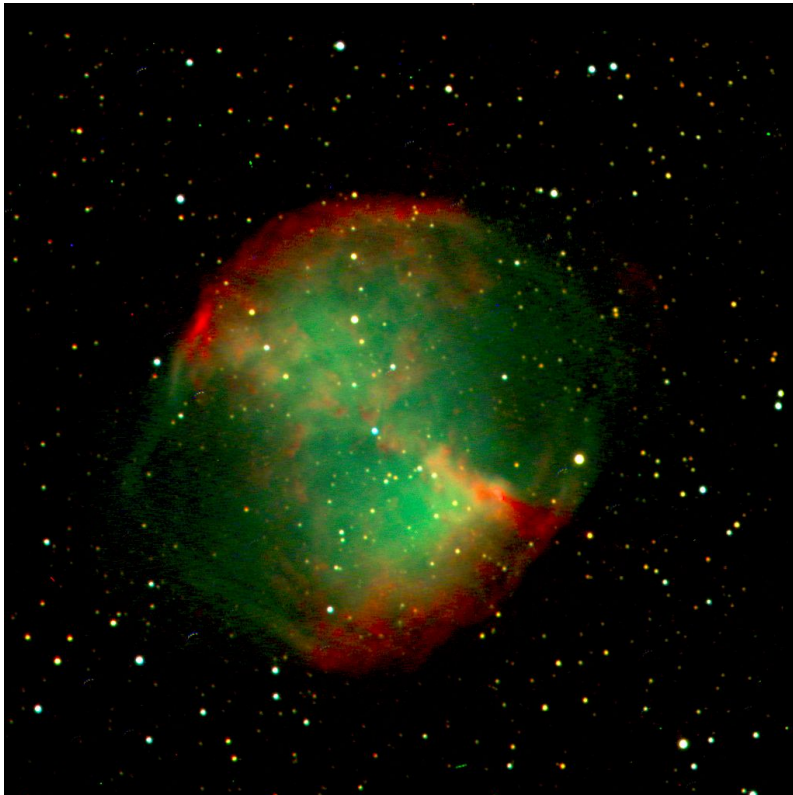


**RR Lyrae stars:
Substructures
and the Oosterhoff dichotomy
in the Halo of the Milky Way**



Mohamad Abbas

Dissertation
submitted to the
Combined Faculties for the Natural Sciences and for Mathematics
of the Ruperto–Carola University of Heidelberg, Germany
for the degree of
Doctor of Natural Sciences

Presented by
Mohamad Abbas
Born in: Kuwait, Kuwait
Oral examination: 12th of December, 2014

**RR Lyrae stars:
Substructures
and the Oosterhoff dichotomy
in the Halo of the Milky Way**

Mohamad Abbas

Referees: Prof. Dr. Eva K. Grebel
Prof. Dr. Joachim Wambsganss

This work is dedicated to my beloved father and mother...
and to my loving and supporting siblings, Tania, Lara, Katia,
Hussein, and Aya.

Without them, I would have been lost

*Have they not observed the heaven above them,
how We have constructed it and beautified it,
and how there are no rifts therein?*

AYAT Qaf 50:6

Abstract

We present the detection of 6371 RR Lyrae (RRL) stars distributed across $\sim 14000 \text{ deg}^2$ of the sky from the combined data of the Sloan Digital Sky Survey (SDSS), the Panoramic Survey Telescope and Rapid Response System 1 3π survey (PS1), and the repeated observations from the second photometric catalogue from the Catalina Survey (CSDR2). Around 2000 of these stars are new discoveries. The completeness level of our RRL stars (4800 RRab and 1571 RRC stars) is $\sim 50\%$ while the efficiency levels for RRab and RRC stars are $\sim 99\%$ and $\sim 87\%$, respectively. We show that our method for selecting RRL stars allows us to recover halo substructures. Moreover, we present a method for selecting RRL stars and other types of variable stars in the absence of a large number of multi-epoch data and light curve analyses. Our method uses a Gaussian Mixture Bayesian Generative technique (GMM) to apply SDSS color and PS1 variability cuts instead of the commonly used rectangular cuts. A comparison between our efficiency and completeness levels using the GMM method to the efficiency and completeness levels using rectangular cuts that are commonly used yielded a significant increase in the efficiency level from $\sim 13\%$ to $\sim 77\%$ and an insignificant change in the completeness levels. Although we develop it over the SDSS \times PS1 footprint, our technique would work well on any multi-band, multi-epoch survey for which the number of epochs is limited.

Additionally, we study the different Oosterhoff populations (OoI and OoII) in the Milky Way's halo using the largest catalog of RRab stars from the Catalina Sky Survey (CSS). We show that $\sim 73\%$ of the halo RRab stars are of OoI type (RRab_{OoI}) and that the latter stars are more metal-rich compared to RRab_{OoII} stars. By examining the change of RRab_{OoI} and RRab_{OoII} stars with Galactocentric distances (R_{gc}), we detect two turning points at $R_{gc} \sim 25 \text{ kpc}$ and $R_{gc} \sim 45 \text{ kpc}$. We believe that these turning points are associated with breaks in the power-laws of the halo and that they divide the stellar halo into three main components: the inner halo, the outer halo, and the "extreme outer halo" components. We also study the Oosterhoff populations of the RRL stars in the direction of the trailing arm of the Sagittarius dwarf spheroidal (dSph) galaxy, the Virgo substructure, and the Hercules-Aquila Cloud and we conclude that these substructures are dominated by RRab_{OoI} stars ($\sim 80\%$) and that the mean periods of their RRab stars fall near the boundary of the Oosterhoff gap; results that suggest that they had dSph galaxy progenitors.

Zusammenfassung

Wir präsentieren die Detektion von 6371 RR-Lyrae-Sternen (RRL-Sternen), verteilt über $\sim 14000 \text{ deg}^2$ des Himmels. Sie wurden sowohl in den kombinierten Datensätzen des Sloan Digital Sky Survey (SDSS), dem Panoramic Survey Telescope und dem Rapid Response System 1 3π Survey (PS1), als auch den wiederholten Beobachtungen des zweiten photometrischen Katalogs des Catalina Survey (CSDR2) entdeckt. Etwa 2000 dieser Sterne sind neue Entdeckungen. Der Vollständigkeitsgrad der beobachteten RRL-Sterne (4800 RRab- und 1571 RRC-Sterne) beträgt $\sim 50\%$, wohingegen die Effizienz bei den RRab-Sternen bei $\sim 99\%$ und bei RRC-Sternen 87% liegt. Wir zeigen, dass unsere Selektionsmethode von RRL-Sternen es uns erlaubt, Sub-Strukturen im stellaren Halo der Milchstraße nachzuweisen. Darüberhinaus präsentieren wir eine Methode zur Selektion von RRL-Sternen und anderer variabler Sterne, für die nur wenige Messungen zu verschiedenen Zeitpunkten zur Verfügung stehen und für die keine Analyse von Lichtkurven möglich ist. Unsere Methode benutzt die Gaussian-Mixture-Bayesian-Generative-Technik (GMM), um anstelle der herkömmlichen Farbselektionen neue Selektionskriterien zu definieren, die auf SDSS-Farben und PS1-Variabilitäten beruhen. Obgleich wir diese Methode für Sterne, die sowohl mit SDSS wie auch PS1 beobachtet wurden, entwickelt haben, kann die Methode auch auf andere Mehrfarbendurchmusterungen und Daten mit nur wenigen Epochen angewandt werden.

Außerdem untersuchen wir die verschiedenen Oosterhoff-Populationen (OoI und OoII) im Halo der Milchstraße mithilfe des größten Kataloges an RRab-Sternen des Catalina Sky Survey (CSS). Wir zeigen, dass $\sim 73\%$ der RRab-Sterne des Halo vom Typ OoI sind (RRab_{OoI}) und dass diese Sterne metallreicher sind im Vergleich zu RRab_{OoII} Sternen. Bei der Untersuchung der Verteilung von RRab_{OoI} und RRab_{OoII} Sternen mit galaktozentrischem Abstand (R_{gc}) finden wir zwei Wendepunkte bei $R_{gc} \sim 25 \text{ kpc}$ und $R_{gc} \sim 45 \text{ kpc}$. Wir glauben, dass diese Wendepunkte mit Brüchen in den Profilen des Halos verknüpft sind und dass sie den stellaren Halo in drei Hauptkomponenten unterteilen: Den inneren Halo, den äußeren Halo und den "extremen äußeren Halo". Wir untersuchen auch die Oosterhoff-Populationen der RRL-Sterne in Richtung des nachfolgenden Arms der kugelförmigen Zwerggalaxie Sagittarius, der Virgo-Substruktur und der Hercules-Aquila-Wolke und wir schließen daraus, dass die Substrukturen von RRab_{OoI} Sternen dominiert sind ($\sim 80\%$) und dass die mittleren Perioden der RRab-Sterne nahe der Grenze der Oosterhoff-Lücke liegen. Diese Ergebnisse zeigen, dass die RRL-Sterne aus sphäroidalen Zwerggalaxien stammen könnten.

Contents

1	Introduction	1
1.1	The Milky Way	1
1.1.1	The Disk	3
1.1.2	The Bulge	3
1.1.3	The Halo	4
1.2	Understanding the Halo	4
1.3	RRL Stars as Tracers of the Halo	5
1.4	Thesis topics, results and structure	10
2	RR Lyrae Stars	13
2.1	Introduction	14
2.2	On the Origin of the Naming	14
2.3	Types of RRL Stars	14
2.4	Pulsations of RRL Stars	15
2.5	The Blazhko Effect	17
2.6	The Oosterhoff Effect	18
2.7	Summary	18
3	Used Data And Surveys	23
3.1	Introduction	24
3.2	The Panoramic Survey Telescope and Rapid Response System 1 (Pan-STARRS1)	24
3.2.1	The PS1 Survey	24
3.2.2	The PS1-MD Survey	24
3.3	The SDSS	24
3.4	The Catalina Real-Time Transient Survey (CRTS)	25
3.4.1	The CSS	25
3.4.2	The SSS	27
3.4.3	The MLS	27
3.5	The Quasar Equatorial Survey Team RRL Stars Survey (QUEST)	27
3.6	The La Silla QUEST (LSQ) Southern Hemisphere Variability Survey	27
3.7	RRL Star Surveys	27

4	Our Newly Discovered RR Lyrae Stars	33
4.1	Introduction	34
4.2	Identifying RRL stars	35
4.2.1	The SDSS Color Cuts	35
4.2.2	The PS1 Variability Cuts	37
4.3	The CSDR2 Light Curves	37
4.3.1	The Analysis of Variance	39
4.3.2	Template Fitting Method	40
4.4	Results	43
4.5	Comparison with Stripe 82	43
4.5.1	Completeness	43
4.5.2	Missed RRL Stars	43
4.5.3	Efficiency	45
4.5.4	Period Testing	45
4.6	Comparison With the Catalina and the LSQ QUEST catalog of RRL stars	45
4.6.1	The Catalina catalog of RRL stars	45
4.6.2	The LSQ QUEST catalog of RRL stars	48
4.7	Newly Discovered RRL Stars	48
4.7.1	RRab Stars	48
4.7.2	RRc Stars	48
4.7.3	Contaminant Stars	50
4.8	Distances Of RRL Stars and Halo SubStructure	50
4.9	Summary	55
5	An optimized Method to Identify RRL stars	57
5.1	Introduction	58
5.2	RRL Stars	58
5.2.1	The Colors of RRL Stars in the SDSS and PS1 Photometric Systems	58
5.2.2	Pre-identified Sample of RRL stars	60
5.3	Applying and Testing our Method	60
5.3.1	Stripe 82	62
5.3.2	Applying Regular Rectangular Cuts	66
5.3.3	Contaminant Stars	68
5.4	RRL Candidates	69
5.5	Halo Substructure	71
5.6	Summary	71
6	The Oosterhoff Populations in the Milky Way's Halo	73
6.1	Introduction	74
6.2	The Oosterhoff Groups in the Stellar Halo	74
6.2.1	Changes in the Oosterhoff Populations With Galactocentric Distance	78
6.3	The Oosterhoff Groups in the substructures of the halo	80
6.3.1	Part of the Sagittarius Stream	80
6.3.2	The Virgo Substructure	81
6.3.3	The Hercules-Aquila Cloud (HAC)	84
6.4	Summary	84
7	Summary	87
7.1	Summary	87
	List of Abbreviations	91

References	93
Acknowledgements	99
Curriculum Vitae	103

List of Figures

1.1	Artist's conception of the Milky Way galaxy	2
1.2	A schematic diagram showing the different components of the Milky Way	3
1.3	Artist's illustration showing the Milky Way, the Small, and Large Magellanic Clouds	4
1.4	Colors of RRL stars in the SDSS filters	7
1.5	The $(NUV - V)_0$ colors of halo RRab, disk RRab, and RRc stars	8
1.6	Variability of RRL stars in the SDSS filters	9
1.7	CMD of the new thin stellar stream	10
2.1	Sample light curve of one RRab star	15
2.2	Sample light curve of one RRc star	16
2.3	The P–A distribution for RRL stars	17
2.4	Color change of RRL and eclipsing binary stars	20
2.5	Light curve of an RRab star that is exhibiting the Blazhko effect	21
2.6	The metallicity vs. $\langle P_{ab} \rangle$ distribution of globular clusters and dwarf satellite galaxies	22
3.1	Transmissions of the PS1 and SDSS filters as a function of wavelength	26
3.2	Comparison between amplitudes of RRL stars in the V and NUV bands	30
4.1	Our color-color cut in the u , g , and r filters	36
4.2	The number of CSDR2 observations per star	38
4.3	Illustration of the Analysis of Variance technique	40
4.4	The ten TFM templates used to classify our variable objects	41
4.5	Best-fitted templates by the TFM for CSDR2 star-id 1157029004107	42
4.6	Phased light curves of RRab and RRc stars located in Stripe 82	46
4.7	Phasing light curves of two stars using different periods	47
4.8	Phased light curves of CSDR2 star-id 2122228003249	49
4.9	Phased light curves from our study and from the GCVS	51
4.10	The number density distribution of the RRL stars found in the Stripe 82 area	53
4.11	The number density distribution of the RRL stars found in the Northern Galactic hemisphere section of the celestial equator	54

5.1	The difference of the colors of RRL stars in the SDSS and PS1 photometric systems	59
5.2	Different SDSS color-color density plots of the 636 RRL stars used in our study	61
5.3	The $(u - g)$ vs. $(g - r)$ colors of the 636 pre-identified RRL stars and the GMM color selection boundary	64
5.4	The $(g - r)$ vs. $(r - i)$ colors of the 636 pre-identified RRL stars and the GMM color selection boundary	65
5.5	The g_{P1} vs. $(\sigma_{g_{P1}} + \sigma_{r_{P1}})$ distribution of stars that passed the SDSS GMM color selection cuts	66
5.6	A comparison between the efficiency and completeness levels resulting from the GMM and rectangular cuts techniques	67
5.7	Phased light curves of a stars in Algol binary system and of a δ Scuti candidate	68
5.8	The efficiency and completeness levels as a function of magnitude	69
5.9	The GMM variability selection boundary	70
5.10	The number density distribution of the RRL stars in Stripe 82	72
6.1	Spatial distribution of the CSS RRab stars, LSQ RRL stars, and the Stripe 82 RRL stars	75
6.2	The P–A density plot of the CCS RRab stars	76
6.3	The ΔP density plot of the CCS RRab stars	77
6.4	The metallicity vs. $(u - g)_0$ plot of RRab _{OoI} and RRab _{OoII} stars in addition to their metallicity distributions	79
6.5	Histograms of the R_{gc} distribution for RRab _{OoI} and RRab _{OoII} stars, and the change of N_{RRab}^{OoI}	80
6.6	Distribution of RRab _{OoI} sand RRab _{OoII} stars located in the direction of the trailing tail of the Sgr dSp	82
6.7	Distribution of RRab _{OoI} sand RRab _{OoII} stars located in the footprint of the Virgo substructure and comparison field regions	83
6.8	Distribution of RRab _{OoI} sand RRab _{OoII} stars located in the direction of the HAC	85

List of Tables

2.1	The Oosterhoff Groups	18
3.1	MDF Fields Central Locations	25
3.2	Exposure times of all filters in different surveys	28
3.3	A brief summary for some of the RRL Star surveys	31
4.1	Our applied color cuts	36
4.2	Our catalog of RRL stars	44
7.1	Oosterhoff populations in halo substructures	88

Introduction

Set no limits to yourselves. Spread out until there are no regions where you are not. Spread out until the whole world be wherever you are. Spread out until you meet God wherever you meet yourselves. Spread out. Michael Naimy

In this thesis, we cover several topics and searches which are related to RR Lyrae (RRL) stars in the Milky Way. Our aim is to find RRL stars to better understand their properties and to use them as fossils to trace back the formation history of the Milky Way's halo. We also aim to develop new methods to detect RRL stars more efficiently. This was done by: (1) Finding new RRL stars using light curve analyses. (2) Using RRL stars to detect overdensities in the halo. (3) Studying the Oosterhoff effect that they exhibit in the halo. (4) Studying the latter effect they exhibit in satellite galaxies. (5) Detecting different populations of RRL stars in the halo (i.e., different properties). (6) Detecting turning points in the Oosterhoff populations that are associated with the breaks in the power-laws of the halo. (7) Improving our understanding of their color and variability properties. (8) Developing efficient and reliable methods to find RRL stars and other variable stars when light curve analysis is not possible. In the following chapters, those topics will be covered in great detail.

This chapter is organized as follows. In Section 1.1, we start by discussing the general properties of the Milky Way and of its three main components (the disk, the bulge, and the halo). In Section 1.2, we explain the different formation scenarios of the Milky Way's halo. The advantages of using RRL stars as traces of the halo and of the Milky Way's formation history are introduced and explained in Section 1.3. The broad topics and results of this thesis are briefly mentioned in Section 1.4. Finally, the structure of this thesis is given in the latter section.

1.1 The Milky Way

When Galileo Galilei, the “father of modern observational astronomy”, constructed the first telescope in Holland in 1610, he came up with many important astronomical discoveries. Some of these discoveries were sunspots and the four largest moons of Jupiter. His observations led him to announce that the Earth was not at the center of the solar system, instead, he believed that the Sun was at the center. As this was a revolutionary discovery at that time, he was accused of heresy and was forbidden by the church from teaching or advocating his ideas. For more than 300 years after Galileo, most observational astronomers assumed that all the stars and “nebulae” in the universe were contained inside of the Milky Way.

It is well known now that the Milky Way is only one out of hundreds of billions of galaxies in the universe. The Milky Way consists of at least 200 billion stars and their planets, thousands of clusters and nebulae, dark matter, gases, and dust. Infrared surveys performed by the Spitzer Space Telescope (Werner et al., 2004) confirmed that the Milky Way is a barred spiral galaxy of SBc type (i.e., loosely bound arms). Since we are embedded in it, it is very difficult to figure out what the Milky Way looks like exactly. We show an artist's conception of its shape in Figure 1.1.



Figure 1.1: Artist's conception of the Milky Way galaxy. Credit: Nick Risinger.

Understanding the process of galaxy formation has always been an important goal in astrophysics. In particular, the formation and evolution of disk galaxies still pose many unsolved questions. Many observational studies have focused on the Milky Way as the one disk galaxy that can be studied in the greatest detail (i.e., see the reviews of Freeman & Bland-Hawthorn 2002; Ivezić et al. 2012). Fortunately, in the last few decades, our understanding of the Milky Way properties has been greatly improved.

The main reason behind the new discoveries is the development of new sensitive surveys that are designed to observe large areas of the sky in different wavelengths. For instance, the Two Micron All Sky Survey (2MASS, Skrutskie et al. 2006) provided us with an enhanced picture of the near-infrared sky and the Sloan Digital Sky Survey (SDSS, Fukugita et al. 1996; York et al. 2000) has created 3-D dimensional maps of the Galaxy. These surveys, in addition to other surveys that we discuss in Chapter 3 have proved that the formation history of the Galaxy is more complicated than we have thought (Jurić et al., 2008). Special emphasis in these studies has been placed on the Galactic stellar halo (i.e., Johnston et al. 2008; Schlafman et al. 2009). The three main components, (1) the disk, (2) the bulge, and (3) the halo, that make up the Milky Way are discussed below.

1.1.1 The Disk

The disk is a flattened, rotating system which contains the majority of the gas and dust in the Milky Way. It is a very prominent and distinct part of the Galaxy because of its spiral arms. Stars in the disk orbit the Galactic center at about 200 km s^{-1} . Our Sun lies within the Galactic disk at $\sim 8 \text{ kpc}$ from the center of the Galaxy and takes $\sim 250 \text{ Myr}$ to orbit the Galactic center. The luminosity of the disk is $\sim (15\text{--}20) \times 10^9 L_\odot$ while its mass in stars is $\sim 60 \times 10^9 M_\odot$ (Sparke & Gallagher, 2007). The disk, which extends to more than $\sim 15 \text{ kpc}$ from the Galactic center, experiences an exponential drop in the density of its stars, both radially and vertically. Thus, the disk is divided into two main subcomponents: the thin and thick disks. The thin disk contains most ($\sim 95\%$) of the stars that are young and metal-rich and is where most of the star formation takes place. It is defined by its small scale height (h_z) of $\sim 0.3 \text{ kpc}$. On the other hand, the thick disk surrounds the thin disk and contains older and more metal-poor stars than the ones found in the thin disk. The thick disk has $h_z \sim 1 \text{ kpc}$. The different stellar populations in the thin and thick disks suggests a difference in their formation histories. The thin and thick disks are shown in the schematic diagram of the Milky Way in Figure 1.2.

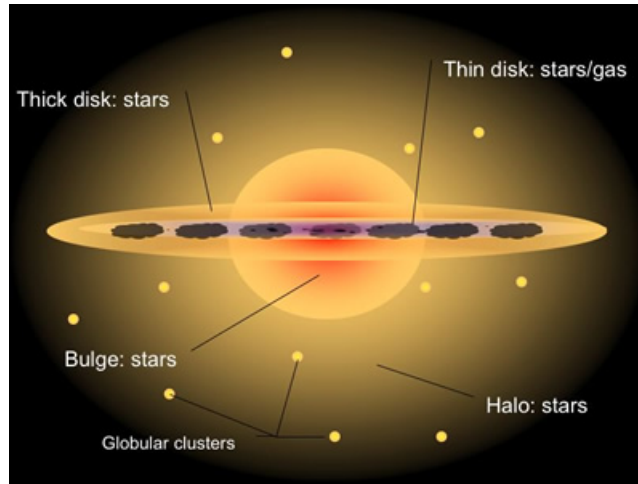


Figure 1.2: A schematic diagram showing the different components of the Milky Way. Credit: Swinburne University of Technology.

1.1.2 The Bulge

The Bulge, which extends few kpcs above and below the disk, is one of the most important parts of the Galaxy. The luminosity of the bulge is $\sim 5 \times 10^9 L_\odot$ while its mass in stars is $\sim 20 \times 10^9 M_\odot$ (Sparke & Gallagher, 2007). The rotating Bulge consists mainly of Population II (age $> \sim 9 \text{ Gyr}$) and metal-poor ($-1 < [\text{Fe}/\text{H}] \text{ (dex)} < 0.5$) stars. Because of the high extinction due to dust and because of the crowding of stars in its direction, the bulge used to be avoided when studying the Milky Way formation history (i.e., Eggen et al. 1962; Searle & Zinn 1978). However, near-infrared all sky maps from 2MASS and DIRBE (Dwek et al., 1995) have revealed the importance of the peanut-shape bulge (Minniti & Zoccali, 2008). It has different kinematics and compositions from the other Galactic components. Additionally, metal-rich globular clusters are found in the bulge. These clusters have the same kinematics and spatial distributions as the bulge field stars. The Bulge, which is located at the center of the Galaxy (see Figure 1.2), is the home of the galactic nucleus, the dead center of a galaxy and home to an extremely dense clustering of ancient stars, and it is believed to be the home of a black hole ($M_{BH} \sim 4 \times 10^6 M_\odot$, Sparke & Gallagher 2007).

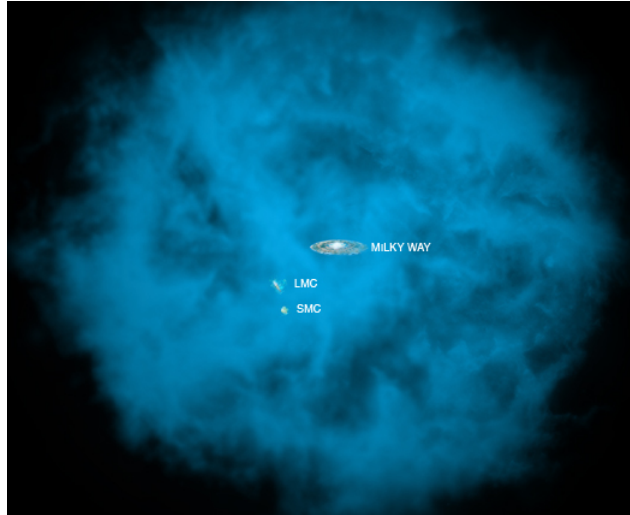


Figure 1.3: Artist’s illustration showing the hot gas of the halo (in blue) that surrounds the Milky Way. The two small neighboring galaxies, Small and Large Magellanic Clouds, are also shown. Credit: NASA.

1.1.3 The Halo

The Galactic halo is the old, roughly spherical and extended component of our Galaxy. It contains dark matter, hot gases, and Population II stars, and it extends beyond the Galactic disk. It also hosts numerous globular clusters. The rotation of the stars and globular clusters in the halo is usually random and do not follow any trend (Sparke & Gallagher, 2007). The exact shape, mass, and size of the halo are still obscure. Unlike the bulge and disk, the halo is mostly dark and is dominated by dark matter. Understanding the exact nature of the Milky Way halo plays a key role in current models of galaxy formation and evolution and may help to explain the mysterious dark matter, which seems to pervade the universe. The halo itself is made of two parts: the inner halo and the outer halo.

1.2 Understanding the Halo

The inner and outer halo are not cleanly divided. However, different types of halo tracers like RRL, horizontal-branch, blue straggler, and main-sequence stars, in addition to models have been used to study the number density profile of the halo (i.e., Deason et al. 2011; Sesar et al. 2011b; Zinn et al. 2014; Simion et al. 2014; Abbas et al. 2014d). These studies have detected comparable breaks at Galactocentric distances (R_{gc}) ~ 25 kpc, suggesting a transition from the inner to outer halo. The outer halo region of the Milky Way, as with other galaxies, contains the vast majority of the mass of the Galaxy. Figure 1.3 illustrates how the hot gas of the halo (in blue) envelops the Milky Way, and how it extends to further than ~ 100 kpc from the Galactic center.

It is believed from observations and simulations that mergers and accretions of smaller systems contributed to the formation of the outer halo (i.e., Bullock et al. 2001; Bullock & Johnston 2005; Carollo et al. 2007; Beers et al. 2012) while the inner halo is a result of accretion of a few massive systems in addition to in situ star formation processes (i.e., Yanny et al. 2003; Jurić et al. 2008; De Lucia & Helmi 2008; Zolotov et al. 2010; Font et al. 2011; Schlafman et al. 2012). This scenario implies that many of the halo stars were formed in dwarf galaxies outside the Milky Way (i.e., Bullock & Johnston 2005).

These accretion events and mergers leave signatures in the structure and kinematics of the stellar halo, usually in the form of stellar streams, substructures, and overdensities (Ibata et al., 1995; Newberg et al., 2003; Duffau et al.,

2006; Schlafman et al., 2009; Sesar et al., 2010). Because of the infall pattern of the progenitor satellites from where streams originate, some of these streams overlap on the sky (Helmi et al., 2011). As witnesses of the early phase of the formation of our Galaxy, these halo stars can be used as fossils to trace back the history of our Galaxy (i.e., Johnston et al. 2008; Schlafman et al. 2009; Zolotov et al. 2010). A complete and a deep map of the halo is vital to find the remnants of the accretion processes (i.e., Keller et al. 2008; Bell et al. 2008; Zolotov et al. 2010). Over the past decade, various halo overdensities and stellar streams have been discovered using different methods and different types of stars. For instance, the detections of new halo clumps and substructures like the Sagittarius (Sgr) dwarf galaxy (Ibata et al., 1995) and its extended tidal tails (Ivezić et al., 2000; Yanny et al., 2000), Palomar 5 (Pal 5, Odenkirchen et al. 2001), and the Hercules-Aquila Cloud (HAC, Belokurov et al. 2007) reflected the inhomogeneity nature of the Milky Way's halo. Since then, the Milky Way's halo has been the subject of intense scrutiny to find more of these substructures and to better understand their properties (i.e., Johnston et al. 2008; Schlafman et al. 2009). For a summary, see Ivezić et al. (2012).

It is easier to detect substructures and overdensities of stars at larger R_{gc} where the dynamical time scales are longer (Bullock et al., 2001; Bell et al., 2008). The absence of massive and luminous stars, the old main-sequence turn-offs, the prevalence of horizontal-branch stars, and the low metallicities of the halo stars indicate that halo stars are predominantly old. However, it is still unclear whether these stars were mainly formed in situ during the early phase of the collapse of the Milky Way, or whether they were formed outside the Milky Way in satellite galaxies only to be accreted by the Milky Way at a later date (i.e., Vivas et al. 2004; Carollo et al. 2007; Bell et al. 2008). Answers to such questions may be found by identifying and characterizing the streams that the satellite galaxies have left in the halo (i.e., Zolotov et al. 2010) of the Milky Way where the contamination of foreground stars makes the mapping of stellar structures difficult. Additionally, these streams can serve as very sensitive probes to deduce the shape of the Milky Way's potential (Newberg et al., 2002; Law et al., 2009). The accreted substructures identified so far mainly seem to consist of old stars. Thus, it is expected that such populations are revealed by maps of RRL stars, these being found only in old stellar populations.

1.3 RRL Stars as Tracers of the Halo

Variable stars like the RRL stars have a history of being exploited to help us study the distances and properties of our Galaxy. For instance, when Henrietta Swan Leavitt from the Harvard College Observatory (HCO) was studying the variability of stars in the Small Magellanic Cloud, she realized that brighter Cepheid stars tend to have longer periods. In 1912, she confirmed an accurate relationship between the apparent brightness of Cepheid variables and their pulsation periods (i.e., the period-luminosity relation). Another period-luminosity relation was then established for RRL stars. These period-luminosity relations played a critical role in understanding the size of the Milky Way and the universe as a whole. At first, distances to the Cepheids and RRL stars in the Milky Way and globular clusters were computed and the size of the Milky Way was becoming clearer. Most importantly, when Cepheids were detected in other galaxies that were formerly believed to be “nebulae”, it became clear that these “nebulae” were distinct galaxies and that not all the stars are contained in the Milky Way.

Until this day, astronomers still use Cepheid and RRL stars among other stars (i.e., main-sequence stars and red giants) to map the Galaxy and to better understand its formation history. In the last decades, and because of the numerous large sky surveys that have been established, there has been a growing emphasis on studying the Galactic halo using RRL stars. Finding RRL stars and their distances is one way to map the Galactic halo and find its stellar streams. These stars can be also used as objects to study the intrinsic halo population, the distribution, and the gradients in halo metallicity. For instance, the domination of the inner and outer halo by slightly more metal-rich and metal-poor stars, respectively, and their different global kinematics supports the different scenarios of the formation processes of the inner (in situ formation) and outer (accretion processes) halo (Carollo et al., 2007, 2010). This evolutionary picture is also supported by studying RRL stars in both parts of the halo (i.e., Kinman et al. 2012). However, the number of predicted substructures vary substantially (i.e., Bell et al. 2008; Deason et al. 2011; Zinn et al. 2014) and thus more observations are needed.

RRL stars are periodic variables located on the horizontal branch of an old stellar population's color-magnitude diagram (CMD). They have periods less than ~ 1 day (d) (Smith, 1995), so the detection of RRL stars requires repeated observations. Over the past two decades, colors, variability, and light curve properties of RRL stars have been well

studied and characterized (i.e., Ivezić et al. 2005; Vivas & Zinn 2006; Abbas et al. 2014a,b,d). See Chapter 2 for more details about RRL stars. In the following, we will introduce some of the advantages of RRL stars that motivate us to use them for the purposes described above.

1. RRL stars have witnessed the formation history of the halo as they belong to the old populations (age $> \sim 9$ Gyr). Thus, they hold a critical role to identify the Milky Way satellites that have contributed to build up the Galactic halo (Greco et al., 2010).
2. Their well-defined period-luminosity relation and their nearly constant absolute magnitude ($\langle M_V \rangle = 0.6 \pm 0.1$, Layden et al. 1996) make them very good standard candles. Thus, once an RRL star is identified, it is relatively easy to estimate its heliocentric distance ($d_h = 10^{((V_0) - M_v + 5)/5}$). Taking the photometric and color uncertainty into account in addition to the RRab metallicity dispersion of [Fe/H] in the halo, d_h is determined with $\sim 5\%$ uncertainty (Sesar et al., 2010; Drake et al., 2013a; Abbas et al., 2014a).
3. Unlike main-sequence stars, RRL stars are intrinsically bright and can thus be used to study the farthest parts of the halo.
4. While the nearly symmetric light curves of RRL stars of c type (RRc stars) can be confused with other types of variable stars like Ursae Majoris (W UMa), δ Scuti, and SX Phe stars, RRL stars of ab type (RRab stars) have very distinctive light curves that can be easily identified and distinguished from other type of variable stars. See Chapter 2 for sample light curves for RRab and RRc stars. Additionally, it is easier to detect the variability of RRab stars than that in RRc stars because RRab stars tend to have larger amplitudes.
5. One of the most important properties of RRL stars is their well defined colors. We show a comparison of the color-color distributions of RRL (red circles) and non-RRL (black dots) stars in Figure 1.4. These colors are from the five SDSS filters ($u, g, r, i,$ and z) that we describe in Chapter 3. The three different distributions shown in the latter figure illustrate the usefulness of applying color cuts when searching for RRL stars and show how the farther away we go from the main stellar locus, the fewer non-RRL stars we have. Since the $(u - g)$ color serves as a surface gravity indicator and since the $(g - r)$ color reflects the effective temperature of RRL stars (Ivezić et al., 2005), the RRL stars are best identified in the $(u - g)$ vs. $(g - r)$ color-color diagram (lower panel of Figure 1.4). Additionally, using the ultraviolet band (NUV) from the Galaxy Evolution Explorer (GALEX, Martin et al. 2005), Kinman & Brown (2014) recently showed that the $(NUV - V)$ color is very sensitive to metallicities and effective temperatures and that the latter color can be used to estimate the metallicities and effective temperatures of these stars. This is illustrated in Figure 1.5.
6. Just like the case with other variable objects, RRL stars can be easily identified using different variability statistics when multi-epoch data are available. At the same time, RRL stars have nearly consistent variability properties in different filters that can be used to identify them more efficiently. For instance, the distribution of the rms scatter (σ) in the SDSS g (σ_g) and r (σ_r) bands is shown in the upper panel of Figure 1.6. The blue dots represent stars with light curves that have been well-fitted with RRL templates from Sesar et al. (2010). The template-rejected stars are shown in red open squares, and the green triangles represent stars that did not have RRL-like light curves but that showed variability similar to that of RRL stars. Using this distribution, Sesar et al. (2010) showed that $\sim 97\%$ of the RRL stars have $|\sigma_g - 1.42\sigma_r| < 0.03$ while most of the non-pulsating variables have $\sigma_g = \sigma_r$. The middle and lower panels of Figure 1.6 show the $(\sqrt{\sigma_g^2 + \sigma_r^2}$ vs. $\sigma_{g-r})$ and the $(g_0$ vs. $A_g)$ ¹ distributions of the same stars. These plots show how RRL stars have distinctive variability properties and how can these properties help in separating RRL from non-RRL stars.
7. RRL stars exhibit the so called Oosterhoff effect (Oosterhoff, 1939) which can be briefly summarized as follows (see Section 2.6 for more details). The period-amplitude (P–A) distribution of RRL stars displays two distinct groups, the Oosterhoff type I (OoI) and Oosterhoff type II (OoII) RRL stars. On average, RRL stars from the OoI group tend to have smaller periods (mean period $\langle P_{ab} \rangle = 0.55$ d) and are more metal-rich than the ones belonging to the OoII group ($\langle P_{ab} \rangle = 0.65$ d). At the same time, RRL stars from dwarf spheroidal (dSph) satellite galaxies and their globular clusters are believed to have mean periods that fall in the so called “Oosterhoff gap” ($0.58 < \langle P_{ab} \rangle < 0.62$). Thus, understanding the different Oosterhoff groups in the halo reflects different

¹where g_0 and A_g are the magnitudes and amplitudes in the g -band, respectively.

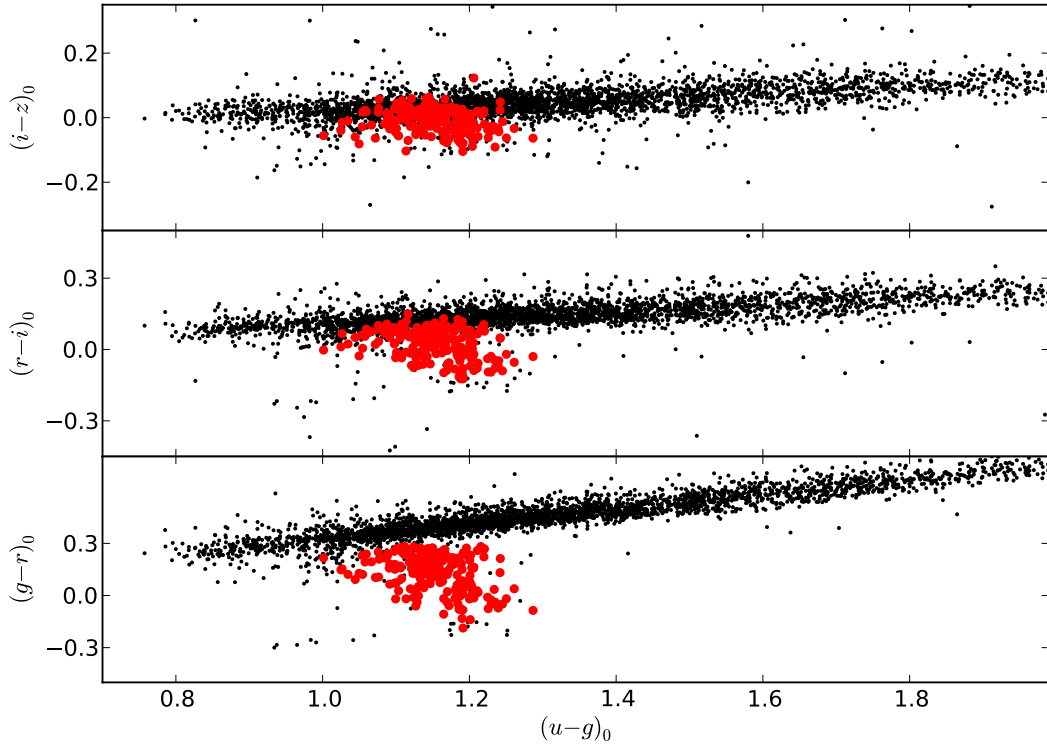


Figure 1.4: The $(u - g)_0$ vs. $(g - r)_0$, $(r - i)_0$, and $(i - z)_0$ color-color distributions (corrected for the line-of-sight interstellar extinction) for RRL (red circles) and non-RRL (black dots) stars are shown in the lower, middle, and upper panels, respectively. RRL stars occupy narrow regions in these color-color plots, an advantage that helps us in distinguishing them from other types of stars. Data taken from Abbas et al. (2014a).

formation histories and may hold valuable information about the formation history of the halo and the Galaxy as a whole. For more details, see Chapter 6 which is based on Abbas et al. (2014d).

Despite all the advantages listed above, RRL stars are scarce objects and are sometimes hard to detect in small halo substructures with sparse horizontal branches. In such cases, more numerous stars like main-sequence stars can be used to detect substructures. For instance, we (Bernard, Ferguson, Schlafly, Abbas, et al., 2014) recently announced the discovery of a new thin stellar stream near the Galactic bulge in the constellation of Ophiuchus using data from the Panoramic Survey Telescope and Rapid Response System 1 3π (hereafter PS1) survey. The short and narrow stream is located at $(l, b) \sim (5^\circ, 32^\circ)$, has $R_{gc} \sim 5 \pm 1$ kpc, and is likely to be a disrupted former globular cluster.

Using the g_{P1} and i_{P1} bands from PS1, Figure 1.7a and Figure 1.7b show the CMD of the new stream and of a nearby comparison region of the same area, respectively. There appears to be an overdensity of main-sequence stars in the region that is highlighted by the red box in panel (a). The red box is plotted with the same coordinates in panel (b) where no overdensity is detected. The few stars located at $(g_{P1} - i_{P1})_0 \sim -0.5$ mag and $i_{P1} \sim 16$ mag are the

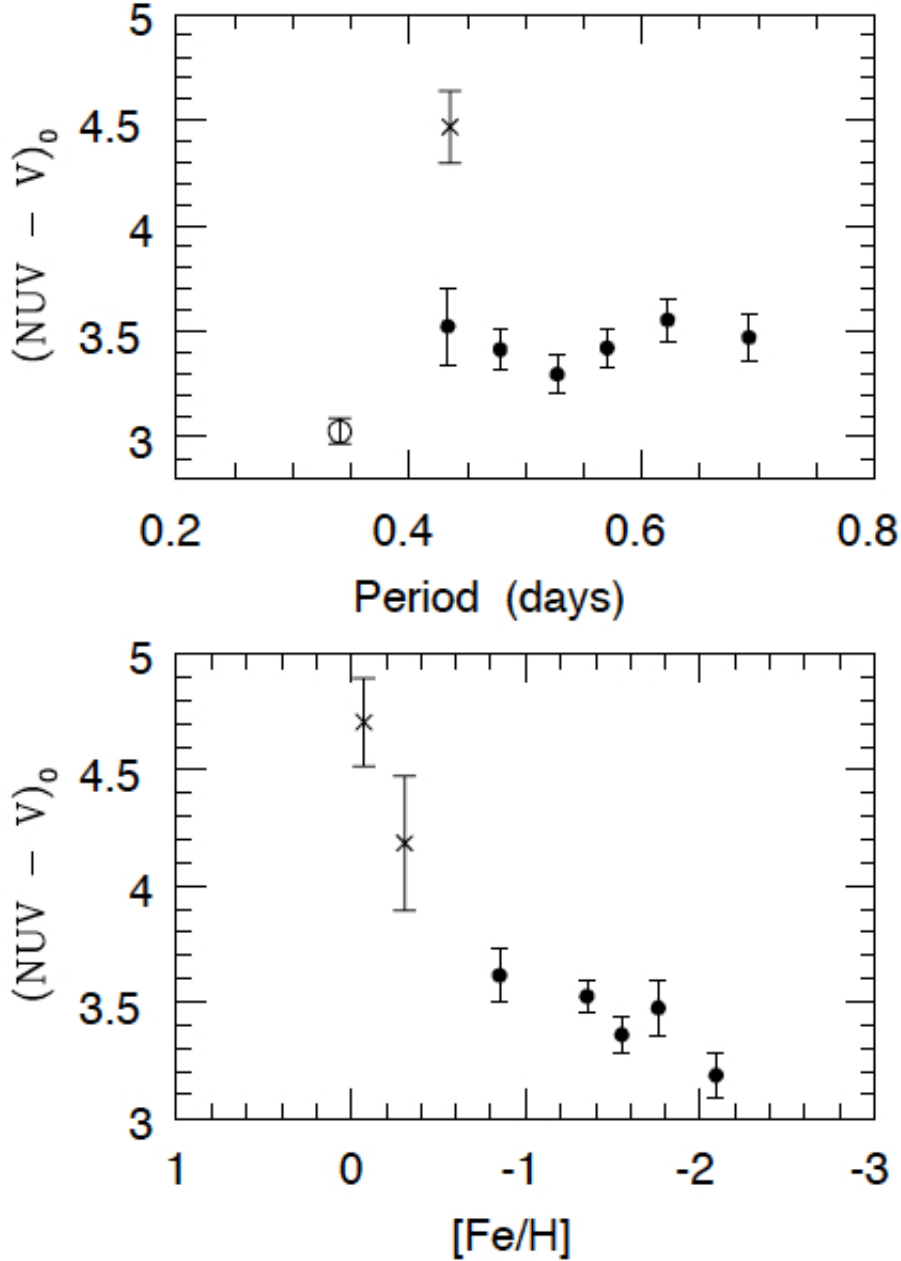


Figure 1.5: Upper panel: Period vs. $(NUV - V)_0$ color (de-reddened) for RRL stars located in the halo (filled circles), RRL stars in the disk (crosses), and RRC stars (open circles). While the difference in the $(NUV - V)_0$ colors of RRab and RRC stars reflects the differences in their temperatures (see Section 2.4), the same difference between halo and disk RRab stars reflects their different metallicities. Lower panel: The $[Fe/H]$ vs. $(NUV - V)_0$ (de-reddened) distribution of RRL stars in the halo (filled circles) and in the disk (crosses). This plot clearly shows that disk RRab stars are more metal-rich than halo RRab stars and shows significant differences in their $(NUV - V)_0$ colors. Figure from Kinman & Brown (2014).

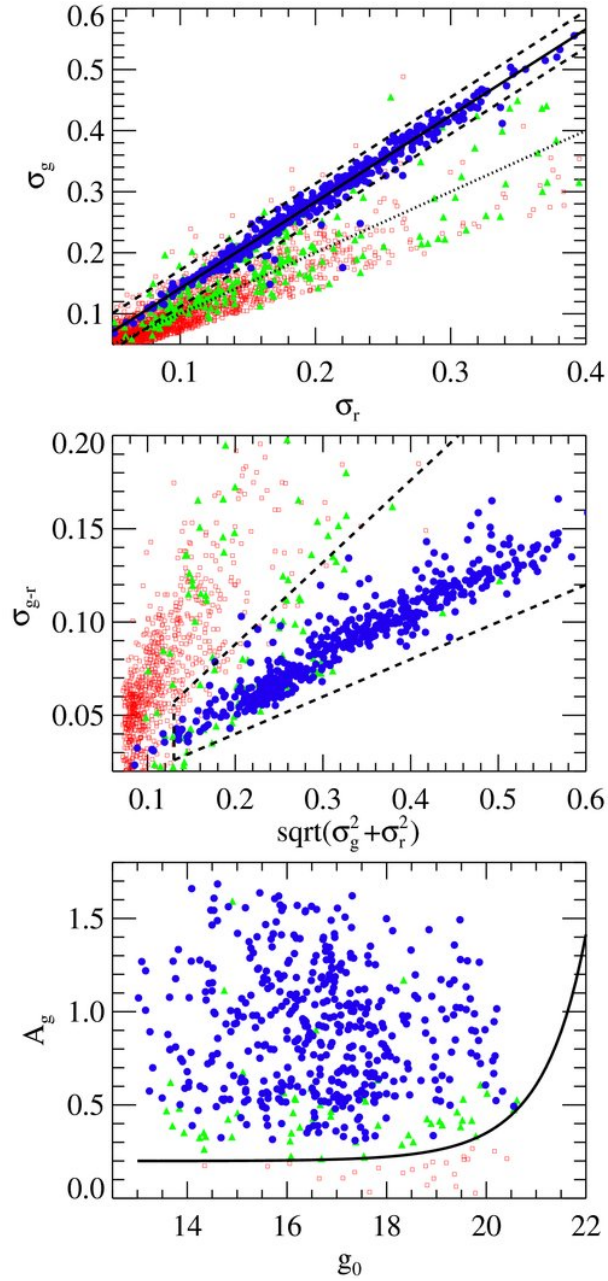


Figure 1.6: Stars with light curves that have been well-fitted with RRL templates are shown as blue dots while stars with light curves that have been rejected by all RRL templates are shown as red open squares. Finally, stars with variability similar to that of RRL stars and that have ambiguous light curves are shown as green triangles. Upper panel: the $(\sigma_r$ vs. $\sigma_g)$ shows how most RRL stars (blue dots) occupy a narrow region. The distributions in the middle ($\sqrt{\sigma_g^2 + \sigma_r^2}$ vs. σ_{g-r}) and lower (g_0 vs. A_g) panels illustrate how most of the RRL stars have distinct variability properties. Figure taken from Sesar et al. 2010.

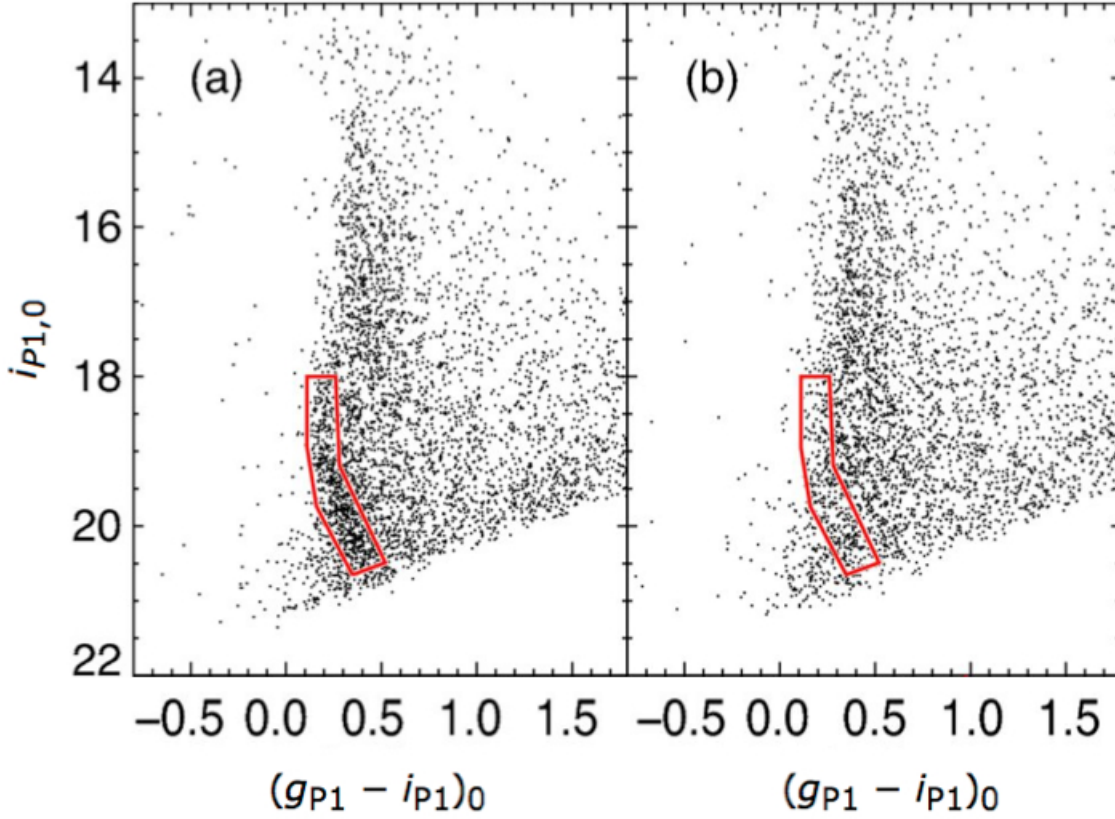


Figure 1.7: The $(g_{P1} - i_{P1})_0$ vs. $(i_{P1})_0$ CMD of our new detected thin stream (left panel) and a nearby comparison region of the same area (right panel). The red box highlights an overdensity in the left panel in contrast to the right panel where no overdensity is detected. Figure from Bernard, Ferguson, Schlafly, Abbas, et al. (2014).

few blue horizontal-branch stars. Because this thin stream has a sparse horizontal branch, no RRL stars were detected in its direction. This example illustrates a case where RRL stars can not be used for the detection of stellar streams. Nevertheless, RRL stars are still considered as one of the most valuable tracers of the halo because of the advantages listed above.

1.4 Thesis topics, results and structure

First of all, because RRL stars are short period variables with well defined colors and variability statistics, we search for them using several sky surveys and we successfully detect 6371 RRL stars, of which ~ 2000 are new discoveries. Our search exploits the strong points of different surveys to mitigate other weak points of the same surveys. As we will show in this thesis, the synergy between data from different surveys results in an efficient and systematic method to find RRL stars. Recently, Kinman & Brown (2014) used our catalog (Abbas et al., 2014a) as a comparison catalog and found similar results. In addition to detecting halo substructures, and because of the large number of repeated observations

used in our study, our catalog can be used to further improve our understanding of the color, light curve, and variability properties of RRL stars.

Additionally, we develop an optimized method for selecting RRL stars and other type of variable stars in the absence of a large number of multi-epoch data and light curve analyses (Abbas et al., 2014b). This is very important as light curve analysis is not always possible due to the lack of sufficient number of repeated observations. We favor using our method in future studies as we proved that its ~ 6 times more efficient than the commonly used methods.

Finally, we investigate the Oosterhoff effect in the halo and in several substructures using ~ 17000 RRab stars (Abbas et al. 2014d, in prep.). We confirm that RRL stars from different halo substructures fall close to the “Oosterhoff gap”. Additionally, we detect the different Oosterhoff populations in the halo and we detect two turning points that are associated with the breaks in the power-laws of the halo. These turning points divide the stellar halo into three main components: the inner halo, the outer halo, and the “extreme outer halo” components. Our results enhance our understanding about the formation history of the halo. In the following chapters, those topics will be covered in great details.

This thesis is organized as follows. Chapter 2 gives detailed information about the history, properties, and types of RRL stars. We also describe the theory behind their pulsations and we discuss their Blazhko and Oosterhoff effects. In Chapter 3, a detailed description of the different surveys we used is given. In the same chapter, we list and discuss some of the studies that searched for RRL stars. Chapter 4, which is based on our published work (Abbas et al., 2014a), discusses the methods and techniques we used to detect 6371 RRL stars in the halo. We also derive their distances and detect halo substructures. Chapter 5, which is based on another published work (Abbas et al., 2014b), describes and introduces an optimized method to search for RRL stars when large number of repeated observations are not available. In the same chapter, a comparison between our method and the commonly used methods is conducted. In Chapter 6, which is based on Abbas et al. 2014d (in prep.), we investigate the Oosterhoff effect in the Milky Way’s halo as a whole and in different halo substructures. We also study the change in the Oosterhoff effect as a function of distance. Chapter 7 provides a summary of the important points and results.

RR Lyrae Stars

Neither the things written up there, nor the desert down below, could have been made or written by the hand of a man. Like the Flowing River

Abstract In this chapter, we introduce and discuss the different properties and importance of RRL stars. RR Lyrae variables are among the most important standard candles that served in measuring distances. We trace back their discovery history, their different subtypes, and we explain the reasons behind their pulsations. Additionally, we discuss the Blazhko effect and the Oosterhoff dichotomy that RRL stars exhibit. These are debatable phenomena that are not fully understood.

2.1 Introduction

RRL stars are periodic variables with periods in the $\sim 0.2\text{--}1$ d range (Smith, 1995; Catelan, 2009), and V -band amplitudes in the $\sim 0.2\text{--}2.0$ mag range (Kholopov et al., 1998). Unlike the case with most stars in eclipsing binary systems, the variability of RRL stars is due to a physical change in their temperatures and radii.

They are low-mass ($\sim 0.7 M_{\odot}$) stars with helium-burning cores. RRL stars are located at the horizontal-branch's gap of a stellar population's CMD. As this gap occurs in a region where many stars pulsate, the instability strip, globular cluster observers avoided observing stars in this region to avoid extended time-domain observing programs. Thus, this omission resulted in the "fake" RRL gap seen in many globular cluster's CMDs (Catelan, 2009).

RRL stars have a mean absolute V -band magnitude of $\langle M_V \rangle = 0.6 \pm 0.1$ (Layden et al., 1996), which makes them very good distance indicators. These variable stars are still bright enough to be detected at large distances such as in the halo. They have been used as tracers of the chemical and dynamical properties of old stellar populations (i.e., Kinman et al. 2007; Keller et al. 2008; Haschke et al. 2012) and have served as test objects for theories of the evolution of low-mass stars and for theories of stellar pulsations (Smith, 1995). Many of the substructures that were discovered in the Milky Way were re-confirmed using RRL stars (i.e., Duffau et al. 2006; Watkins et al. 2009; Sesar et al. 2010).

In Section 2.2, we trace back the discovery history of RRL stars and we introduce the origin of their naming. The different subtypes of RRL stars are introduced in Section 2.3 where we also discuss how their naming evolved with time. In the latter chapter, we discuss their different properties and we show sample light curves of the different subtypes. In Section 2.4, we explain the reasons behind the pulsations of RRL stars and we discuss the different scenarios during their radial expansion and contraction. In Sections 2.5 and 2.6, we review the Blazhko effect and the Oosterhoff dichotomy, respectively. Finally, we summarize this chapter in Section 2.7.

2.2 On the Origin of the Naming

While serving as the director of the HCO between 1877 and 1919, Edward Charles Pickering and his group members were one of the most active astronomy groups at that time. They made visual photometric studies of 45000 stars and published numerous papers and catalogs in the fields of stellar photometry, asteroid searches, and variable stars. Interestingly, his staff who were mostly women conducted most of the calculations and searches of photographic plates. Since then, different types of variable stars in most of the known globular clusters have been studied and identified using different methods and techniques (e.g., Clement et al. 2001; Layden et al. 2003; Baker et al. 2007; Abbas et al. 2014c).

In one of their papers, Pickering et al. (1901) announced the discovery of sixty four variables, of which one ("RR Lyrae star", firstly discovered by Williamina Fleming in 1898) had a short period, high amplitude, and was located in the constellation Lyra. It is located at a distance of ~ 260 pc and has an apparent magnitude of 7.5 mag. At that time, the variability of some stars were explained by the double-star interpretation. However, the brightness of the variable "RR Lyrae star" allowed more precise photometric and spectroscopic studies which in return made Shapley (1914) explain that the variability of Cepheids is due to intrinsic radial pulsations. Likewise, he classified "RR Lyrae star" as a short-period pulsating variable star. The name, RR Lyrae (RRL) star, was then given to variable stars with similar properties.

2.3 Types of RRL Stars

There are four subtypes of RRL stars: RRa, RRb, RRc, and RRd stars (Bailey, 1902; Schwarzschild, 1940; Alcock et al., 2000; Catelan, 2009; Abbas et al., 2014d). The first subclass is the RRd. These stars pulsate in the fundamental and first overtone mode at the same time and are less common than the other types of RRL stars. Studies of RRL stars in globular clusters showed that the mean ratio between the first and fundamental periods of RRd stars is ~ 0.7454 with minimum and maximum values of ~ 0.7433 and 0.748, respectively (Alcock et al., 2000; Catelan, 2009).

On the other hand, both RRa and RRb stars pulsate in the fundamental mode, have a mean period (P_{ab}) of ~ 0.57 d (Smith, 1995), and are more common than the other types of RRL stars. The slight difference between RRa and RRb stars is in the shape of their light curves where RRb light curves tend to show small modifications as compared to RRa

light curves. RRA and RRb stars are commonly grouped into one subclass (RRab). RRab stars have very distinctive asymmetric light curves (fast rise and slow decrease in their brightness) and relatively large amplitudes compared to RRc stars. The second most common RRLs are the RRc stars. These stars pulsate in the first overtone, have smaller amplitudes than RRab stars, and a mean period of ~ 0.34 d. Because they have symmetric light curves, RRc stars can be confused with other types of variable stars like W UMa, δ Scuti, and SX Phe stars (Abbas et al., 2014a).

We show sample light curves from Abbas et al. (2014a) of one of our RRab and RRc stars in Figures 2.1 and 2.2, respectively. These plots illustrate the difference between the light curves of RRab (asymmetric) and RRc (symmetric) stars. In Figure 2.3, we plot the P–A distribution of ~ 6000 RRL stars from Abbas et al. (2014a). It is clear that RRab stars (red dots) tend to have larger periods and amplitudes compared to RRc stars (blue stars). Because of their unique phased light curve shape, and because of their larger pulsation amplitudes, it is relatively easier to identify and characterize RRab stars than to find RRc stars.

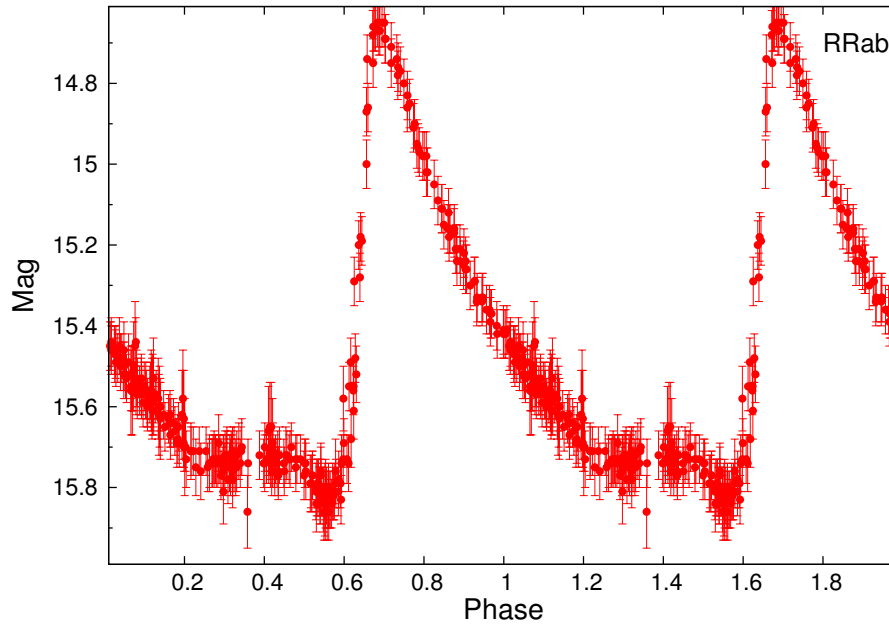


Figure 2.1: Illustration of one of our RRab stars showing the asymmetric behavior of their phased light curves and their large amplitudes compared to RRc stars.

2.4 Pulsations of RRL Stars

At first, Eddington (1926) explained the pulsation of stars by a natural and repeated “valve” driving mechanism that is based on the fusion rates in their cores. It was then shown (Cox & Whitney, 1958; Zhevakin, 1959) that the valve mechanism is driven in the second ionization region of He (He II to He III) and that the primary engine of the pulsation is the κ mechanism. This κ mechanism reflects the opacity of stars and depends on the atoms involved, density, the temperature, and on the ionization of matter:

$$\kappa = \frac{\kappa_0 \rho^n}{T^s} \quad (2.1)$$

where κ_0 is a constant while T and ρ are the temperature and density of the star, respectively.

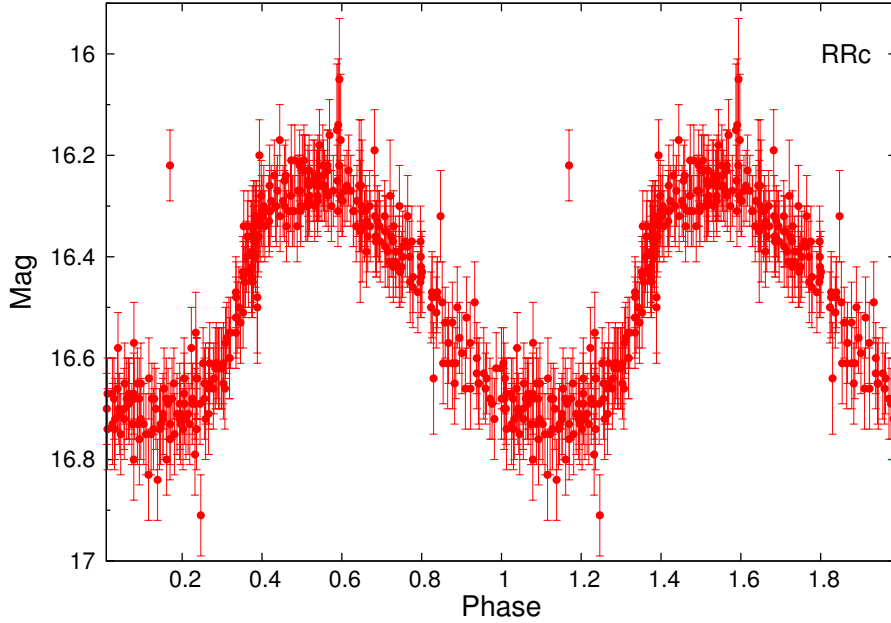


Figure 2.2: Illustration of one of our RRc stars showing the symmetric behavior of their phased light curves and their small amplitudes compared to RRab stars.

Outside ionization zones ($s, n \sim 1, 3.5$), if a star is compressed, the temperature rises while the radiation flow increases and the opacity decreases ($\kappa \sim \frac{\rho^1}{T^{3.5}}$). Thus, the unionized zones do not act as the primary engine of the pulsation in the case of RRL stars (and pulsating stars in general) as in the latter case the maximum in opacity occurs at the maximum compression (Eddington, 1926).

On the other hand, if a star is compressed, s drops to zero or to negative values inside an ionized zone. The ionization releases free electrons and increases the opacity of the zone. As a result, the radiation gets trapped inside the ionization layer (i.e., helium layer), resulting in outward pressure.

As the zone is driven outwards by pressure, the star cools down and a recombination of the ionized material takes place. This results in a decrease in the opacity and a decrease in the outward pressure. The zone gets compressed again. Thus, the κ mechanism in the ionized zones act as the primary engine of pulsation. These zones act against any pulsation movement, making the star unstable to pulsation.

The different pulsation scenarios that the RRab and RRc stars exhibit are reflected by the shape of their light curves (see Section 2.3) is mainly due to the difference in the temperatures between different types of RRL stars. For instance, RRc stars are hotter than RRab and are thus more unstable towards overtone pulsations.

At the same time, the γ mechanism acts as a secondary driver of pulsation. Specifically, the γ mechanism acts as a reinforcement of the κ mechanism in partial ionization zones. Because the temperature in the partial ionization zone is lower than in the adjacent stellar layers, heat tends to flow into the zone during compression, prompting further ionization. Thus, if a star is compressed, the energy which would normally increase the temperature outside ionization zones will go into increasing the ionization levels, which in return maximize the opacity level at maximum compression.

We show the SDSS phased light curve of a RRc star (upper left) and a candidate eclipsing binary (upper right) in Figure 2.4. The best-fitted templates from Sesar et al. (2010) correspond to RRc stars and are plotted in solid yellow lines. Although the latter light curves correspond to different types of stars, both of their best-fitted light curves correspond to RRc stars. This example reflects the difficulty in correctly classifying RRc stars due to their symmetric

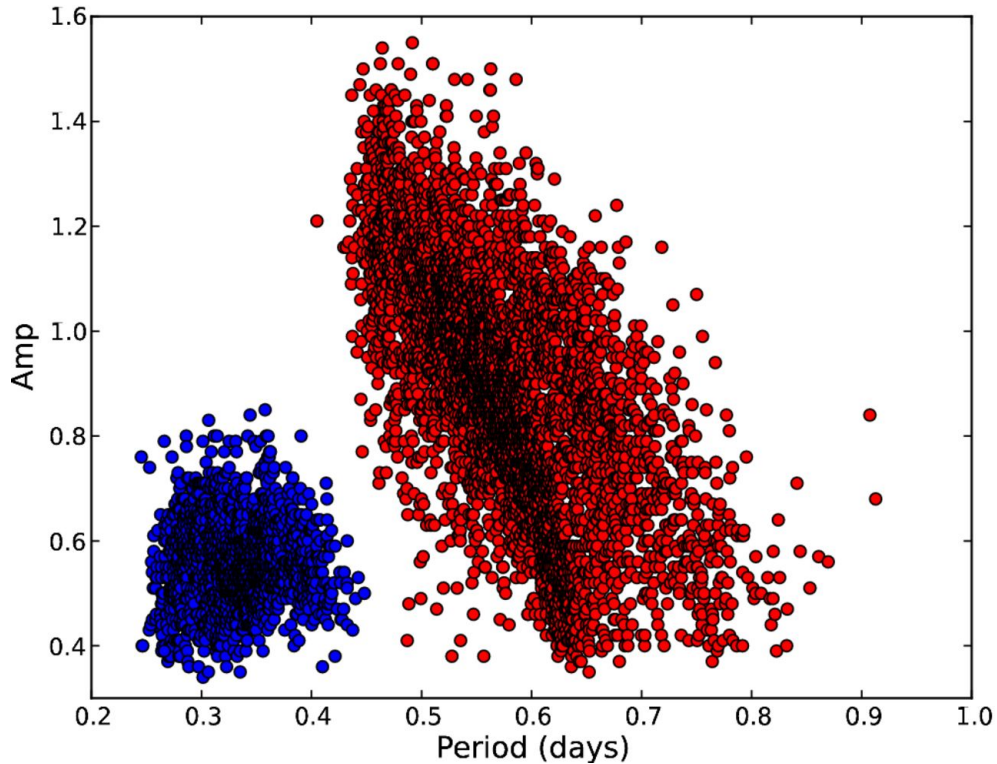


Figure 2.3: The P–A distribution for the RRab (red dots) and RRC (blue dots) stars from Abbas et al. (2014a).

light curves discussed in Section 2.3. On the other hand, the change in the $(g-r)$ color for the RRC star and the candidate eclipsing binary are shown in the lower left and lower right panels of Figure 2.4, respectively. The $(g-r)$ color change (which reflects changes in temperature) for the RRC stars is much more significant than that for the eclipsing binary. This illustrates how the temperature changes during the pulsation cycles of RRL stars (Sesar et al., 2010).

2.5 The Blazhko Effect

When Sergey Blazhko detected a modulation in the phase of the “RW Dra star” (Blazhko, 1907) and when Shapley detected amplitude modulation in the “RR Lyrae star” (Shapley, 1914), it was clear that RRL stars experience a long-term variations in their periods and amplitudes, the so called Blazhko effect. The origin of the Blazhko effect is still not well understood but it has been suggested that the modulations in the periods and amplitudes are due to resonance between the fundamental radial mode and the ninth overtone (Buchler & Kolláth, 2011). To illustrate the Blazhko effect, we show in Figure 2.5 a light curve from the Convection Rotation and Planetary Transits satellite mission (CoRoT, Chadid et al. 2010) of an RRab star (CoRoT ID 0105288363) that is exhibiting the Blazhko effect. This star which has been observed 24000 times during 145 days by the CoRoT have a pulsation period of ~ 0.5676 d (Chadid et al., 2011). Variations in the light curve due to the irregular Blazhko effect are clearly visible over four Blazhko cycles in Figure 2.5.

Different systematic surveys have shown that at least 40% of the RRab stars undergo the Blazhko effect (i.e., Jurcsik et al. 2009). Although it was originally believed that RRC stars do not exhibit the Blazhko effect, it has been

Table 2.1: The Oosterhoff Groups

Oo Cluster Type	$\langle P_{ab} \rangle$ (d)	$\langle P_c \rangle$ (d)	Fraction of RRc stars
OoI	0.55	0.32	17%
OoII	0.65	0.37	44%

recently shown that 5%–40% of them exhibit the latter effect (i.e., Kolenberg et al. 2010; Kunder et al. 2013). However, it is sometimes difficult to confirm or refute the Blazhko effect as it requires a very precise photometry, specially in globular clusters where crowding and blending issues are present. Recently, $> 10\%$ of the known Blazhko RRL stars were discovered (Bramich et al., 2014) using the time-domain data from the Qatar Exoplanet Survey (QES, Alsubai et al. 2013).

2.6 The Oosterhoff Effect

While studying the P–A distribution of RRL stars in different globular clusters, Oosterhoff (1939) noticed two different types of globular clusters that were later named OoI and OoII clusters.

The first main difference between OoI and OoII clusters is in the mean periods of their RRL stars. The mean period of RRab stars in OoI clusters is $\langle P_{ab} \rangle = 0.55$ d compared to $\langle P_{ab} \rangle = 0.65$ d for RRab stars in OoII clusters. Likewise, the mean periods of RRc stars in OoI and in OoII clusters are $\langle P_c \rangle = 0.32$ d and $\langle P_c \rangle = 0.37$ d, respectively. Another major difference between OoI and OoII clusters is in the ratio of their RRc stars. The ratio of RRc stars in OoI clusters is small ($\sim 17\%$) compared to the same ratio in OoII clusters ($\sim 44\%$). These values are listed in Table 2.1. Finally, OoI clusters are more metal-rich ($[\text{Fe}/\text{H}] > -1.7$ dex) than OoII clusters ($[\text{Fe}/\text{H}] < -1.7$ dex). These values are adopted from Smith (1995) and De Lee (2008).

In addition to the OoI and OoII groups, some globular clusters originating from dSph satellite galaxies are classified as Oosterhoff intermediates as they fall in the Oosterhoff gap ($0.58 < \langle P_{ab} \rangle < 0.62$ d) in the P–A diagram (Catelan, 2009). This is called the Oosterhoff dichotomy.

In the left panel of Figure 2.6, we show the $[\text{Fe}/\text{H}]$ vs. $\langle P_{ab} \rangle$ distribution of globular clusters in the Milky Way. The latter figure illustrates how most of the globular clusters avoid the Oosterhoff gap. The right panel of Figure 2.6 shows the same distribution as the left panel in addition to dSph satellite galaxies of the Milky Way and their globular clusters. The Oosterhoff gap which is avoided by the RRL stars in globular clusters of the Milky Way seems to be filled by systems associated with the dSph satellite galaxies of the Milky Way. This difference in the distribution between globular clusters and the systems associated with the dwarf satellite galaxies in the Milky Way reflects the difference in their formation scenarios and properties.

Although the Oosterhoff dichotomy is not well understood, it is believed that it is caused by different factors like the metallicities, ages, and He abundances of the clusters (Clement et al., 2001; Catelan, 2009; Dotter et al., 2010; Smith et al., 2011; Contreras Ramos et al., 2013; Kennedy et al., 2014; Zinn et al., 2014).

Because different Oosterhoff groups in globular clusters seem to indicate different populations and formation histories, detecting the Oosterhoff groups in field stars in the Galactic halo can help in understating its formation history (i.e., Catelan 2006; Miceli et al. 2008; Catelan 2009; Cusano et al. 2013; Garofalo et al. 2013; Abbas et al. 2014d). See Section 3.7 for a review about previous studies that investigated the Oosterhoff effect and Chapter 6 for a detailed study that we conducted about the latter effect.

2.7 Summary

Although Williamina Fleming was the first to observe the prototype “RR Lyrae star” in 1899, it was Pickering who published its data in the *Harvard Second Catalog of Variable Stars*. RRL stars are periodic-variables with periods less than ~ 1 day. They are low-mass, horizontal-branch stars that are burning helium in their cores. Because they have

a well-defined average magnitude of $M_v \sim 0.6 \pm 0.1$ mag, they have been extensively used as standard candles to measure galactic distances.

The two most common subtypes of RRL stars are the RRab and RRC stars. RRab stars pulsate in the fundamental mode, have a mean period $\langle P_{ab} \rangle$ of ~ 0.57 d, and have very distinctive asymmetric light curves (fast rise and slow decrease in their brightness). RRC stars on the other hand pulsate in the first overtone, have smaller amplitudes and periods than RRab stars, symmetric light curves, and a mean period of ~ 0.34 d (Smith, 1995). Because of the unique shape of their light curves, it is relatively easier to identify RRab stars than to identify RRC stars.

The primary engine of the pulsation of RRL stars is the κ mechanism that is driven in the second ionization region of He. In this case, the opacity reaches a maximum during compression. When the RRL star is compressed, free electrons are released in the ionization zone. These electrons increase the opacity which in return trap the radiation inside the ionization layer. As a result, an outward pressure is created. During the expansion due to the outward pressure, the temperature, opacity, and outward pressure decrease and a recombination of the ionized material takes place. The secondary engine of pulsation is the γ mechanism. In the partially ionized zone, the energy which increases the temperature during compression goes into increasing the ionization levels, which in return maximize the opacity level at maximum compression. Thus, the γ mechanism acts as a reinforcement of the κ mechanism as it contribute in increasing the opacity during compression.

Although the Blazhko effect and the Oosterhoff dichotomy have been investigated for almost a century, the physics behind them have not been fully understood. The Blazhko effect which is the long-term modulations in the periods and amplitudes of RRL stars affect $\sim 40\%$ of the RRab stars and $5\%–40\%$ of RRC stars. It is believed that these modulations are due to resonance between the fundamental radial mode and the ninth overtone. On the other hand, the Oosterhoff effect which is represented in Figure 2.6 divides globular clusters into three different types: OoI clusters, OoII clusters, and Oo intermediate clusters. RRab stars in OoI clusters have $\langle P_{ab} \rangle = 0.55$ d and $\langle P_c \rangle = 0.32$ d while those in OoII clusters have $\langle P_{ab} \rangle = 0.65$ d and $\langle P_c \rangle = 0.37$ d. Additionally, OoI clusters are more metal-rich than OoII clusters.

The Oo intermediate clusters have periods in the Oosterhoff gap $0.58 < \langle P_{ab} \rangle (d) < 0.62$. Although this gap is usually avoided by the globular clusters, it seems to be filled with systems associated with the dwarf satellite galaxies of the Milky Way. This difference in the distribution between globular clusters and the systems associated with the dwarf satellite galaxies in the Milky Way reflects the difference in their formation scenarios and properties. Although the Oosterhoff dichotomy is not well understood, it is believed it is caused by different factors like the metallicities, ages, and He abundances of the clusters.

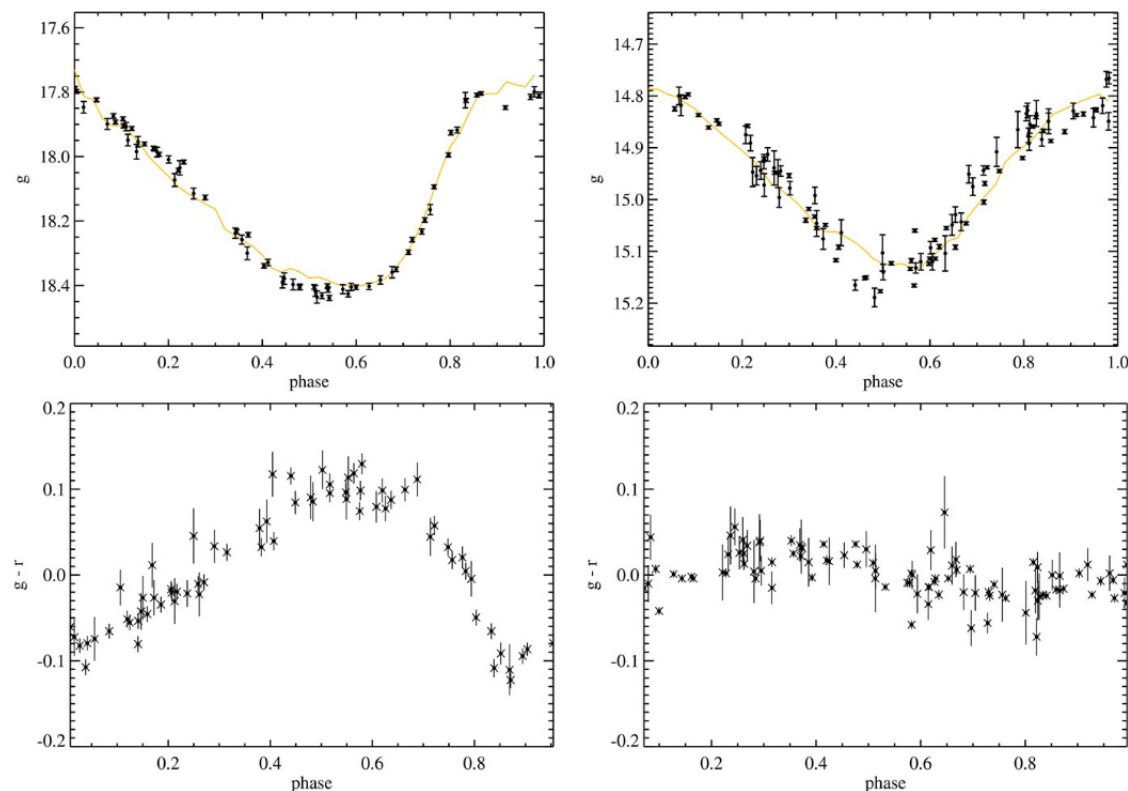


Figure 2.4: Illustration of the temperature change during the pulsations of RRL stars. Upper panel: The SDSS phased light curve of a RRC star (left) and a candidate eclipsing binary (right). The best-fitted templates that are shown as solid yellow lines show similar light curves. Lower panel: The $(g-r)$ color variation of the same RRC star (left) and the candidate eclipsing binary (right) are plotted. It is clear how the change in the $(g-r)$ color (which reflects the change in temperature) of the RRC star is much more significant than the color change for the candidate eclipsing binary. Figure from Sesar et al. (2010).

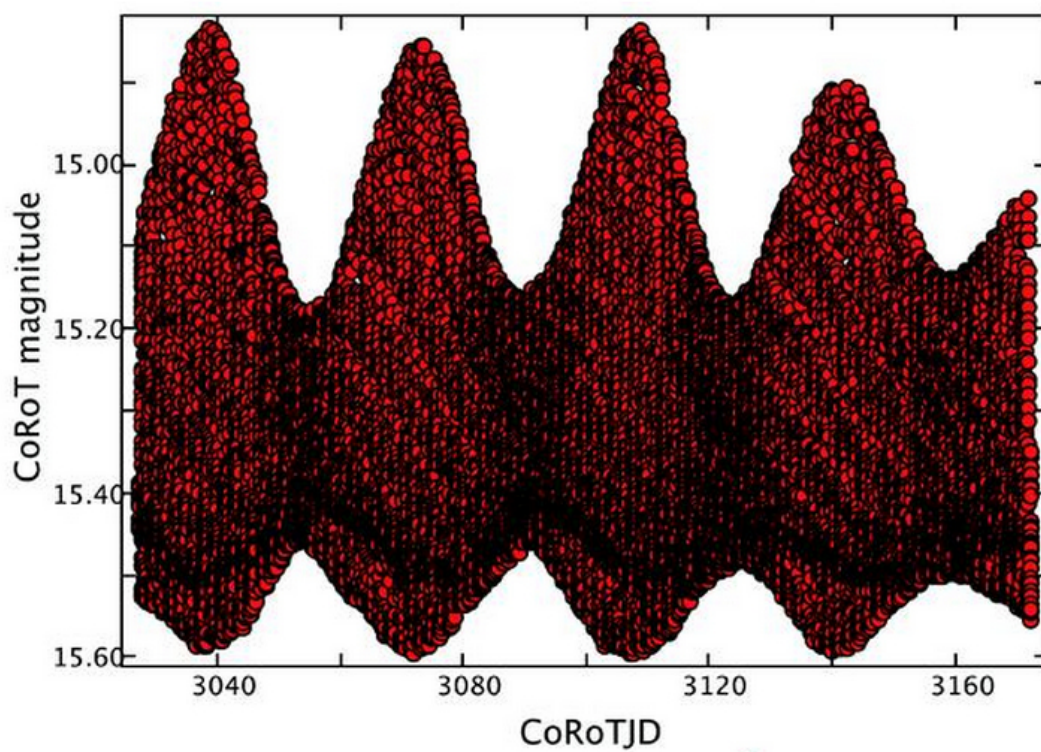


Figure 2.5: CoRoT light curve of a RRab star (ID 0105288363) that is exhibiting the Blazhko effect. The variation of the amplitudes over four Blazhko cycles are clearly observed. Figure from Chadid et al. (2011).

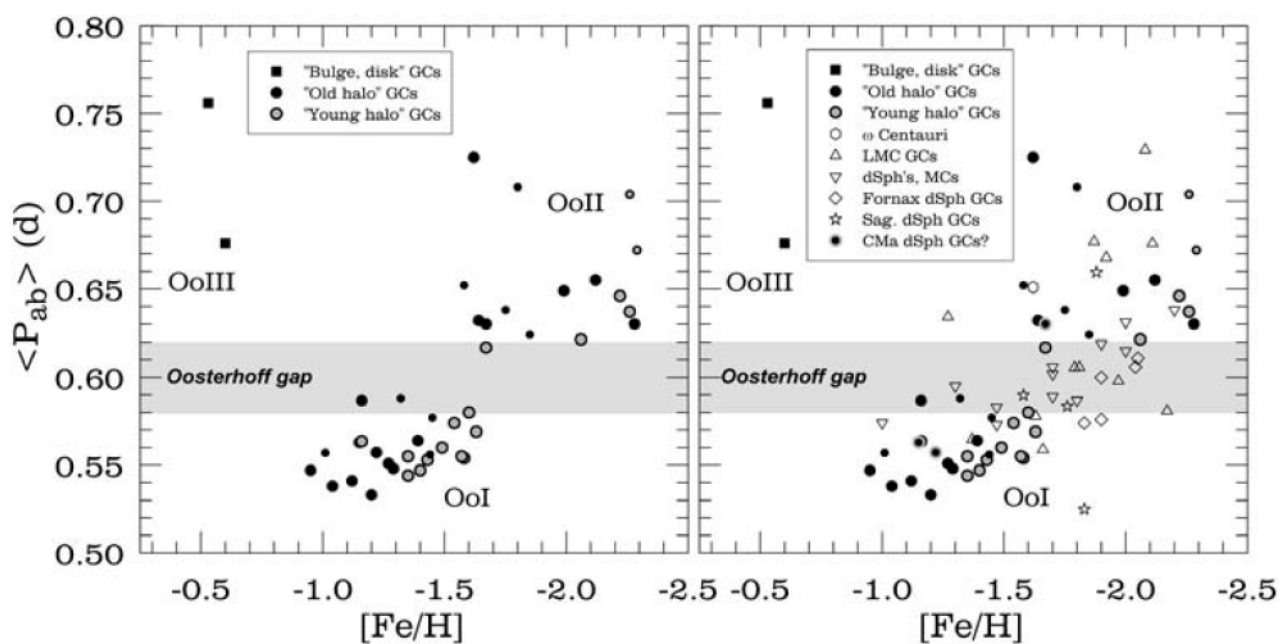


Figure 2.6: The $[Fe/H]$ vs. $\langle P_{ab} \rangle$ distribution of globular clusters in the Milky Way is plotted in the left panel. The right panel shows the same distribution for the same globular clusters in addition to dwarf satellite galaxies and systems associated with them. Figure from Catelan (2009).

Used Data And Surveys

I say to you that everything has will. Even the stone, apparently so deaf, and dumb and lifeless, is not without a will. Else would it not have been, and would it not affect a thing, and nothing would affect it. The Book of Mirdad, Michael Naimy

Abstract Motivated by different scientific questions, astronomers have always focused on developing new and large sky surveys. Different surveys are designed differently according to their major goals. For instance, if a survey is aimed to study variable stars, it needs to be designed in a way to repeatedly observe the sky, preferably using at least two bandpasses. Fortunately, data from many of the sky surveys have been made publicly available. Taking advantage of that, we use data from different sky surveys and we exploit their strong points to mitigate other weak points of the same surveys. We also use previously published catalogs of RRL stars to test our methods and results. In this chapter, these surveys and catalogs will be introduced and explained.

3.1 Introduction

We explain the observational properties and techniques, the filters, the characteristics, and the different properties of all the telescopes and surveys used in this work in Sections 3.2, 3.3, 3.4, 3.5, and 3.6. In Section 3.7, we discuss some of the previous studies that detected RRL stars. We also introduce the methods they adopted and their major results.

3.2 The Panoramic Survey Telescope and Rapid Response System 1 (Pan-STARRS1)

The Panoramic Survey Telescope and Rapid Response System 1 (Pan-STARRS1) was mainly designed to detect potentially hazardous asteroids and near Earth objects (NEOs; Kaiser et al. 2002). Because it is a deep survey that is repeatedly observing three quarters of the sky, its data are of interest for a wide range of different scientific topics. These topics cover different science areas, from solar system objects to cosmology. The Pan-STARRS1 data are of particular interest also for structural studies of the Milky Way affording a deeper and wider area coverage than previous surveys.

Pan-STARRS1 consists of two sub-surveys: the Pan-STARRS1 3π (hereafter PS1) survey and the Pan-STARRS1 Medium Deep Field (hereafter PS1-MD).

3.2.1 The PS1 Survey

The PS1 survey (Kaiser et al., 2002) is a ~ 3.5 -year (May 2010 – March 2014) multi-epoch photometric and astrometric survey that was observing from Haleakala, Hawaii. One of its goals is to carry out a photometric and astrometric survey of stars in the Milky Way and the Local Group. It used a 1.8-m telescope with a 7 deg^2 field of view to patrol $\sim 30000 \text{ deg}^2$ of the sky (north of declination -30°) between ~ 10 and 50 times during its three and a half years period of operation. Specifically, it was designed to take four exposures per year and area with each of its filters using the largest digital camera in the world (1.4 Gigapixels). The PS1 used 5 bandpasses (g_{P1} , r_{P1} , i_{P1} , z_{P1} , and y_{P1}) that cover the optical and near-infrared spectral range ($4000 \text{ \AA} < \lambda < 10500 \text{ \AA}$). The transmission curves as a function of wavelength are shown in the upper panel of Figure 3.1. Its exposure times are filter-dependent and vary between 30s in z_{P1} and y_{P1} and ~ 45 s in g_{P1} , r_{P1} , and i_{P1} . The PS1 goes as deep as 23.1, 23.0, 22.7, 21.9, and 20.9 in g_{P1} , r_{P1} , i_{P1} , z_{P1} , and y_{P1} respectively, in co-added images. Individual g_{P1} , r_{P1} , i_{P1} , z_{P1} , and y_{P1} exposures have limiting magnitudes of 21.9, 21.8, 21.5, 20.7, and 19.7, respectively (Morganson et al., 2012).

3.2.2 The PS1-MD Survey

Pan-STARRS1 was designed to extensively observe 10 fields (each is 7 deg^2) that are spaced approximately uniformly around the sky, i.e., the PS1-MD survey. The central coordinates of these fields are listed in Table 3.1. The PS1-MD survey obtained deep and multi-epoch images in the same g_{P1} , r_{P1} , i_{P1} , z_{P1} , and y_{P1} bands used in the PS1 3π survey. However, the exposure times of the PS1-MD survey are much longer than the ones for the PS1 3π survey. At the same time, at least seven of the 10 PS1-MD fields were observed every night. Thus, every footprint was observed ~ 140 times under good-photometric conditions in each year.

3.3 The SDSS

The SDSS (Fukugita et al., 1996; York et al., 2000) is a deep photometric and spectroscopic survey containing more than 900000 galaxies and 110000 quasars. The SDSS (York et al., 2000), which has been in operation since 2000 April, uses a 2.5-m telescope located at Apache Point Observatory in New Mexico to image $\sim 12000 \text{ deg}^2$ of the sky. One part of the SDSS is a multi-wavelength imaging survey (in u , g , r , i , and z) that goes as deep as 22.3, 23.3, 23.1, 22.3, and 20.8 in u , g , r , i , and z , respectively (Morganson et al., 2012). We plot the transmission curves of these filters in

Table 3.1: MDF Fields Central Locations. Both equatorial J2000.0 R.A. and Dec. are given in decimal degrees.

MDF field name	R.A. (center)	Dec. (center)
MD01	35.87	-4.25
MD02	53.10	-27.80
MD03	130.59	44.31
MD04	150.00	2.20
MD05	161.91	58.08
MD06	185.00	47.11
MD07	213.14	53.41
MD08	242.78	54.95
MD09	333.68	0.28
MD10	351.97	-0.43

the lower panel of Figure 3.1. The exposure times of the SDSS filters are listed in Table 3.2. The SDSS has created the most detailed three-dimensional maps of the Universe ever made.

Most of the SDSS data are based on single epoch observations with the exception of the overlapping regions of adjacent scans and of Stripe 82 ($-50^\circ < \text{R.A.} < 59^\circ$, $-1.25^\circ < \text{Dec.} < 1.25^\circ$). Stripe 82 covers $\sim 270 \text{ deg}^2$ of the Southern Galactic hemisphere and have been observed ~ 80 times by the SDSS.

3.4 The Catalina Real-Time Transient Survey (CRTS)

Aiming to discover rare and interesting transient phenomena (i.e., optical transients, NEOs, etc.), the Catalina Real-Time Transient Survey (CRTS, Drake et al. 2009, 2013a) uses three different surveys and telescopes: the Catalina Sky Survey (CSS), the Mt. Lemmon Survey (MLS), and the Siding Spring Survey (SSS). While the CSS and MLS are carried out with two different telescopes located in Tucson, Arizona, the SSS uses a third telescope in Siding Spring, Australia. Each telescope is equipped with an unfiltered $4k \times 4k$ CCD. 2500 deg^2 of the sky are covered by these telescopes every night (Drake et al., 2013a). In order to avoid crowded stellar regions, the CRTS avoids the Galactic plane region by 10° – 15° (Drake et al., 2014). In total, it observes around 33000 deg^2 of the sky ($-75^\circ < \text{Dec.} < 70^\circ$ and $|b| > 10^\circ$).

Using the SExtractor photometry software, the second photometric catalog from the Catalina Survey (CSDR2) was released and is now available online¹. The CSDR2 contains seven years of observations taken between 2005 and 2011 using the CSS, MLS, and SSS telescopes. The CSDR2 data are available for ~ 500 million objects with V -band magnitudes between 11.5 and 21.5 mag.

3.4.1 The CSS

The CSS which started operating in April 1998, uses a 0.7-m Schmidt telescope and is located ~ 2500 meters above the sea level. It uses an unfiltered CCD with a 2.5 arcsec pixel scale providing an 8 deg^2 field of view (Drake et al., 2013a). The CSS bright and faint magnitude cut-offs are ~ 11.5 and 19.5 mag, respectively. Its typical exposure time is 30 seconds.

¹<http://nesssi.cacr.caltech.edu/DataRelease/>.

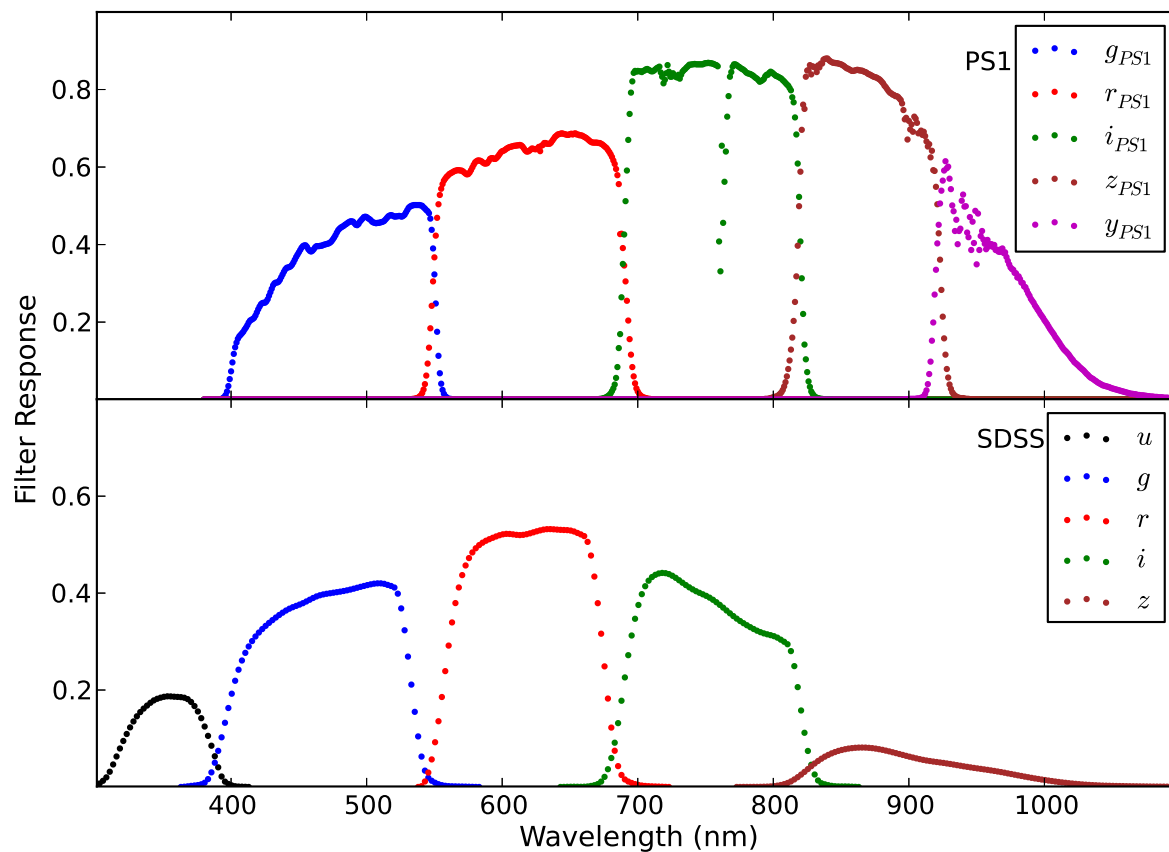


Figure 3.1: Upper panel: transmissions of the PS1 g_{P1} , r_{P1} , i_{P1} , z_{P1} , and y_{P1} filters as a function of wavelength are shown. Lower panel: same as the upper panel but showing the transmission curves of the SDSS u , g , r , i , and z filters. Data for the upper and lower panel are taken from the PS1 (<http://ps1sc.ifa.hawaii.edu/>) and SDSS (<https://www.sdss3.org/>) websites, respectively.

3.4.2 The SSS

The SSS telescope is a 0.5-m Schmidt telescope with a computing system identical to that of the CSS telescope. The SSS telescope began operating in April 2004 and can detect objects with V -band magnitudes between ~ 11.5 and 19.0 mag using a CCD camera with a 1.8 arcsec pixel scale and 4.2 deg² field of view.

3.4.3 The MLS

The largest telescope used in the CRTS is the MLS telescope. It is a 1.5-m Cassegrain reflector telescope equipped with an unfiltered CCD (1 deg² field of view and 1 arcsec pixel scale). The MLS can detect objects as bright as $V \sim 11.5$ mag and as faint as $V \sim 21.5$ mag, which makes it more sensitive than the CSS and SSS. However, the CSS and SSS cover a much larger area of the sky than the MLS.

3.5 The Quasar Equatorial Survey Team RRL Stars Survey (QUEST)

The Quasar Equatorial Survey Team (QUEST) RRL Stars Survey used a 1-m Schmidt telescope located at 3610 meters elevation at the Llano del Hato Observatory in Venezuela and covered 380 deg² of the sky (Vivas et al., 2004). The QUEST RRL Stars Survey used the QUEST camera, which is a 16 CCDs mosaic with 2048 \times 2048 pixels per CCD (1.02 arcsec pixel scale). These CCDs were arranged in a 4 \times 4 array and the entire camera had a field of view of 2^o.3 \times 2^o.3. The QUEST camera allows simultaneous multi-filter photometry as it is designed to operate in a drift-scanning mode. Stars would then pass through the four different filters in the different CCD chips almost simultaneously, similar to the drift-scan imaging technique used in the SDSS.

3.6 The La Silla QUEST (LSQ) Southern Hemisphere Variability Survey

The La Silla QUEST (LSQ) Southern Hemisphere Variability Survey used a 1-m Schmidt Telescope at the La Silla Observatory in Chile to observe ~ 1000 deg² per night (Hadjiyska et al., 2012). It was mainly designed to study supernovae, RRL stars, quasars, and trans-Neptunian objects. The survey is equipped with a broad-band filter (4000–7000 Å) and a camera that consists of 112 CCD detectors. The camera covers an area of 4. ^o6 \times 3. ^o6 on the sky. Every one or two days, the LSQ Southern Hemisphere Variability Survey observes the same patch of the sky for 60 seconds twice. These exposures are separated by ~ 2 hours (Hadjiyska et al., 2012; Zinn et al., 2014).

The filters and exposure times used by these surveys are listed in Table 3.2.

3.7 RRL Star Surveys

In this section, we will discuss the properties of some of the surveys that searched for RRL stars. We will also explain the different methods used in the different studies. At the same time, we will focus on the surveys that we used in our work. Note that the goals of these searches varies from one survey to another.

- The QUEST catalog of RRL stars contains 498 RRL stars (Vivas et al., 2004) in ~ 380 deg² of the sky. It is based on V -band observations to a limiting magnitude of $V \sim 19.5$ mag, taken over ~ 2.3 years (Vivas et al., 2004). According to Vivas & Zinn (2006), 41 out of the 498 stars are not true variables. These 41 stars were

Table 3.2: Exposure times of all the filters in the PS1 3π , PS1-MD, SDSS, CRTS, QUEST, and LSQ surveys.

Survey	Filter	Exposure Time (s)
PS1 3π	g_{P1}	43
	r_{P1}	40
	i_{P1}	45
	z_{P1}	30
	y_{P1}	30
PS1-MD	g_{P1}	113
	r_{P1}	113
	i_{P1}	240
	z_{P1}	240
	y_{P1}	240
SDSS	u, g, r, i, z	~ 54
CRTS (CSS, SSS, MLS)	unfiltered	~ 30
QUEST	U, B, V, R, I, H_α ^a	$\sim 60\text{--}140$
LSQ	unfiltered	~ 60

^aFour different filters can be selected in each scan.

found in crowded regions and the photometric pipeline that was used by QUEST did not include a de-blending algorithm at that time. Consequently, only the remaining 457 stars are used in our work.

- Miceli et al. (2008) detected 838 RRab stars using data from the Lowell Observatory Near Earth Objects Survey Phase I (LONEOS-I, Howell et al. 1995). These stars have been observed between 28–50 times, are distributed around 1430 deg^2 of the sky and have d_h in the $\sim 3\text{--}30$ kpc range. In addition to studying the properties and spatial distribution of the stellar halo, Miceli et al. (2008) clearly observed the different Oosterhoff components. They detected the OoI and OoII components of RRab stars and showed that these components have different radial distributions. Miceli et al. (2008) suggested that the OoI and OoII RRab have dual mode formation scenarios, and that these two components indicate multiple physical mechanisms for the formation of the halo.
- Watkins et al. (2009) and Sesar et al. (2010) used data from the SDSS to look for RRL stars in Stripe 82, which was observed around 80 times. The Watkins et al. (2009) and Sesar et al. (2010) catalogs contain 407 and 483 RRL stars in Stripe 82, respectively, with d_h in the $\sim 4\text{--}120$ kpc range. Because Sesar et al. (2010) used wider color ranges than the ones used by Watkins et al. (2009), Sesar et al.'s (2010) catalog of RRL stars (379 and 104 RRab and RRc, respectively) is more complete. According to Sesar et al. 2010, their catalog has efficiency (fraction of true RRL stars in the candidate sample) and completeness (the fraction of selected RRL stars) levels of $\gtrsim 99\%$. Hence, we use the latter catalog as a comparison catalog to compute the efficiency and completeness levels in our work. The light curves, periods, amplitudes, and properties of these stars are all discussed in their paper. Sesar et al. (2010) used their discoveries to map the spatial distribution of the halo RRL stars in the 5–120 kpc Galactocentric distance range and were able to detect halo stellar streams and overdensities.
- Using the SDSS and the Lincoln Near Earth Asteroid Research survey (LINEAR; Sesar et al. 2011b), Sesar et al. (2013) announced the discovery of ~ 5000 RRL stars with d_h in the 5–30 kpc range that cover $\sim 8000 \text{ deg}^2$ of the sky. LINEAR has no spectral filters and has a mean number of 250 observations per object. These RRL stars were selected using SDSS color cuts, LINEAR variability cuts, and light curve analysis. In their study,

they found evidence for the Oosterhoff dichotomy among field RRL stars and showed that the OoII RRL stars have a steeper number density profile than the OoI RRL stars. They also detected and studied seven candidate halo groups.

- The largest Galactic volume catalog for RRL stars was published using the CSS data in three separate studies (Drake et al., 2013a,b, 2014). In order to discover the CSS RRab stars, Drake et al. (2013a,b, 2014) applied the Welch-Stetson variability index (I_{WS} ; Welch & Stetson 1993) to separate variable from non-variable stars in the CSS data. They then looked for periodicity using the Lomb-Scargle periodogram analysis (LS; Lomb 1976) and measured the percentage time spent by the objects below the mean magnitudes using the M-Test (Kinemuchi et al., 2006). Finally, they calculated RRab periods using the Analysis of Variance (AoV; Schwarzenberg-Czerny 1989) technique. The CSS catalog of RRab stars from Drake et al. (2013a,b) provides the CSS identification numbers (ID_{CSS}), equatorial J2000.0 R.A. and Dec. coordinates, the average magnitudes from the Fourier fits to their light curves, periods in days, amplitudes of variation, number of observations (N_{CSS}), d_h , extinction based on the Schlegel et al. (1998) reddening map, and the ephemeris of the stars (see table 2 and table 1 of Drake et al. 2013a and Drake et al. 2013b, respectively). The combined catalogs from Drake et al. 2013a, Drake et al. 2013b, and Drake et al. 2014 contains ~ 17000 CSS RRab and ~ 5500 RRc stars and is $\sim 90\%$ complete for sources brighter than $V = 17.0$ mag (Drake et al., 2014). The CSS RRab stars cover ~ 20000 deg² of the sky to d_h up to ~ 60 kpc. In one of their studies, Drake et al. (2013a) used their ~ 12000 CSS RRab discoveries that are distributed around 20000 deg² of the sky to show that the OoI and OoII groups are distinctly revealed in the Galactic halo to d_h up to 60 kpc.
- Abbas et al. 2014a detected ~ 6371 RRL stars using the combined data of the SDSS, PS1, and CSS surveys. The RRL stars have d_h in the 4–28 kpc distance range and are distributed across ~ 14000 deg² of the sky. See Chapter 4 for full details.
- Using the CSS catalog of RRL stars from Drake et al. (2013a,b) (CSS Search 1, see Table 3.3), Simion et al. (2014) detected an excess of RRL stars in the direction of the HAC (Belokurov et al., 2007) and confirmed that the HAC is a distinct stellar halo substructure. They suggested that the HAC’s progenitor in the Southern hemisphere is a dwarf galaxy or a OoI globular cluster. They also noted the two Oosterhoff components using ~ 300 CSS RRab stars ($12 < d_h < 22$ kpc) located in the HAC.
- Zinn et al. (2014) studied the different Oosterhoff components, the halo substructures, and the density profile of the Galactic halo using 1013 RRab and 359 RRc stars that they discovered using data from the LSQ survey. Their RRL stars (LSQ catalog of RRL) covered ~ 840 deg² of the sky up to $d_h \sim 80$ kpc and have been observed between 11 and 300 times. Additionally, they studied the Oosterhoff components and period distribution of the Small and Large Magellanic Clouds using RRL stars from the Optical Gravitational Lensing Experiment (OGLE, Soszyński et al. 2009). Based on the $\langle P_{ab} \rangle$ values of the RRL stars associated with the leading stream of the Sagittarius dwarf spheroidal galaxy (Sgr dSph, Ibata et al. 1995), the Virgo Stellar Stream (VSS, Duffau et al. 2006), and the Small Magellanic Cloud, they suggested that the latter systems lie near the OoI and Oo intermediate boundary. They also detected very similar period distributions of the Large Magellanic Cloud and Sgr and a big difference between the same distribution of the Small and Large Magellanic Clouds. They found that the halo consists mainly ($\sim 73\%$) of OoI RRab stars and that at $R_{gc} \sim 25$ kpc, the RRL stars show a break in their number density distribution.
- Using the catalogs of variables objects from GALEX (Martin et al., 2005), Kinman & Brown (2014) studied the variability and properties of RRL stars in ultraviolet bands. The GALEX observed the whole sky using two bands: the FUV (1350–1750 Å) and the NUV (1750–2750 Å). They compared the fraction of low-amplitude RRL stars from Abbas et al. (2014a) to the same fraction in their catalog and found that the variability of RRL stars is more pronounced in the NUV bandpass. As illustrated in Figure 3.2, they found that the NUV pulsation amplitudes of RRL stars is roughly twice that of their V amplitudes. At the same time, they found that the $(NUV - V)$ color is more sensitive to metallicities and effective temperatures than optical colors (see Figure 1.5). Finally, they computed their completeness level ($\sim 50\%$) and found that it agrees with the one found by Abbas et al. (2014a). Specifically, their search yielded ~ 0.4 RRL stars per square degrees of the sky compared to ~ 0.455 RRL stars per square degrees from Abbas et al. (2014a).

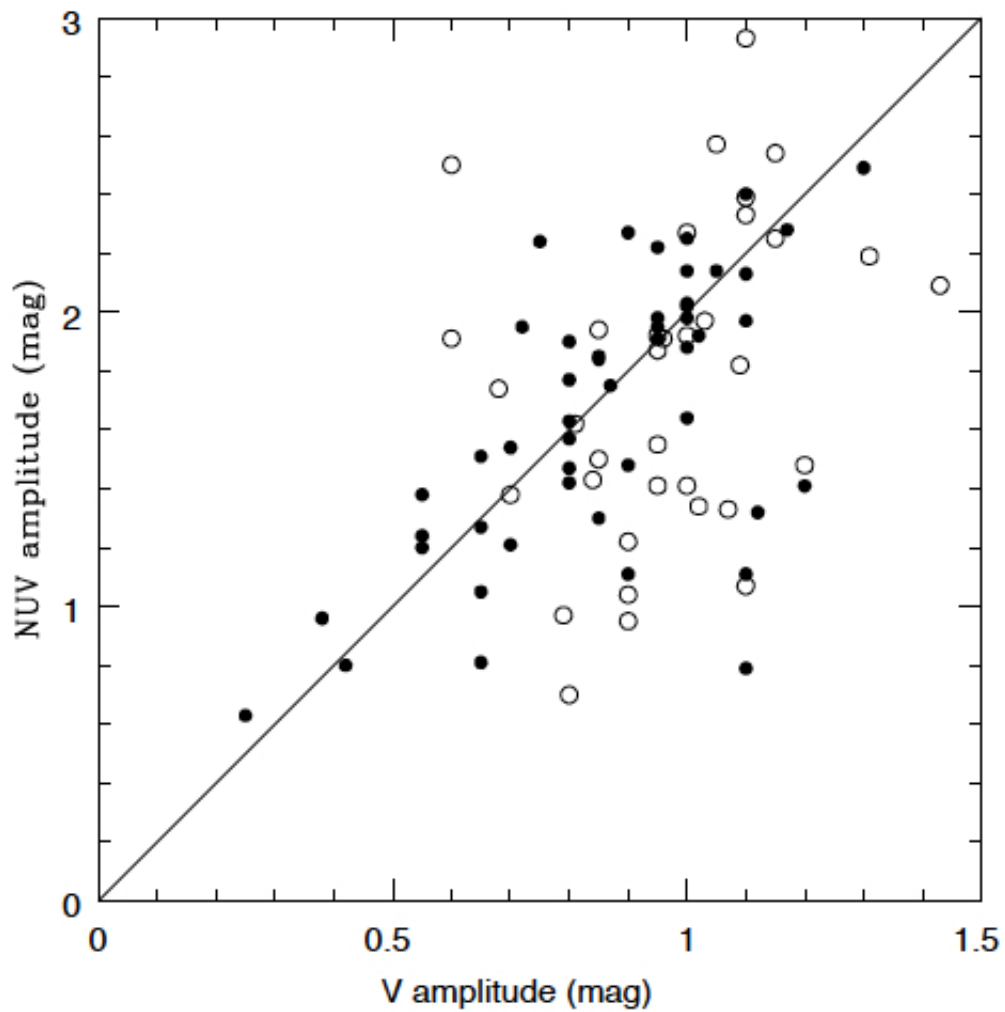


Figure 3.2: The amplitudes of RRL stars in the V band vs. the amplitudes of the same stars in the NUV band. RRL stars from the first and second catalogs of variable stars from GALEX are shown as open and filled circles, respectively. The solid line corresponds to the case where the NUV amplitude is twice the V amplitude. Figure from Kinman & Brown (2014).

Table 3.3: A brief summary for some of the RRL Star surveys.

Survey ^a	N_{RR} ^b	N_{RRab} ^c	N_{RRc} ^d	Max d_h (kpc) ^e	Covered Area (deg ²) ^f	Source
QUEST	457	360	97	70	380	Vivas et al. 2004
LONEOS-I	838	838	0	30	1430	Miceli et al. 2008
SDSS-Stripe 82	483	379	104	120	270	Sesar et al. 2010
LINEAR	4901	4067	834	30	8000	Sesar et al. 2013
CSS Search 1	14400	14400	0	60	20000	Drake et al. 2013a,b
CSS Search 2 (SDSS×PS1×CSS)	6371	4800	1571	28	14000	Abbas et al. 2014a
CSS Search 3	7904	2435	5469	60	20000	Drake et al. 2014
LSQ	1372	1013	359	80	840	Zinn et al. 2014

^aUsed survey

^bTotal number of RRL stars detected (RRab and RRc stars)

^cNumber of RRab stars

^dNumber of RRc stars

^eApproximate distance of the farthest RRL star detected

^fArea covered by the RRL stars

Our Newly Discovered RR Lyrae Stars

In God, there is no sorrow or suffering or affliction. If you want to be free of all affliction and suffering, hold fast to God, and turn wholly to Him, and to no one else. Indeed, all your suffering comes from this: that you do not turn toward God and no one else. Imam Al-Ghazali

Abstract We present the detection of 6371 RRL stars distributed across ~ 14000 deg² of the sky from the combined data of the SDSS, the PS1, and the CSDR2, out of these, ~ 2021 RRL stars (~ 572 RRab and 1449 RRc) are new discoveries. The RRL stars have heliocentric distances in the 4–28 kpc distance range. RRL-like color cuts from the SDSS and variability cuts from the PS1 are used to cull our candidate list. We then use the CSDR2 multi-epoch data to refine our sample. Periods were measured using the Analysis of Variance technique while the classification process is performed with the Template Fitting Method in addition to the visual inspection of the light curves. A cross-match of our RRL star discoveries with previous published catalogs of RRL stars yield completeness levels of $\sim 50\%$ for both RRab and RRc stars, and an efficiency of $\sim 99\%$ and $\sim 87\%$ for RRab and RRc stars, respectively. We show that our method for selecting RRL stars allows us to recover halo structures. The full lists of all the RRL stars are made publicly available.

This chapter is based on our published work : *Abbas, M., Grebel, E., Martin, N., Burgett, W., Flewelling, H., and Wainscoat, R. (2014a, MNRAS, 441, 1230)*

Available from: <http://mnras.oxfordjournals.org/content/441/2/1230.full>

4.1 Introduction

As mentioned in Chapter 1, one way of finding stellar streams and substructures is by identifying and mapping RRL stars in the halo. Many of the substructures that were discovered in the Milky Way were re-confirmed using RRL stars (i.e., Duffau et al. 2006; Watkins et al. 2009; Sesar et al. 2010). For more information about RRL stars, see Chapter 2.

The best and most reliable way to detect RRL stars is by using multi-band time series observations of a sufficiently high cadence and over a sufficiently long period. Since RRL stars are short-period pulsating stars with typical mean periods of ~ 0.57 and ~ 0.34 days for RRab and RRc stars (Smith, 1995), respectively, the time between observations is preferred to be short in order to sample the magnitudes of the stars at each phase. In addition to that, monitoring an RRL star over a long period of time will result in a more accurate and reliable classification and period determination.

In this chapter, we use and combine data from different sky surveys out of which each survey has a distinctive advantage that helps in identifying RRL stars with high efficiency, completeness, and reliability levels.

First, we apply color cuts to the SDSS (Fukugita et al., 1996; York et al., 2000), 8th data release (DR8; Aihara et al. 2011). Second, we apply variability cuts using data from the PS1 (Kaiser et al., 2002). Finally, we plot light curves and find the periods of the RRL stars using the CSDR2 (Drake et al., 2009, 2013a) which is based on seven years of multi-epoch observations. Using one of the surveys without the others to find RRL stars results in low efficiency and completeness levels.

In order to define the SDSS color selection threshold limits and the PS1 and CSDR2 variability threshold limits, we use the color and variability properties of the QUEST RRL star catalog (Vivas et al., 2004; Vivas & Zinn, 2006). To compute our efficiency and completeness levels, we compare our results with the RRL stars found in Stripe 82 (Sesar et al., 2010). See Section 3.7 and Table 3.3 for more information about the properties of the RRL stars from the QUEST and SDSS-Stripe 82 surveys.

Previous Studies

Drake et al. (2013a) had full access to the first photometric catalog of the Catalina Survey (CSDR1; Drake et al. 2009), which allowed them to look for RRab stars in the whole ~ 20000 deg² area of the sky that was covered by the CSDR1. On the other hand, we had to manually do a multiple object cone search for at most 100 objects at a time as more is not permitted by the public data interface. The CSDR1 RRL star catalog (Drake et al., 2013a) contains 12227 RRab stars found in the CSDR1 (Drake et al., 2009) database and covers stars with d_h up to 60 kpc. Because these authors were only interested in RRab stars and to avoid spurious detections, they removed all stars with periods outside the 0.43–0.95 days range. While our paper was nearing completion, Drake et al. (2013b) announced the discovery of ~ 2000 additional RRab stars in a re-analysis of the CSDR1 photometry and using additional data from the CSDR2. We refer to the latter two catalogs from Drake et al. (2013a) and (Drake et al., 2013b) as “CSS Search 1” in Table 3.3.

In this chapter, we use different variability statistics techniques than the ones used by Drake et al. (2013a) and Drake et al. (2013b) to find RRab stars. Unlike the latter two studies, we use template fitting techniques to help us in the classification process in addition to the visual inspection of all of the RRL candidate light curves. This allowed us to discover 646 additional RRab stars as compared to Drake et al. (2013a) and Drake et al. (2013b). We also found 1571 RRc stars, of which ~ 1449 stars are new discoveries.

The properties of the different surveys used in this study are described in Chapter 3. In Section 4.2, we describe our method for selecting RRL candidates within the overlapping area between the PS1 and the SDSS. Using the QUEST RRL stars, we define and apply our SDSS color cuts in Section 4.2.1 and our PS1 variability cuts in Section 4.2.2. In Section 4.3, we use the multi-epoch data from the CSDR2 database to look for stellar variability. The method used to find the periods of the RRL stars is described in Section 4.3.1. In Section 4.3.2, light curves are plotted and the methods used to distinguish RRL from contaminant (non-RRL) stars are described. Section 4.4 summarizes our results and provides our catalog of RRL stars. In Section 4.5, we compare our RRL star discoveries with the catalog of RRL stars in Stripe 82 (Sesar et al., 2010) to compute the efficiency and completeness levels of our method and periods. The properties of the RRL stars that we missed are also described in the same section. In Section 4.6, we compare our RRL star discoveries with the catalog of RRab stars from Drake et al. (2013a) and Drake et al. (2013b) and with the LSQ catalog of RRL stars (Zinn et al., 2014). We discuss our newly discovered RRL stars in Section 4.7 and we compare

them with stars found in the General Catalog of Variable Stars (GCVS¹; Samus et al. 2009). In Section 4.8, we find the distances for our RRL stars and we use these distances to recover previously known halo substructures. The results of this chapter are summarized in Section 7.1.

4.2 Identifying RRL stars

We start by using data from the overlapping area between the PS1 and the SDSS that cover $\sim 14000 \text{ deg}^2$ of the sky. We first select RRL candidates based on the SDSS $(u - g)$, $(g - r)$, $(r - i)$, and $(i - z)$ colors. As a variability cut, we use the multi-epoch data from the PS1 to distinguish variable from non-variable stars. Applying the SDSS color and PS1 variability cuts in this Section is necessary to reduce the number of light curves to be requested from the CSDR2 as the CSDR2 allows the retrieval of only 100 sky objects at a time.

4.2.1 The SDSS Color Cuts

Having different filters is a great advantage as it allows us to construct diagnostic color-color diagrams and consequently helps in having several color constraints for selecting and distinguishing RRL from contaminant stars. Although applying the SDSS color cuts will eliminate a large fraction of contaminant stars, contaminant stars with colors similar to the colors of the RRL stars will still be present (i.e., main-sequence stars with colors at the edge of the color range of the RRL stars, W UMa contact binary stars, Algol eclipsing binary stars, δ Scuti and SX Phe stars)

We study and identify the $(u - g)$ - $(g - r)$ SDSS colors of the QUEST RRL stars as this color-color diagram is the most sensitive and efficient in selecting RRL stars. Other single-epoch SDSS colors of RRL stars in the remaining SDSS filters were adopted from Sesar et al. (2010). In order to increase the efficiency of our color cuts, we define and use a $(u - g)$ - $(g - r)$ rhomboidal cut instead of a rectangular cut like the one used by Sesar et al. (2010). Additionally, we chose not to use the $(u - g)$ - $(g - r)$ colors of the RRL stars found in the catalog of RRL stars in Stripe 82 (Sesar et al., 2010) because we wanted to use the latter catalog as a test catalog to determine our efficiency and completeness levels, especially because that catalog is $\sim 100\%$ efficient and complete (Sesar et al., 2010). Using the $(u - g)$ - $(g - r)$ colors of Sesar et al.'s (2010) RRL stars in Stripe 82 would have biased the computation of our efficiency and completeness levels in Section 4.5. At the same time, we cannot accurately compute our efficiency and completeness levels by comparing our results with the QUEST catalog of RRL stars as the latter catalog is not complete (Vivas et al., 2004).

By positionally cross-matching the 457 QUEST RRL stars with the DR8 database, we obtained the u , g , r , i , and z magnitudes of these stars. We used a circle of 3 arcsec centered at the QUEST's positions. Out of the 457 RRL stars, 216 stars are recovered in the DR8 database having $12.0 < u < 19.0$. Most of the remaining missed RRL stars have magnitudes beyond our magnitude cut or do not have clean photometry in all of the 5 SDSS filters.

We adopted the above magnitude cut because the PS1 variability of faint ($u > 19.0$) and bright ($12.0 < u$) stars can be easily biased by the small number of the PS1 repeated observations currently available. Some of the PS1 data are affected by de-blending, cosmic rays, saturation, or non-photometric conditions as the PS1 final calibrated catalogs have not been produced yet. We will investigate much deeper areas of the sky when more PS1 epochs are available and the final PS1 calibrated catalogs are available.

Based on the SDSS colors of the 216 QUEST RRL stars, we define a color-color rhomboidal cut in the $(u - g)$ vs. $(g - r)$ diagram, which is presented in Figure 4.1. These colors are corrected for the line-of-sight interstellar extinction using the Schlegel et al. (1998) dust map. We believe that such color corrections can be applied to our stars as these stars are found at high Galactic latitudes in the halo where the overall extinction is small. The QUEST RRL stars with DR8 magnitudes are indicated by blue dots and the black rhomboidal box indicates our RRL candidates color-corrected selection box in the $(u - g)$ vs. $(g - r)$ diagram. Only stars that are plotted with red dots and that are found inside the black rhomboidal box are considered as RRL candidates and are retained for further analyses.

Figure 4.1 illustrates how RRL stars are distinguished in such a color-color diagram, which demonstrates the usefulness of applying such color cuts. RRL stars follow a trend in this color-color diagram. Their colors always spread out around the blue end of the main stellar locus. The farther away we go from the main stellar locus, the fewer contaminant stars we have. In addition to the $(u - g)$ - $(g - r)$ rhomboidal cut that we computed using the 216 QUEST

¹Published in 2012 and available from VizieR via <http://cdsarc.u-strasbg.fr/viz-bin/Cat?B/gcvs>

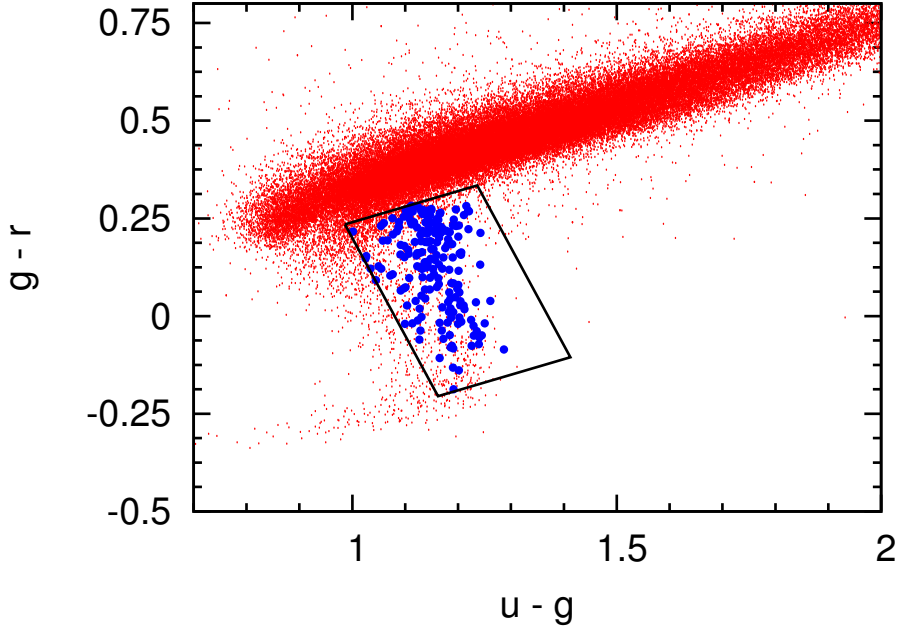


Figure 4.1: The $(u - g)$ vs. $(g - r)$ color-color diagram displaying the QUEST RRL stars with DR8 magnitudes in blue dots. The black rhomboidal box indicates our color-color selection cut. Stars that are plotted with red dots and are located inside the black rhomboidal box are considered as RRL candidates and are retained for further analyses. These colors are corrected for the line-of-sight interstellar extinction using the Schlegel et al. (1998) dust map.

Table 4.1: Our applied color cuts

$(g - r)_0 < 0.4 \times (u - g)_0 - 0.16$
$(g - r)_0 > 0.4 \times (u - g)_0 - 0.67$
$(g - r)_0 < -2.5 \times (u - g)_0 + 3.42$
$(g - r)_0 > -2.5 \times (u - g)_0 + 2.70$
$-0.25 < (g - r)_0 < 0.40$
$-0.20 < (r - i)_0 < 0.20$
$-0.30 < (i - z)_0 < 0.30$

RRL stars, we adopt other SDSS rectangular color cuts from Sesar et al. (2010). All our color cuts are listed in Table 4.1.

Since we use the catalog of RRL stars in Stripe 82 (Sesar et al., 2010) as a reference catalog to compute our completeness and efficiency levels in Section 4.5, computing our own $(u - g)$ - $(g - r)$ SDSS color cut using the QUEST RRL stars and then applying them to the stars found in Stripe 82 ensures that the completeness and efficiency levels we achieve are unbiased. Additionally, Sesar et al. (2010) use rectangular cuts while we use a $(u - g)$ - $(g - r)$ rhomboidal cut. The SDSS $(u - g)$ color serves as a surface gravity indicator for these stars. The range (~ 0.3 mag) and the rms scatter (~ 0.06 mag) are the smallest in this color (Ivezić et al., 2005).

Within the overlapping area between the PS1 and DR8, 308342 stars passed all the color cuts listed in Table 4.1.

4.2.2 The PS1 Variability Cuts

Because many stars passed the SDSS color cuts and because the CSDR2 allows us to do a manual search of only 100 sky objects at a time, we use the PS1 preliminary variability cuts to reduce the number of RRL candidates light curves to be retrieved from the CSDR2.

On average and at the end of the survey, the number of the PS1 pointings per object will be around 12 per filter. Taking chip gaps and dead cells into account, the PS1 observations per object will likely amount to about 9 times in each filter. While working on this paper, the average number of clean detections in the g_{P1} and r_{P1} filters were only ~ 5 . These are the “good” detections, which means that these detections were not saturated or blended, and were not flagged as cosmic rays (Morganson et al., 2012). We will include more epochs from the PS1 in future studies when the final calibrated catalogs from the PS1 are available.

The PS1 photometric catalog contains the average g_{P1} , r_{P1} , i_{P1} , z_{P1} , and y_{P1} magnitudes for each point source that were computed using the multi-epoch data available. It also contains the standard deviations (σ) that show the scatter of the single-epoch data about the average magnitudes in each filter. As a preliminary variability cut, we select stars with a standard deviation greater than 0.05 in g_{P1} ($\sigma_{g_{P1}}$) or in r_{P1} ($\sigma_{r_{P1}}$). The mean g_{P1} and r_{P1} errors are ~ 0.02 mag in both filters. Although this preliminary variability cut does not result in a clean sample of variable stars, it eliminates a large fraction of non-variable contaminant stars (i.e., main-sequence stars) and reduces the number of CSDR2 light curves to be requested. The PS1 variability statistics used in this study are based on ~ 5 epochs in two different filters where a single outlier can bias the statistics. Potential contaminant stars that can still be present after the preliminary variability cut include non-variable stars (i.e., main-sequence stars) with relatively large g_{P1} or r_{P1} photometric errors and non-RRL variable stars with colors similar to the colors of RRL stars.

Around 34200 stars (11% of the 308342 stars selected in Section 4.2.1) passed these two variability selection cuts. Most of the stars that passed our SDSS color cuts but not the PS1 variability cuts are main-sequence stars with colors close to the edge of the color range of the RRL stars. We use the CSDR2 multi-epoch data in the next section to obtain a clean list of variable stars and to carry out a light curve analysis.

4.3 The CSDR2 Light Curves

We extract the CSDR2 light curves for the stars that passed the SDSS color and the PS1 variability cuts. We searched for all of our ~ 34200 RRL candidates and found ~ 21050 stars in the CSDR2 database. The remaining stars were either not observed with the Catalina Survey, or were found in crowded regions. We used a circle of 3 arcsec centered at the DR8 positions. The mean number of epochs for these stars in the CSDR2 database is 270. More than 90% of these stars were observed more than 100 times. The number of CSDR2 observations per star as a function of equatorial J2000.0 R.A. and Dec. is illustrated in Figure 4.2 where the values are color-coded according to the legend. Because 90% of the stars have more than 100 epochs, the CSDR2 variability statistics and light curve analyses were sufficient and very accurate to reliably distinguish RRL from contaminant stars.

In order to get rid of possible outliers, we omit data points that are more than 3σ from the CSDR2 mean magnitudes (Mag) for each star. This step ensures a reliable variability statistics and better phased light curves (light curves folded using a specific period). This is because some of the CSDR2 observations were taken under non-photometric conditions and sometimes possibly due to the recalibration process itself. Potential outliers can also be contaminated by cosmic rays.

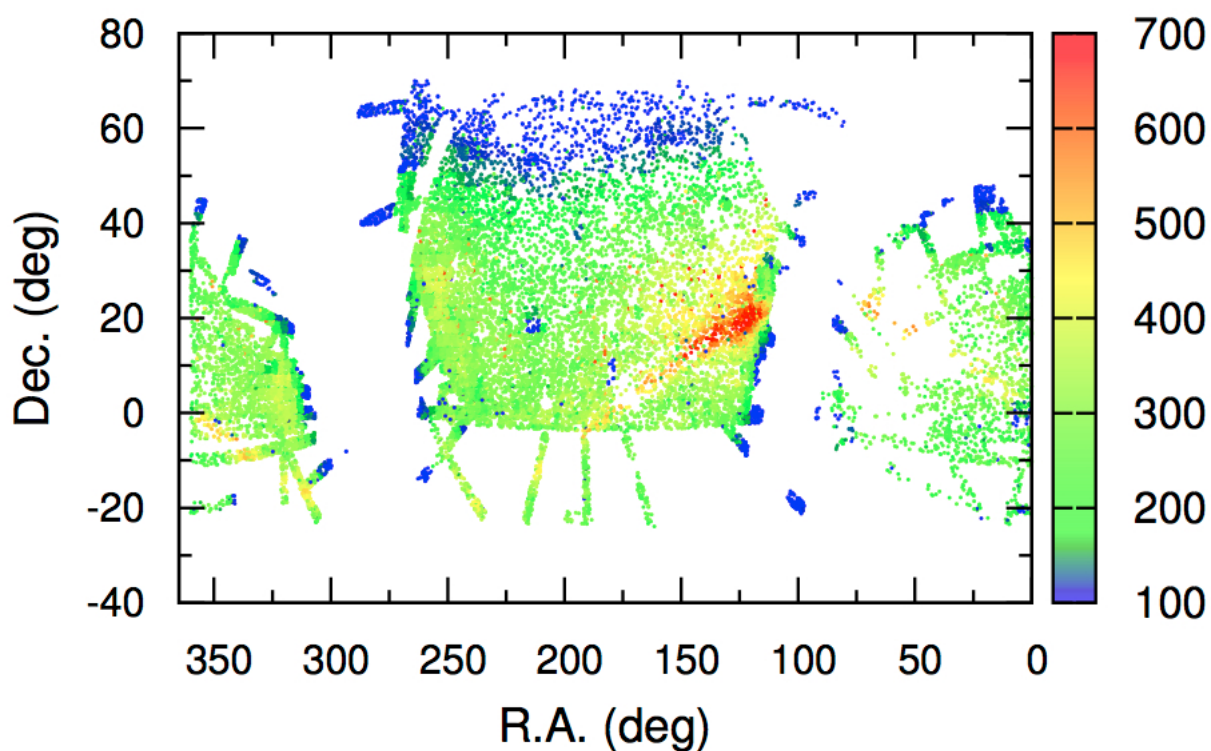


Figure 4.2: The number of CSDR2 observations per star as a function of equatorial J2000.0 right ascension and declination. These are only the stars that are in the footprint of the SDSS covering $\sim 14000 \text{ deg}^2$ of the sky. The values are color-coded according to the legend. The mean number of epochs of these stars in the CSDR2 database is 270. 90% of these stars were visited more than 100 times.

Using data from the CSDR2, we calculated variability statistics like the weighted standard deviation (W_σ), χ^2 , variability index (α), variance (Var), amplitude (Amp), and the skewness of the light curves (γ) for a better separation of variable and non-variable stars. We list the definitions of these quantities below.

$$W_{\langle m \rangle} = \frac{\sum_{i=1}^N \frac{x_i}{x_{ierr}^2}}{\sum_{i=1}^N \frac{1}{x_{ierr}^2}} \quad (4.1)$$

$$W_\sigma = \sqrt{\frac{\sum_{i=1}^N \frac{(x_i - W_{\langle m \rangle})^2}{x_{ierr}^2}}{\frac{N-1}{N} \sum_{i=1}^N \frac{1}{x_{ierr}^2}}} \quad (4.2)$$

$$\chi^2 = \frac{1}{N-1} \sum_{i=1}^N \frac{(x_i - \bar{x})^2}{x_{ierr}^2} \quad (4.3)$$

$$\alpha = \frac{\sum_{i=1}^N (x_i - \bar{x})^2 - x_{ierr}}{N-1} \quad (4.4)$$

$$\gamma = \frac{N}{(N-1)(N-2)} \frac{1}{\zeta^3} \sum_{i=1}^N (x_i - \bar{x})^3 \quad (4.5)$$

$$\zeta = \sqrt{\frac{1}{N-1} \sum_{i=1}^N (x_i - \bar{x})^2} \quad (4.6)$$

where x_i and x_{ierr} represent the CSDR2 single-epoch magnitude and the error corresponding to this magnitude, respectively. \bar{x} is the mean magnitude (Mag), and N is the number of the CSDR2 epochs for each star.

Our RRL candidates are the stars that passed our SDSS color cuts in Section 4.2.1, the PS1 variability cuts in Section 4.2.2, and that have W_σ , χ^2 , α , Var , and Amp greater than 0.1, 1.0, 0.002, 0.006, and 0.4, respectively, and $-1.0 < \gamma < 1.0$. These variability threshold limits were defined using the CSDR2 variability statistics of the QUEST RRL stars (Vivas & Zinn, 2006) discussed in Section 3.5. We did not define the CSDR2 variability statistics threshold limits using the catalog of RRL stars in Stripe 82 (Sesar et al., 2010) because we later use the latter catalog to test our efficiency and completeness levels.

Of the ~ 21050 stars with the CSDR2 information, 8351 stars ($\sim 40\%$) passed the CSDR2 additional variability cuts applied in this section. These stars are retained for further analyses.

4.3.1 The Analysis of Variance

We used the AoV (Schwarzenberg-Czerny, 1989) technique to find the periods of the 8351 RRL candidates. Using Fourier methods, the AoV technique calculates variances of the light curves using different periods and tries to detect sharp signals (Schwarzenberg-Czerny, 1989). Each calculated signal corresponding to a different trial period (in the 0.1–1.1 days range) is then represented in a periodogram (period vs. power). For each light curve, we chose the period with the highest signal. Having low signal reflects a non-periodic behavior for the phased light curve while a large signal reflects a good periodic behavior.

For instance, Figure 4.3a represents the light curve for one of our stars, with the modified Julian date (MJD) plotted along the x-axis and the magnitudes along the y-axis. The periodogram from the AoV technique and the best-phased light curve corresponding to a period of ~ 0.62154 d are represented in panels (b) and (c) of the same

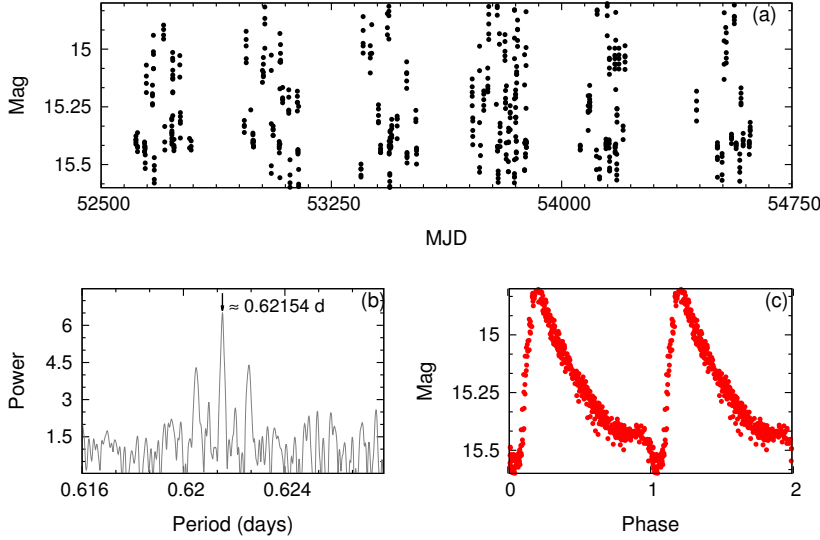


Figure 4.3: This figure illustrates how the AoV technique works. Panel (a): The light curve (MJD vs. Mag) of one of our stars. Panel (b): The periodogram from the AoV technique. The arrow marks a sharp signal detected by the AoV, indicating that the best period for this star is ~ 0.62154 d. Panel (c): Phasing the light curve with $P \sim 0.62154$ d shows an RRab-like light curve.

Figure. The arrow in Figure 4.3b marks the best period found by the AoV, indicating that the best period for this star is ~ 0.62154 d. The phased light curve in panel (c) shows a very well-fitted RRab-like light curve corresponding to the mentioned period.

4.3.2 Template Fitting Method

After estimating the best-fitted periods using the AoV technique, we used the Template Fitting Method (TFM; Layden 1998; Layden et al. 1999) in order to determine the types of our RRL candidates.

In total, the TFM uses a set of 10 different template light curves representing different variable stars. Six of these template light curves are for RRab stars, two for RRC stars, one for W UMa contact binary stars, and one for Algol eclipsing binary stars. We show these templates in Figure 4.4. The CSDR2 light curves are folded using periods from the AoV technique and are fitted by each of the 10 templates. The χ^2_{TFM} and rms scatter of each fit are then calculated. Small χ^2_{TFM} and rms values reflect a good template fit, which in turn reflects the correct type of the star.

In order to insure that this classification process was correct, we visually inspected the four best-fitted templates for each star. The four best-fitted templates for CSDR2 star-id 1157029004107 (period of 0.52853 days) are shown in panels (a), (b), (c), and (d) of Figure 4.5, respectively. The phased light curves and the best-fitted templates are shown in red and green, respectively.

All of the four best-fitted templates belong to RRab stars with rms ranging between 0.0479 and 0.0607 for the first and fourth best-fitted template, respectively. The asymmetric, steep rise, and slow decrease in brightness of the phased light curves and templates suggest that this is an RRab star with an amplitude of ~ 1.0 mag. This visual inspection was done for all of the RRL candidates.

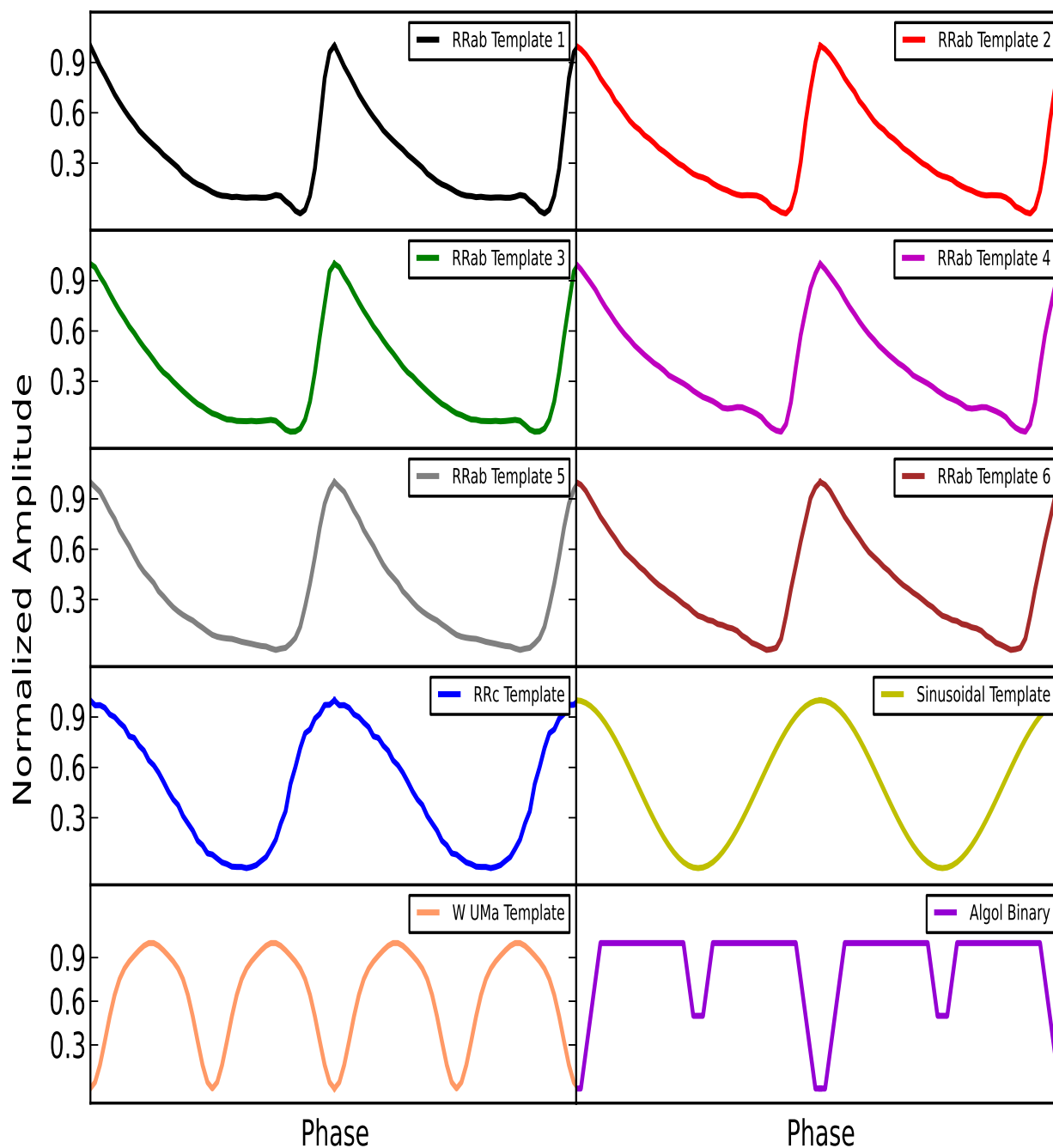


Figure 4.4: The 10 TFM templates used to classify our variable objects. All light curves are fitted by each of the 10 templates.

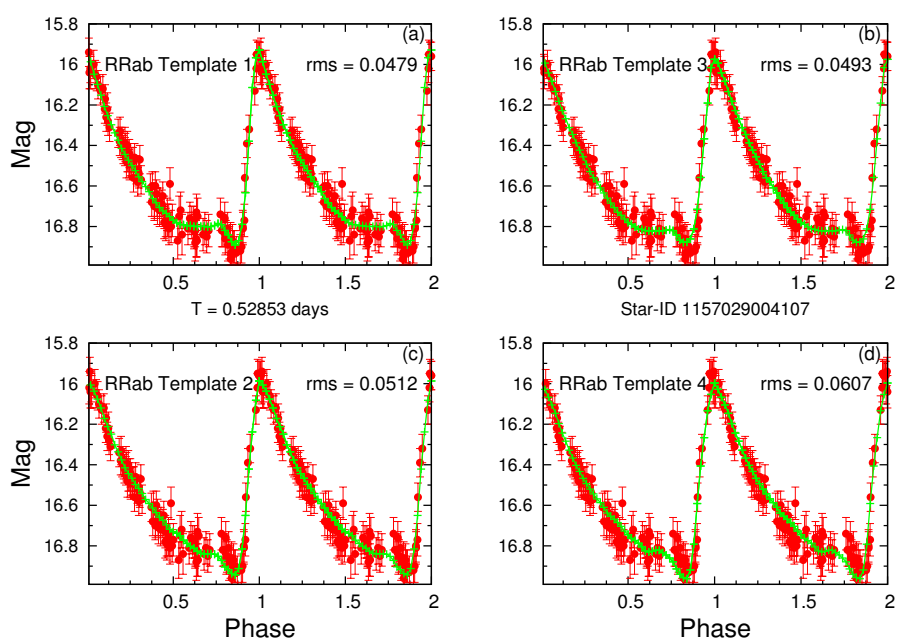


Figure 4.5: Panels (a), (b), (c), and (d) illustrate the four best-fitted templates by the TFM for CSDR2 star-id 1157029004107 (period of 0.52853 days). The phased light curves and the best-fitted templates are plotted in red and green, respectively. All of the four best-fitted templates belong to RRab stars with an *rms* ranging between 0.0479 and 0.0607.

4.4 Results

After applying the AoV and the TFM methods and after the visual inspection of the four best-fitted templates by the TFM, we were able to detect 4800 RRab stars and 1571 RRc stars (6371 RRL stars in total). These are the stars that passed the variability and color cuts and that were well fitted with the templates provided by the TFM. The positions (R.A. and Dec.), CSDR2 mean magnitudes (Mag), CSDR2 amplitudes, subtypes, periods, ephemeris (MJD_{max} ; time at maximum light), and d_h (see Section 4.8) of our RRab and RRc stars are found in Table 4.2.

Figure 2.1 and Figure 2.2 illustrate the phased light curves of one of our RRab and RRc stars, respectively. The asymmetrical shape, steep rise, and slow decrease of the RRab stars' phased light curves have been observed in all of our RRab stars. On the other hand, the more symmetrical phased light curves with relatively smaller amplitudes were observed in all of our RRc stars. The unique phased light curve shape of RRab stars makes it relatively easy to identify them with high efficiency, compared to RRc stars that have phased light curves that can be confused with other types of variable stars (i.e., W UMa, δ Scuti, and SX Phe stars, see Section 4.7.3).

The P–A diagram for the RRab (red dots) and RRc (blue dots) stars is shown in Figure 2.3. RRab stars tend to have higher amplitudes and periods than RRc stars, as expected. Figure 2.3 also shows that most of the RRab stars are concentrated in a narrow period-amplitude range (periods less than ~ 0.65 days), these stars belong to the Oosterhoff I group. Some RRab stars lie toward the longer period region and belong to the Oosterhoff II group. See Section 2.6 for more information about the Oosterhoff effect (Oosterhoff, 1939) and Chapter 6 where we use ~ 17000 CSS RRab stars to study this phenomenon.

4.5 Comparison with Stripe 82

It is important to check how complete, efficient, and reliable our catalog is. Accordingly, we compare our RRL star discoveries with the catalog of RRL stars in Stripe 82 (Sesar et al., 2010). We also discuss the properties of the RRL stars that we missed.

4.5.1 Completeness

Our catalog contains 184 RRL stars (137 RRab and 47 RRc stars) in the Stripe 82 area, out of which 177 (136 RRab and 41 RRc stars) are also found in the catalog of RRL stars in Stripe 82 (Sesar et al., 2010). The 7 extra RRL stars are found in our catalog only. The presence of the extra RRL stars can either prove that our catalog is slightly contaminated by non-RRL stars or that Sesar et al.'s (2010) catalog is not 100% complete.

Our achieved completeness level is distance-dependent because of the magnitude cut ($12.0 < u < 19.0$) applied and discussed in Section 4.2.1. All of the common 177 RRL stars in Stripe 82 that are found in our and in Sesar et al.'s (2010) catalog have d_h between ~ 4 and ~ 28 kpc. These distances are provided in the latter catalog. Accordingly, the completeness level will be studied and analyzed in the mentioned distance range. Sesar et al.'s (2010) catalog contains 337 RRL stars (255 and 82 of type ab and c, respectively) with d_h in the 4–28 kpc distance range. Since we recovered 136 and 41 RRab and RRc stars, respectively, our completeness level is then $\sim 50\%$ for RRab and RRc stars.

4.5.2 Missed RRL Stars

With our 50% completeness level computed in the previous section, we know that we missed $\sim 50\%$ of the RRL stars in Stripe 82 with d_h in the 4–28 kpc distance range. These missed stars either did not have CSDR2 information or did not pass the variability cuts in Section 4.2.2 ($\sigma_{g_{P1}} > 0.05$ or $\sigma_{r_{P1}} > 0.05$).

For example, only $\sim 60\%$ of the RRL candidates that passed the SDSS color and the PS1 variability cuts had CSDR2 data. The remaining missed stars were either not observed with the Catalina Survey, or they are located in crowded regions (i.e., de-blending problems) where they had a small number of clean CSDR2 detections.

Another reason for why we missed 50% of the RRL stars are the PS1 variability cuts applied in Section 4.2.2. Although most of the missed RRL stars were observed ~ 4 times in g_{P1} or r_{P1} , the variability of the missed RRL stars did not appear in the PS1 database. RRL stars are short period variable stars and are repeating their cycles between ~ 1 and ~ 5 times a day. Hence, it is likely that some RRL stars were repeatedly observed at the same or a close phase.

Table 4.2: Our catalog of RRL stars. Both equatorial J2000.0 R.A. and Dec. are given in decimal degrees. A portion of the table is shown here for guidance regarding its form and content. The complete table which contains 6371 RRL stars (4800 RRAb and 1571 RRc stars, respectively) is available in its entirety in the electronic version of the paper (Abbas et al. 2014a, <http://mnras.oxfordjournals.org/content/441/2/1230/suppl/DC1>).

SDSS NAME ^a	R.A.	Dec.	<i>Mag</i> ^b	<i>Amp</i> ^c	Type	Period ^d	MJD _{max} ^e	<i>d</i> _h ^f
SDSS J140016.30+155821.4	210.0679	15.9726	17.54	1.03	ab	0.4860	55676.21067	27.6
SDSS J170343.25+115155.5	255.9302	11.8654	15.61	1.43	ab	0.4695	54591.39047	11.7
SDSS J143301.30+181254.3	218.2554	18.2150	16.32	0.93	ab	0.4865	54228.29835	15.9
SDSS J103555.83+382214.0	158.9826	38.3705	16.25	1.15	ab	0.4875	54566.25784	14.8
SDSS J153604.59+210746.7	234.0191	21.1296	16.88	0.8	ab	0.6701	53866.34446	16.1
SDSS J134644.45+454526.2	206.6852	45.7572	15.76	1.2	ab	0.4738	54138.43831	11.8
SDSS J201518.96-124928.8	303.8290	-12.8246	16.61	0.75	ab	0.5559	54286.39649	15.5
SDSS J172732.63-133844.0	261.8859	-13.6455	15.20	0.91	ab	0.5558	53986.47201	5.3
SDSS J144412.93+203641.2	221.0538	20.6114	14.37	0.47	c	0.3479	54884.44511	7.4
SDSS J145428.85+501007.7	223.6202	50.1687	17.03	0.53	c	0.3662	56126.21641	21.2

^aThe official SDSS designation for an object where the coordinates are truncated, not rounded, given by the format: JHHMMSS.ss+DDMMSS.s

^bThe CSDR2 mean magnitude

^cThe CSDR2 amplitude range

^dPeriod in days

^eEphemeris of the stars (time at maximum light)

^fHeliocentric distances in kpc

Nevertheless, we were still able to recover more than 50% of the RRL stars with the small number of epochs available from the PS1 at the moment. The completeness level will be significantly higher when more PS1 epochs are available. Nevertheless, the variability cuts were necessary to distinguish a possible variable from a non-variable star.

4.5.3 Efficiency

Among the 184 RRL stars we found in Stripe 82, 137 and 47 are of type ab and c, respectively. Out of the 137 RRab stars, 136 are classified as RRab stars in Sesar et al.'s (2010) catalog.

Of our 47 RRc stars, 41 are found and classified as RRc stars in the latter catalog. Assuming that Sesar et al.'s (2010) catalog is complete, our efficiency levels are then $\sim 99\%$ and $\sim 87\%$ for RRab and RRc stars, respectively.

The phased light curves of the extra RRab star and 3 out of the 6 RRc stars are plotted in red in Figure 4.6. These are the RRL stars in Stripe 82 region that are found in our catalog but not in Sesar et al.'s (2010) catalog. The best-fitted templates from the TFM are shown in green for stars with the CSDR2 star-ids 1001118058621, 2101029003452, 1101120009185, and 1101010021310 in panels (a), (b), (c), and (d) of Figure 4.6, respectively. These stars passed the color and variability cuts that are well defined for RRL stars, have been well fitted with RRL star templates by the TFM, and were observed by the CSDR2 between ~ 250 and ~ 380 times. We believe that the phased light curve shown in Figure 4.6a belong to an RRab star that was missed by Sesar et al. (2010). However, we are less confident about the 6 extra RRc stars that we found in Stripe 82 as their light curves can be confused with other types of variable stars (see Section 4.7.3). In the worst-case scenario, if we assume that all of the 6 RRc stars are non-RRL stars, our efficiency level would be $\sim 87\%$.

4.5.4 Period Testing

Finally, $\sim 95\%$ of our periods differ on average by only 0.009% from the periods found by Sesar et al. (2010). The maximum percentage difference was $\sim 0.17\%$. Periods in Sesar et al.'s (2010) catalog were obtained using the Super-smoother routine (Reimann, 1994) which is a smoothing routine that fits data points as a function of phase to a range of frequencies. It uses a running mean or running linear regression on the data points. The small percentage difference between our and Sesar et al.'s (2010) periods demonstrates the reliability of our method.

4.6 Comparison With the Catalina and the LSQ QUEST catalog of RRL stars

4.6.1 The Catalina catalog of RRL stars

In total, there are ~ 14500 RRab stars found in both the first catalog of RRL stars in the CSDR1 database (Drake et al., 2013a), and in its re-analysis study (Drake et al., 2013b) (i.e., in the ‘‘CSS Search 1’’)

Of the ~ 14500 RRab stars found in the ‘‘CSS Search 1’’, ~ 7500 RRab stars are located in our d_h distance range (4–28 kpc) and area (SDSS \times PS1 \times CSDR2 footprint). We were able to recover $\sim 55\%$ (~ 4150 stars) of the 7500 RRab stars from them.

Missing the remaining $\sim 45\%$ RRab stars was expected as these stars did not show any sign of variability in the PS1 data due to the small number of detections in g_{P1} and r_{P1} that we discussed in Section 4.5.2. Comparing our periods with periods from the ‘‘CSS Search 1’’ for the 4150 common RRL stars made us trust our results as 99% of the matched periods had percentage difference less than 0.009%.

Panels (a) and (b) of Figure 4.7 show the phased light curves of CSDR2 star-id 1109090090390 and 1129076074116, respectively. The light curves phased to our periods (P1) and to Drake et al.'s (2013a) periods (P2) are shown in red and gray, respectively. Light curves phased in red are less scattered and look more like RRab stars than those plotted with gray implying that our periods are more accurate. We applied the TFM on the phased light curves twice (using P1 and P2). The *rms* values for the P1-phased light curves were smaller than those corresponding to P2-phased light curves, in both cases. Hence, we trust our claimed periods in the mis-matched cases.

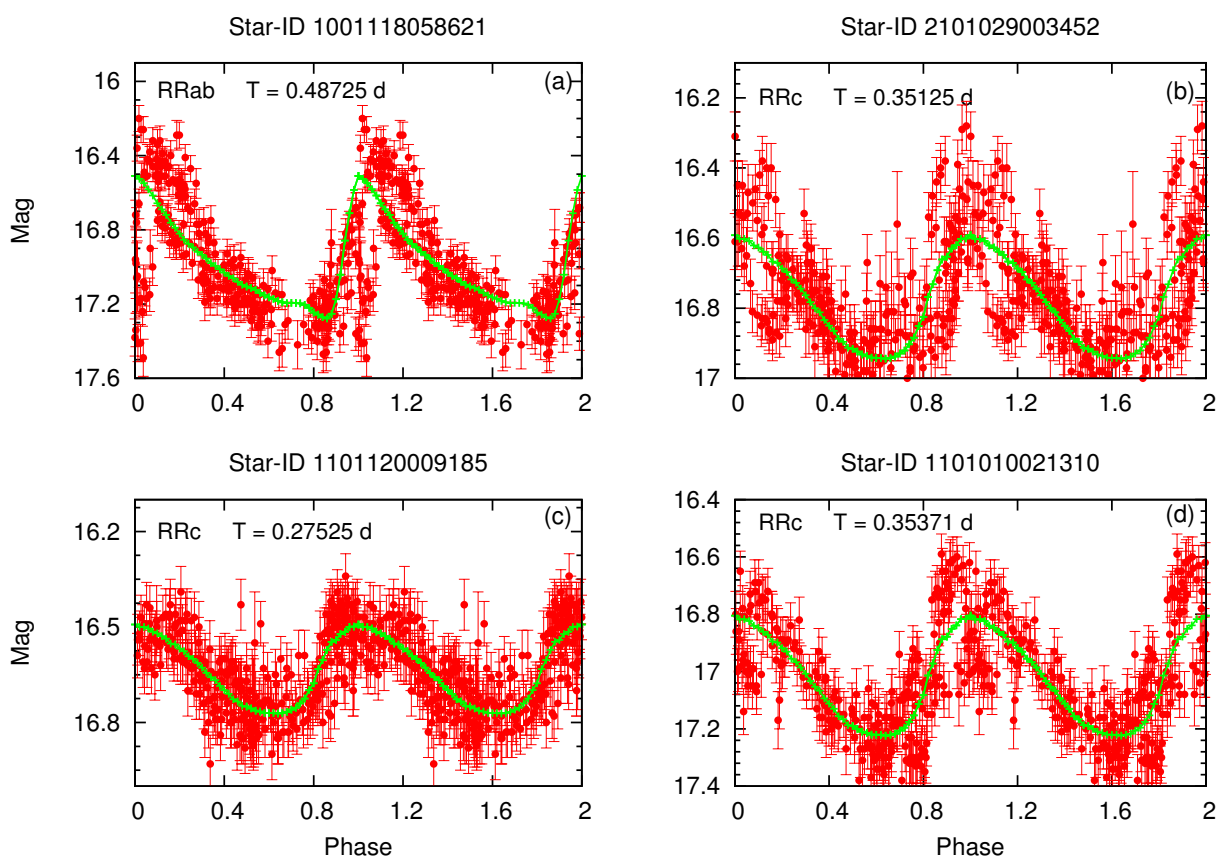


Figure 4.6: The phased light curves of the RRab star and 3 RRc stars that are found in our catalog but not in Sesar et al.'s (2010) Stripe 82 catalog. The phased light curves and the best-fitted templates from the TFM are plotted in red and green, respectively.

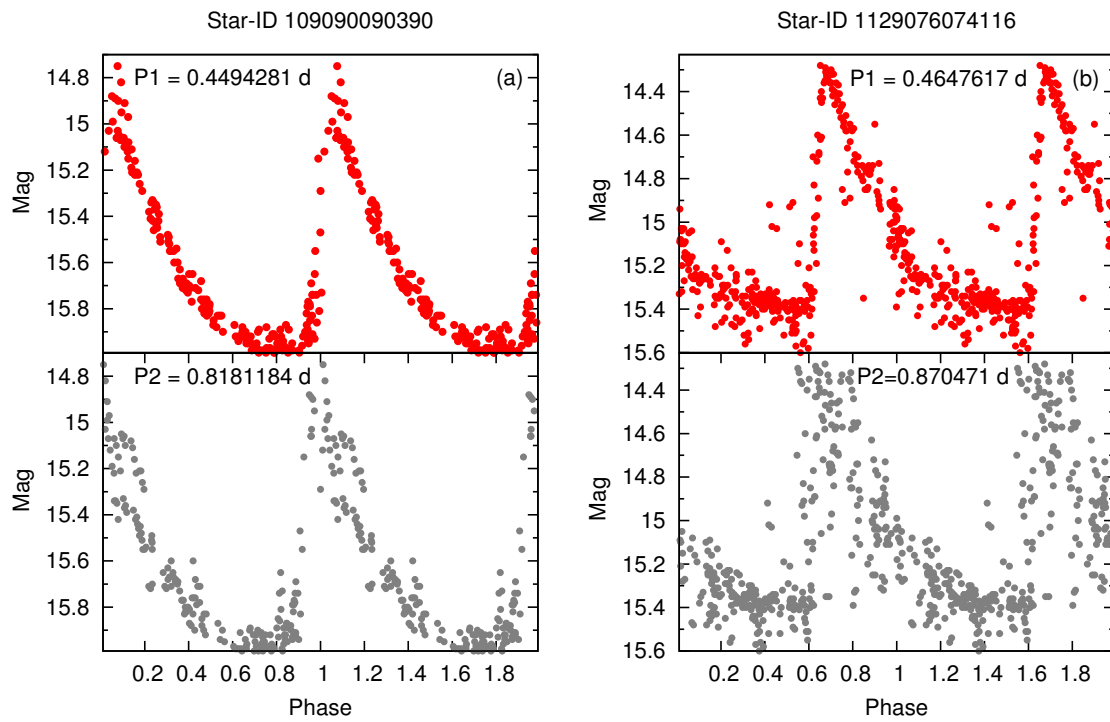


Figure 4.7: Panels (a) and (b) show the phased light curves of CSDR2 star-id 1109090090390 and 1129076074116, respectively. The light curves phased to our periods (P1) and to Drake et al.'s (2013a) periods (P2) are shown in red and gray, respectively.

4.6.2 The LSQ QUEST catalog of RRL stars

The LSQ catalog of RRL stars (Zinn et al., 2014) contains 1372 RRL stars (1013 RRab and 359 RRc) with $d_h < 80$ kpc. Around 70% of the RRab stars found in the LSQ catalog of RRL stars are also found in the “CSS Search 1” (Drake et al., 2013a,b) that we already compared to our catalog in the previous section. We recovered 355 out of the 1013 LSQ RRab stars of which 336 are also found in the CSDR catalog of RRL stars. Only 84 RRc stars are found in both our and LSQ catalog of RRL stars. Most of the remaining LSQ RRL stars that we missed are located beyond our covered distance range ($d_h > 28$ kpc).

Our catalog contains ~ 230 RRL stars that are not found in the LSQ catalog of RRL stars. Zinn et al. (2014) computed their completeness ($\sim 70\%$) level by comparing their catalog with the CSDR catalog of RRL stars (Drake et al., 2013a,b). We believe that their completeness level is slightly lower than 70% as we have shown in this study that the CSDR catalog of RRL stars is not complete. The additional visual inspection that we performed for the light curves of the ~ 230 RRL stars suggests that these are indeed RRL stars.

4.7 Newly Discovered RRL Stars

Although Drake et al. (2013a,b) searched for RRab stars in the whole CSDR database, we were still able to find 646 new RRab stars that were missed by them. Of these 646 RRab stars, 19 stars were found also in the LSQ catalog of RRL stars (but not in the “CSS Search 1”). Around 572 of our RRab stars are new discoveries. Additionally, we present the discovery of 1571 RRc stars of which ~ 1449 are new discoveries. Based on our analyses in Section 4.5, we estimate that only $\sim 2\%$ and $\sim 13\%$ of our RRab and RRc star discoveries are non-RRL stars. We discuss the nature of our contaminant stars in Section 4.7.3.

4.7.1 RRab Stars

We identified 627 additional RRab stars that are neither found in the “CSS Search 1” (Drake et al., 2013a,b) nor in the LSQ catalogs of RRL stars (Zinn et al., 2014). The phased light curves, TFM and AoV analyses, and variability statistics of these stars are similar to the other common RRL stars that we and Drake et al. (2013a,b) and Zinn et al. (2014) have found.

Out of the 627 newly discovered RRab stars, 55 are found in the GCVS (Samus et al., 2009). 42 out of the 55 RRL stars are classified as RRab stars in the GCVS, 12 as RRL stars without giving the sub-type and one as an RRc star.

Our period for the RRc star mentioned earlier (CSDR2 star-id 2122228003249) does not match the period found in the GCVS. The two phased light curves (in red) and the best-fitted templates by the TFM (in green) corresponding to our period ($P_1 = 0.54288$ days) and to the GCVS’s period ($P_{GCVS} = 0.34784$ d) are shown in panels (a) and (b) of Figure 4.8, respectively. The two cycles observed in one phase and the large scatter ($rms = 0.5451$) around the TFM template in Figure 4.8b suggest that this is not an RRc star, even if we assume that P_{GCVS} ’s period is correct. However, the RRab-like phased light curve and the small scatter ($rms = 0.1178$) around the best-fitted RRab template from the TFM in Figure 4.8a indicate that our classification and period are more accurate.

4.7.2 RRc Stars

Our catalog contains 1571 RRc stars, of which 84 are found in the LSQ catalog of RRL stars (Zinn et al., 2014). Additionally, only 38 of our RRc stars are found in the GCVS out of which 25 are classified as RRc stars, four as RRL stars without a sub-type, six as RRab stars, and three as stars in eclipsing binary systems (EW stars).

Four out of the six RRc stars that were classified as RRab stars have periods in the GCVS. The phased light curves corresponding to our (left part of each panel) and to the GCVS (right part of each panel) periods (P_{GCVS}) are shown in red and gray in Figure 4.9, respectively. The green fits indicate the best-fitted templates from the TFM, all corresponding to RRc stars. It is clear that folding the light curves to the P_{GCVS} periods (in gray) did not produce periodic signals in the panels (a), (b), and (c) of the latter figure. On the other hand, periodic signals (in red) and well fitted RRc templates (in green) were observed when folding the light curves to our periods, indicating that these are indeed RRc stars.

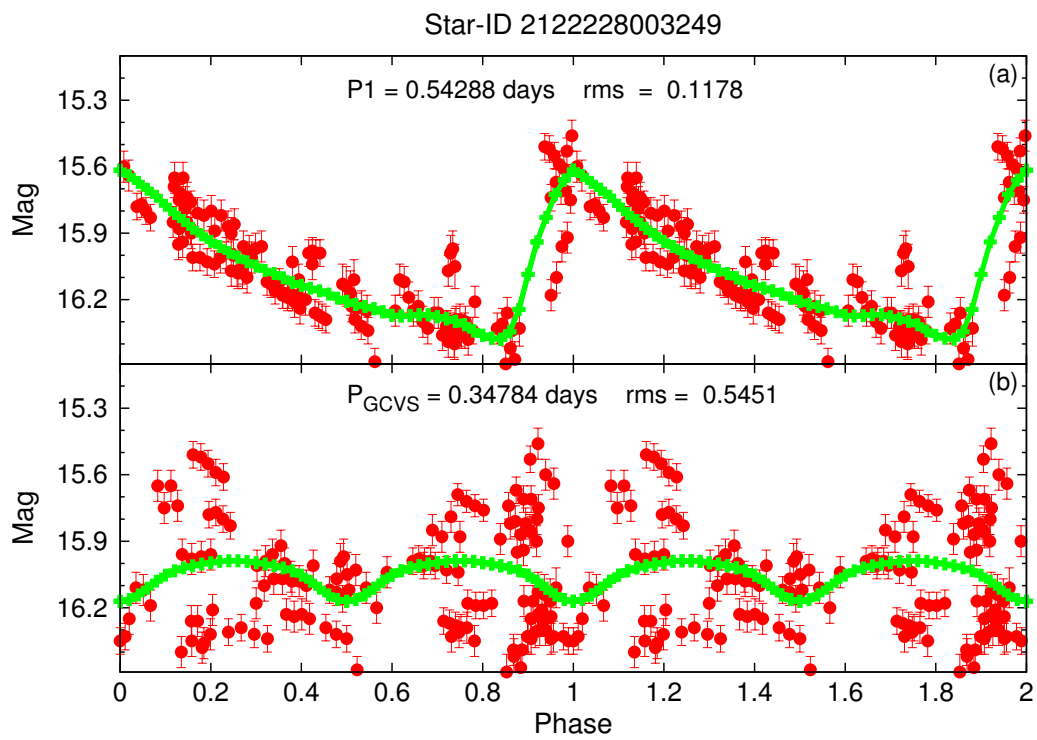


Figure 4.8: A comparison between the two phased light curves (in red) and the best-fitted templates by the TFM (in green) representing our ($P_1 = 0.54288$ days) and the GCVS ($P_{GCVS} = 0.34784$ d) periods are represented in panels (a) and (b) for CSDR2 star-id 2122228003249.

Although periodic signals are observed when folding the data to our and to the P_{GCVS} period in Figure 4.9d, we believe that our period and classification are more accurate because the AoV and TFM analyses are based on 274 CSDR2 epochs for this star.

4.7.3 Contaminant Stars

It is not surprising that some of our RRc stars are contaminated by other type of stars (i.e., W UMa stars, δ Scuti, etc.) as these stars have moderately symmetric light curves (i.e., sinusoidal) and share the same period range. However, we used color cuts that are well characterized for RRL stars. Additionally, each light curve was fitted to both RRc and W UMa templates by the TFM. The fits worked better for the RRc templates for all of our RRc stars.

After comparing our RRc star discoveries with the GCVS in the previous section, and with Stripe 82 in Section 4.5.3, we believe that the RRc contamination level by eclipsing binaries is less than $\sim 15\%$, and is caused mainly due to W UMa stars.

Finally, δ Scuti and SX Phe stars that are usually found in the disk and field as well as in globular and open clusters, have colors similar to the colors of RRL stars (Palaversa et al., 2013) and have periods less than ~ 0.3 days². Because almost half of our RRc stars have periods less than 0.3 days, \sim half of our RRc stars are prone to contamination from δ Scuti and SX Phe stars.

4.8 Distances Of RRL Stars and Halo SubStructure

In this section, we check whether the completeness and efficiency levels of our catalog are good enough to detect previously known and possibly new halo overdensities. First, we derive the d_h of the RRL stars in our catalog using Equation 4.7:

$$d_h = 10^{(\langle V_0 \rangle - M_v + 5)/5} \quad (4.7)$$

where $\langle V_0 \rangle$ magnitudes are calculated using Equation 4.8 which was adopted from Ivezić et al. (2005).

$$\langle V_0 \rangle = r - 2.06(g - r) + 0.355 \quad (4.8)$$

where the g and r SDSS magnitudes were corrected for the line-of-sight interstellar extinction using the recalibration of Schlegel et al.'s (1998) dust map by Schlafly & Finkbeiner (2011). This equation corrects a bias in single-epoch SDSS measurements due to the unknown phase and introduces a minimal rms scatter of 0.12 mag.

Like Sesar et al. (2010), we adopt $\langle M_V \rangle = 0.60$ mag for the absolute magnitude of RRL stars; a value that was calculated by (Cacciari & Clementini, 2003) using Equation 4.9.

$$M_V = (0.23 \pm 0.04)[\text{Fe}/\text{H}] + (0.93 \pm 0.12) \quad (4.9)$$

where the mean halo metallicity of $[\text{Fe}/\text{H}] = -1.5 \pm 0.32$ dex is used (Ivezić et al., 2008). Adopting $[\text{Fe}/\text{H}] = -1.5$ dex introduces rms_{M_v} of ~ 0.1 mag because of the actual dispersion of $[\text{Fe}/\text{H}]$ and their corresponding uncertainties. Taking the uncertainties of $[\text{Fe}/\text{H}]$, $\langle V_0 \rangle$, and M_v into account, d_h is calculated with at least $\sim 7\%$ fractional error.

To test if our completeness and efficiency levels are good enough to detect substructures (and to possibly find new ones), we plotted the number density distribution of the 184 RRL stars we found in Stripe 82 in Figure 4.10. Assuming that Sesar et al.'s (2010) catalog is 100% efficient and complete implies that the contamination level of our 184 RRL stars is $\sim 4\%$. The density of the points that is accentuated by the white contours is shown in scaled density levels. The smoothed surface regions with high and low numbers of stars are represented in red and dark blue, respectively.

The HAC (Belokurov et al., 2007) halo substructure appears at R.A.³ $\sim -40^\circ$ and spans d_h in the 8 to 24 kpc distance range while the arm of Sgr dSph tidal stream (Majewski et al., 2003) appears at R.A. $\sim 30^\circ$ and $d_h \sim 23$ kpc.

²<http://www.aavso.org/types-variables>

³Add 360° to obtain the correct values of R.A. when R.A. $< 0^\circ$. Negative values of R.A. were used for better visualization only.

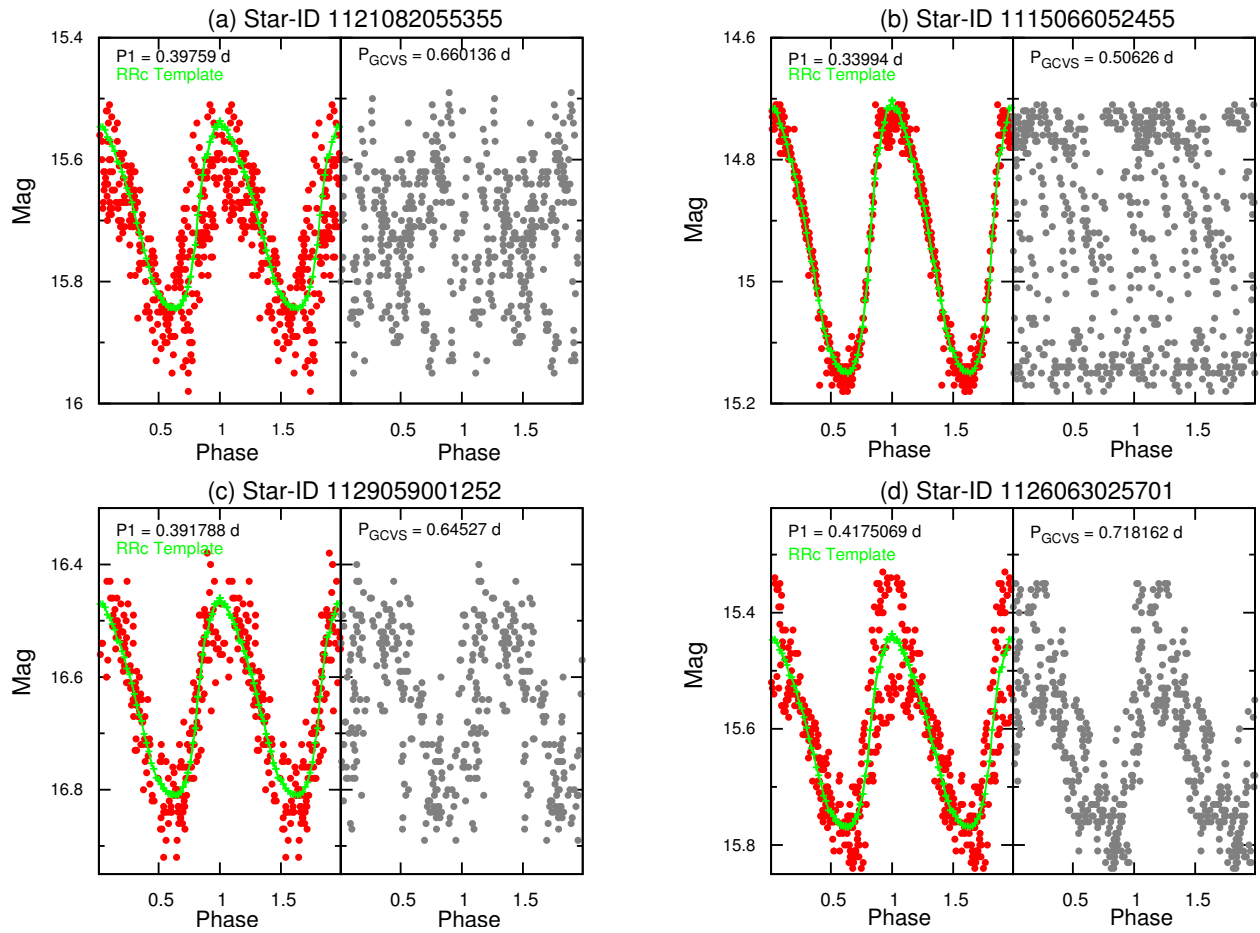


Figure 4.9: The phased light curves corresponding to our (left part of each panel) and to the GCVS (right part of each panel) periods are shown in red and gray, respectively. The green fits indicate the best-fitted templates from the TFM, all corresponding to RRc stars.

Our RRL stars that are found in the Northern Galactic hemisphere section of the celestial equator ($-1.25^\circ < \text{Dec.} < 1.25^\circ$) are plotted in Figure 4.11. The Virgo overdensity (Vivas et al., 2004; Jurić et al., 2008) was detected at R.A. $\sim 190^\circ$ and $d_h \sim 19$ kpc while the HAC at R.A. $\sim 240^\circ$ and $d_h \sim 10$ kpc.

Some parts of the well-defined narrow tidal tails of the extended, low-concentration globular cluster Pal 5 (Odenkirchen et al., 2001, 2003; Grillmair & Dionatos, 2006) overlap in projection with the clump appearing at R.A. $\sim 235^\circ$ and $d_h \sim 20$ kpc (see Figure 4.11). Pal 5 is a faint halo cluster that is currently undergoing tidal disruption due to disc shocks (Dehnen et al., 2004). This globular cluster has a very sparsely populated red giant branch and horizontal branch (Odenkirchen et al., 2003), with only very few RRL stars (five, see Vivas & Zinn 2006). Two additional RRL stars have been suggested to be associated with Pal 5's tidal tails (Vivas & Zinn, 2006). Although the clump appearing at R.A. $\sim 235^\circ$ and $d_h \sim 20$ kpc can indeed be associated with Pal 5, we do not confirm this association because of the small number of RRL stars (5–7) associated with Pal 5 in addition to possible stars that are contaminating our catalog. We suggest radial velocity studies of our RRL stars that belong to this clump in order confirm the association of this clump to Pal 5.

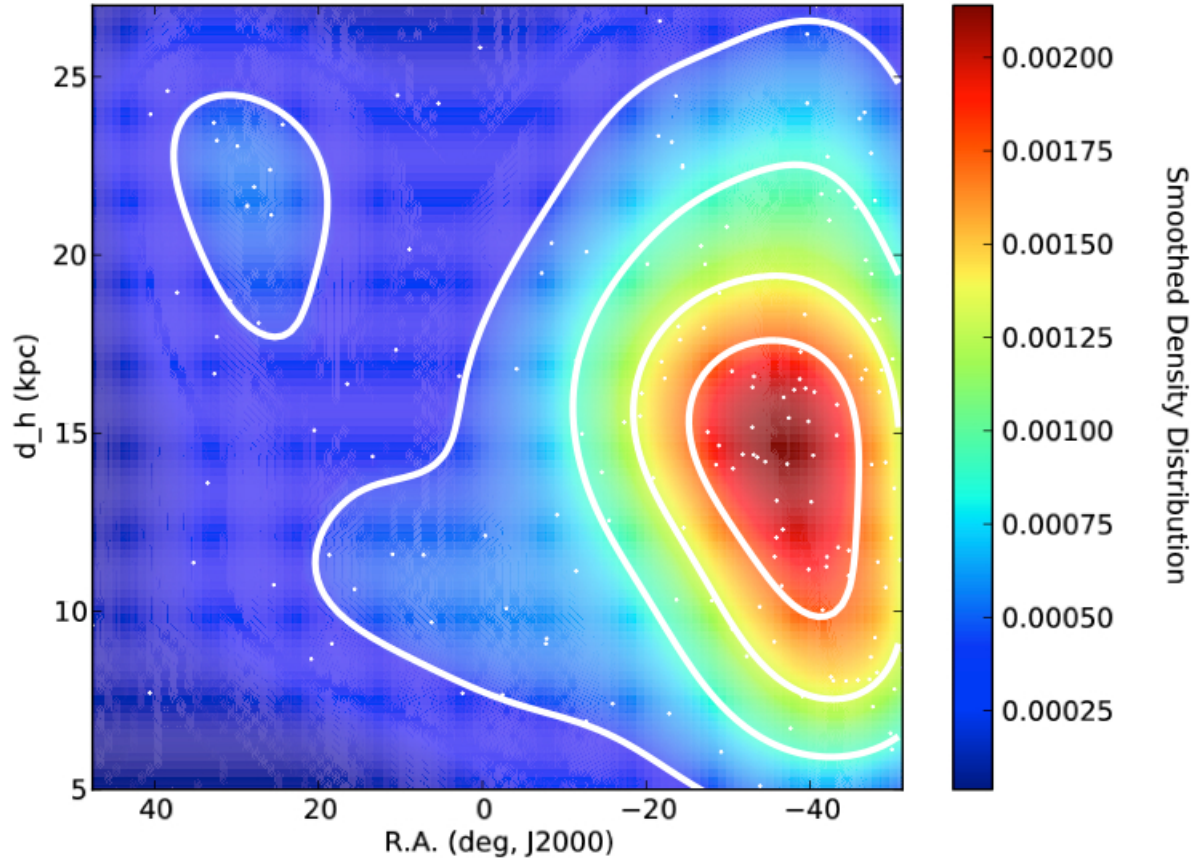


Figure 4.10: The number density distribution of the 184 RRL stars found in our catalog in the Stripe 82 area. The density of the points that is accentuated by the white contours is shown in scaled density levels. The smoothed surface regions with high and low numbers of stars are represented in red and dark blue, respectively. The HAC halo structure appears at R.A. $\sim -40^\circ$ and d_h in the 8 kpc to 24 kpc distance range while the arm of the Sgr dSph tidal stream appears at R.A. $\sim 30^\circ$ and $d_h \sim 23$ kpc. Negative values of R.A. were used for better visualization only (R.A. = R.A. + 360° when R.A. $< 0^\circ$).

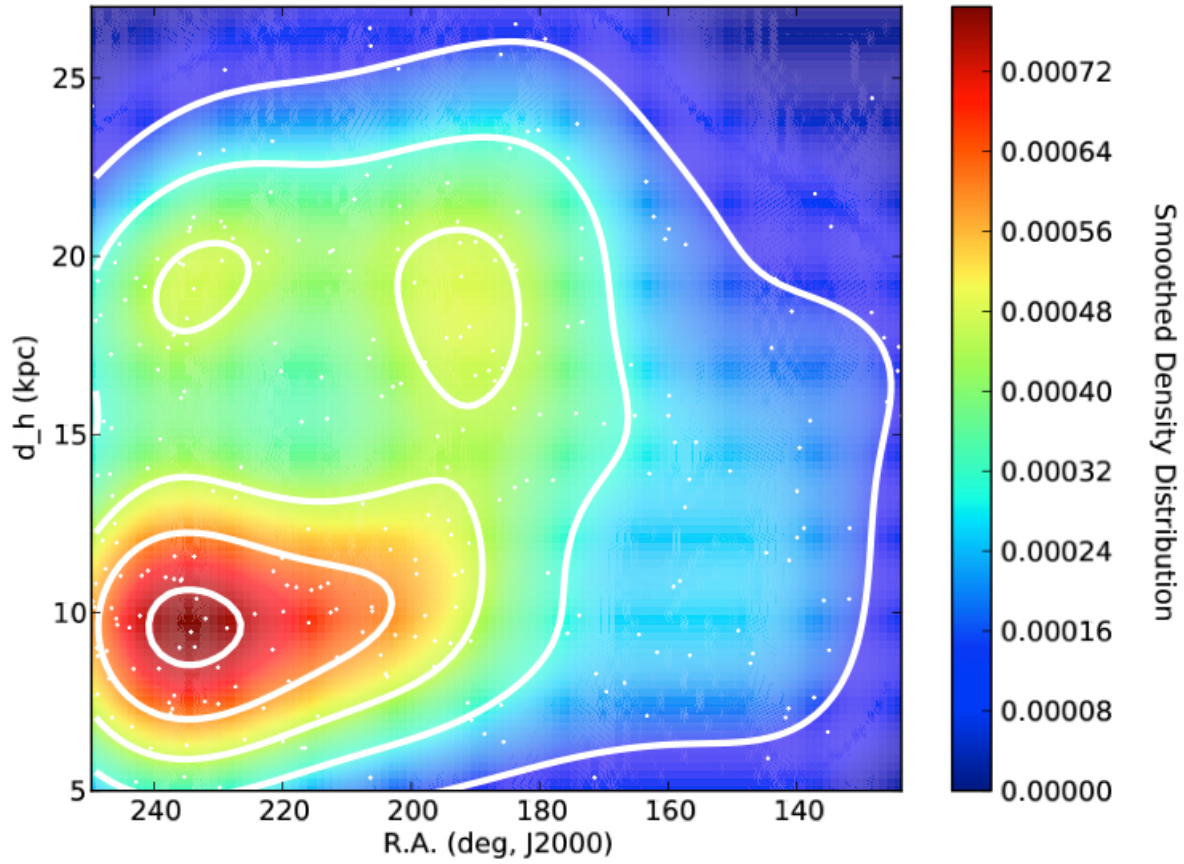


Figure 4.11: The number density distribution of the RRL stars found in the Northern Galactic hemisphere section of the celestial equator ($-1.25^\circ < \text{Dec.} < 1.25^\circ$). Two main structures are detected: the Virgo overdensity at R.A. $\sim 190^\circ$ and $d_h \sim 19$ kpc, the HAC at R.A. $\sim 240^\circ$ and $d_h \sim 10$ kpc.

4.9 Summary

We have combined data from different sky surveys (the SDSS, the PS1, and the Catalina Survey) to look for RRL stars in the Milky Way's halo. The search resulted in the discovery of 6371 RRL stars (4800 RRab and 1571 RRC) distributed around 14000 deg^2 of the sky and with d_h in the 4–28 kpc distance range. Around 2021 (~ 572 RRab and 1449 RRC) of these stars are new discoveries.

In this work, RRL stars were discovered using the SDSS color and the PS1 variability cuts in Section 4.2. We define the threshold limits of these cuts using the QUEST catalog of RRL stars (Vivas & Zinn, 2006) rather than using the catalog of RRL stars in Stripe 82 (Sesar et al., 2010) as we use the latter catalog to test the efficiency and completeness levels of our method.

Additional variability cuts were applied and light curves were plotted using the CSDR2 multi-epoch data. Periods were obtained using the AoV technique while the classification process was done by the TFM and by visual inspection. The comparison of our RRL star discoveries with the RRL stars in Stripe 82 from the SDSS shows that our completeness levels are $\sim 50\%$ for RRab and RRC stars and that our efficiency levels are $\sim 99\%$ and $\sim 87\%$ for RRab and RRC stars, respectively.

Additional comparison of our RRL star discoveries with the GCVS, the LSQ catalog of RRL stars, and the 14500 RRab stars found previously in the Catalina Survey (Drake et al., 2009, 2013b) suggests the reliability of our method. Additionally, the Virgo overdensity, HAC, and Sgr stream were recovered after plotting the number density distribution of our RRL stars in the Stripe 82 and Northern Galactic hemisphere areas. This indicates that our method is capable of identifying halo overdensities. Recently, Kinman & Brown (2014) used our catalog (Abbas et al., 2014a) as a comparison catalog and found similar results (~ 0.4 RRL stars per square degrees of the sky).

An optimized Method to Identify RRL stars

Do not forget God, struggle in His cause with your tongue, with your wealth, and with your lives. Imam Ali

Abstract We present a method for selecting RRL stars (or other type of variable stars) in the absence of a large number of multi-epoch data and light curve analyses. Our method uses color and variability selection cuts that are defined by applying a Gaussian Mixture Bayesian Generative Method (GMM) on 636 pre-identified RRL stars instead of applying the commonly used rectangular cuts. Specifically, our method selects 8115 RRL candidates ($d_h < 70$ kpc) using GMM color cuts from the SDSS and GMM variability cuts from the PS1. Comparing our method with the Stripe 82 catalog of RRL stars shows that the efficiency and completeness levels of our method are $\sim 77\%$ and $\sim 52\%$, respectively. Most contaminants are either non-variable main-sequence stars or stars in eclipsing systems. The method described here efficiently recovers known stellar halo substructures. It is expected that the current completeness and efficiency levels will further improve with the additional PS1 epochs (~ 3 epochs per filter) that will be observed before the conclusion of the survey. A comparison between our efficiency and completeness levels using the GMM method to the efficiency and completeness levels using rectangular cuts that are commonly used yielded a significant increase in the efficiency level from $\sim 13\%$ to $\sim 77\%$ and an insignificant change in the completeness levels. Hence, we favor using the GMM technique in future studies. Although we develop it over the SDSS \times PS1 footprint, the technique presented here would work well on any multi-band, multi-epoch survey for which the number of epochs is limited.

This chapter is based on our published work: Abbas, M., Grebel, E., Martin, N., Kaiser, N., Burgett, W., Huber, M., and Waters, C. (2014b, AJ, 148, 8)

Available from: <http://iopscience.iop.org/1538-3881/148/1/8/article>

5.1 Introduction

In Chapter 4 (Abbas et al., 2014a), the large number of repeated observations available allowed us to do accurate variability statistics and light curve analyses. This resulted in the detection of ~ 6371 RRL stars with very high efficiency levels ($\sim 99\%$ and $\sim 87\%$ for RRab and RRc stars, respectively). When light curve analyses are available, the techniques used in Chapter 4 can be adopted to detect RRL stars.

However, light curve analysis is not always possible as not all surveys provide enough multi-epoch data. The technique developed and used in the current chapter can be adopted in such surveys with few repeated epochs. In the current chapter, we look for RRL candidates by cross-matching the SDSS data with data from PS1. We show that using a Gaussian Mixture Bayesian Generative Method (GMM, VanderPlas et al. 2012) to set selection boundary cuts on the SDSS colors and PS1 variability allows one to find RRL stars (or other types of variable stars) even when only a small number of repeated observations are available and light curve analysis is not possible. Our method's efficiency and completeness levels also allow us to detect halo stellar streams and substructures.

In Section 5.2, we study the properties of RRL stars in the SDSS and PS1 photometric systems using more than 600 pre-identified RRL stars. In Section 5.3, we describe our method for selecting RRL candidates using the GMM selection boundary cuts for the SDSS colors and the PS1 variability. In the same section, we compute the efficiency and completeness levels of our method by comparing our results with the catalog of RRL stars from Sesar et al. 2010. Additionally, we compare the efficiency and completeness levels of our GMM method to the efficiency and completeness levels obtained using the rectangular cuts technique. In the same section, we study the properties of the contaminant stars. In Section 5.4, we apply our color and variability cuts to the whole overlapping footprint between the SDSS and PS1 to find the RRL candidates. In Section 5.5, we derive the distances for our RRL candidates and we use these distances to recover two known halo substructures. The content of the chapter is summarized and discussed in Section 5.6.

5.2 RRL Stars

RRL stars are best identified using color cuts, variability cuts, and light curve analysis. Although the colors of RRL stars in the SDSS photometric system have been studied and identified, the lack of variability information and light curve analysis poses difficulties in identifying these stars using the SDSS data alone. The SDSS data are based on single epoch observations with the exception of the overlapping regions and Stripe 82 (Sesar et al., 2010). The PS1 is a multi-epoch survey that can be used to study the variability of stars but finding RRL stars using the PS1 data alone is a challenge since the number of repeat observations used in PS1 is small (at most 10 epochs per filter) and the cadence is somewhat irregular.

Most of the previous studies that looked for RRL stars used a large number of multi-epoch data for each star which allowed them to analyze their light curves (see Chapter 3). We on the other hand are using the small number of PS1 repeated observations, which makes finding these stars a challenge. Nonetheless, we will demonstrate that using GMM (VanderPlas et al., 2012) to set selection boundary cuts on the SDSS colors and PS1 variability allows us to find RRL stars to detect halo stellar streams and substructures.

5.2.1 The Colors of RRL Stars in the SDSS and PS1 Photometric Systems

In Figure 3.1, we showed that the g , r , i , and z bands from the SDSS are similar to the g_{P1} , r_{P1} , i_{P1} , and z_{P1} bands from the PS1, respectively. However, the u band is used only in the SDSS but not in the PS1, and the y_{P1} band is found only in the PS1 but not in the SDSS. This is due to the difference in the surveys' major scientific goals and in the different sensitivities in the used cameras. The lack of the u filter in the PS1 is a disadvantage when it comes to finding RRL stars.

Additionally, the SDSS operates in a drift-scanning mode where the sky objects pass through its 5 different filters almost simultaneously. The correct colors of the observed sky objects can then be obtained unless they are variable on very short time scales (i.e., few minutes). Consequently, the SDSS drift-scanning technique gives the correct colors of RRL stars as these stars have periods in the ~ 0.2 –1 days range.

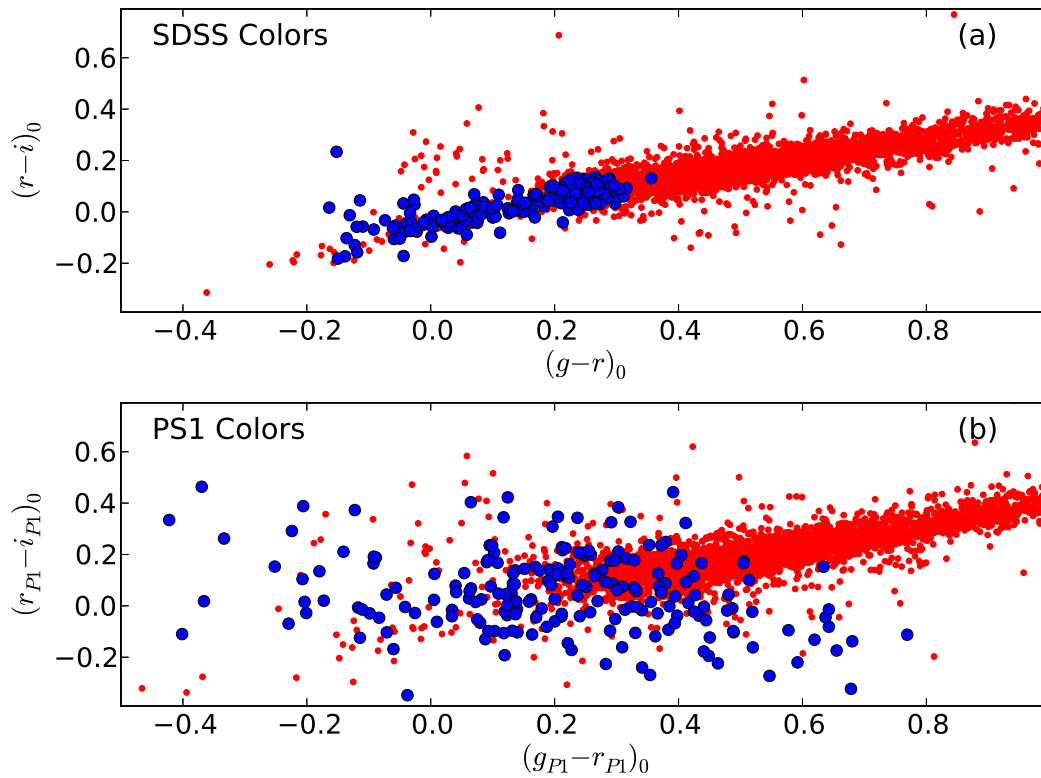


Figure 5.1: Illustration of the difference of the colors of RRL stars in the SDSS and PS1 photometric systems. Red dots show a subsample of non-RRL stars in Stripe 82 while blue filled circles show a subsample of the RRL stars detected in the same Stripe (Sesar et al., 2010). The scatter of RRL stars in the PS1 plot is due to non-simultaneous g_{P1} and r_{P1} observations by PS1 while the well-defined color region occupied by the RRL stars in the SDSS plot is due to the near-simultaneous imaging observations by the SDSS.

However, the correct colors of RRL stars are not provided with the PS1 photometric system because of the PS1 imaging technique. The PS1 images a selected patch of the sky with different filters at different times. Magnitudes in different filters correspond to different phases for short period variable objects like RRL stars.

Figure 5.1a illustrates the $(g-r)$ vs. $(r-i)$ color-color diagram of stars in Stripe 82 from the seventh data release of the SDSS (SDSS DR7), and Figure 5.1b illustrates the PS1 $(g_{P1} - r_{P1})$ vs. $(r_{P1} - i_{P1})$ color-color diagram for the same stars. Red dots represent a subsample of non-RRL stars while blue filled circles represent a subsample of the RRL stars detected in Stripe 82 (Sesar et al., 2010). While the RRL stars occupy a small and well-defined region in the SDSS color-color diagram (see Figure 5.1a), they are spread out over a large and wide region in the PS1 color-color diagram (see Figure 5.1b). This is a result of the different observing techniques used by the SDSS (near-simultaneous imaging using different filters) and PS1 (non-simultaneous imaging).

We base our color cuts for selecting RRL candidates on colors from the SDSS DR7 photometric system and not on the colors from the PS1 photometric system due to the lack of the u band and of the true colors of RRL stars in the latter photometric system.

5.2.2 Pre-identified Sample of RRL stars

We use 636 pre-identified RRL stars selected from the catalogs of RRL stars in the CSS (Drake et al., 2013a) and LINEAR (Sesar et al., 2013) surveys for a better characterization of the SDSS colors and PS1 variability properties of RRL stars.

These 636 RRL stars are chosen based on their clean photometry in the SDSS DR7 and PS1 photometric systems. These stars have photometric errors of less than 0.2 in u and less than 0.1 in g , r , i , z , g_{P1} , and r_{P1} . These are primary objects that are not blended or saturated in both surveys and that have been observed more than twice by PS1 in both g_{P1} ($N_{g_{P1}} \geq 3$) and r_{P1} ($N_{r_{P1}} \geq 3$), respectively. $N_{g_{P1}}$ and $N_{r_{P1}}$ represent the number of PS1 observations in the g_{P1} and r_{P1} filters, respectively. The two last cuts were applied in order to study the variability of RRL stars in the PS1 multi-epoch data.

We corrected the magnitudes for extinction using the recalibration of Schlegel et al.'s (1998) dust map by Schlafly & Finkbeiner (2011). Since the RRL stars used here are located in areas where the extinction is small (i.e., at high Galactic latitudes), such color corrections can be used. The color densities of the 636 RRL stars in the SDSS photometric system are shown in Figure 5.2 where red and blue regions reflect large and small numbers of RRL stars, respectively. A sample of non-RRL stars are also plotted as small white dots to demonstrate the colors of these contaminant stars (i.e., main-sequence stars and stars in eclipsing systems). RRL stars occupy small areas in the color-color diagrams in Figure 5.2 and are concentrated in well-defined regions, especially in the $(u-g)$ color, an advantage that helps in finding these stars.

5.3 Applying and Testing our Method

It is important to test and maximize the completeness and efficiency levels of our method in selecting RRL stars before we apply our color and variability cuts to the whole area where the SDSS and PS1 data overlap.

For that reason, we define and apply our GMM color and variability boundary cuts to the stars found in Stripe 82. We then compare the Stripe 82 catalog of RRL stars, which has efficiency and completeness levels of $\gtrsim 99\%$ (Sesar et al., 2010) to the RRL stars that our method detects in the same region. RRL stars in Sesar et al.'s (2010) catalog span d_h between ~ 4 and ~ 120 kpc and g magnitudes between ~ 12.8 and ~ 21.1 mag. There are 374 RRL stars in Sesar et al.'s (2010) catalog that are found in the overlapping area covered by PS1 and that are within our magnitude range ($14.0 < g_{P1} < 20.0$).

We base our comparison on these 374 RRL stars that are $\gtrsim 99\%$ efficient and complete in our magnitude range and sky coverage. We apply all our cuts and selection criteria step by step to stars found in Stripe 82. We then compute the efficiency and completeness levels for each step.

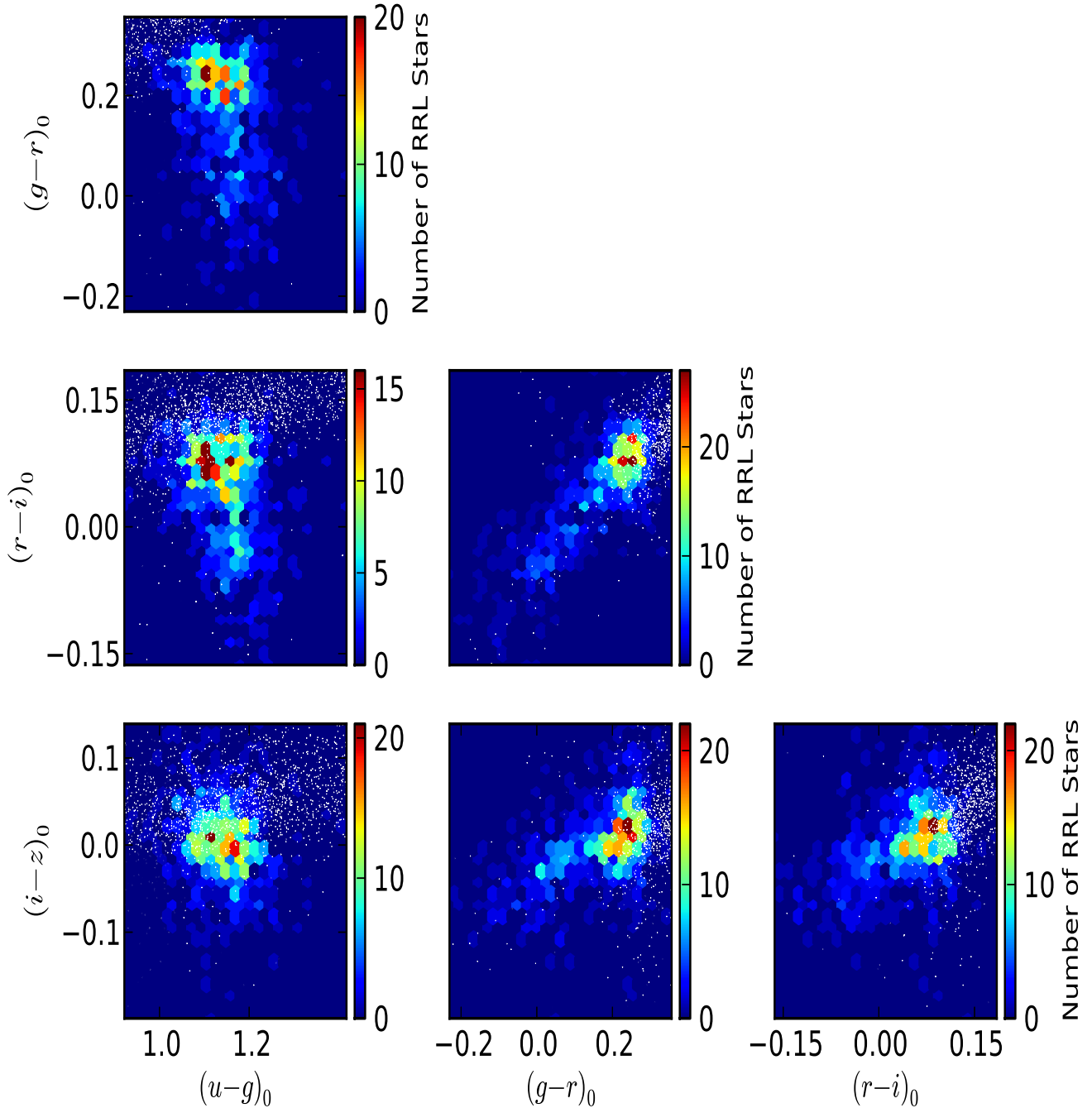


Figure 5.2: Different color-color diagrams of the 636 RRL stars in the SDSS photometric system where the red and blue regions reflect large and small numbers of RRL stars, respectively, as indicated by the color bars to the right of each panel. A sample of non-RRL stars are indicated as small white dots to demonstrate the colors of these contaminant stars. These colors are corrected for extinction using the recalibration of Schlegel et al.'s (1998) dust map by Schlafly & Finkbeiner (2011). RRL stars occupy small and well-defined regions in these plots.

5.3.1 Stripe 82

- **Step (1):** We start by adopting initial rectangular color cuts from Sesar et al. (2010) to avoid downloading all the SDSS DR7 data in Stripe 82 (and later for the whole SDSS×PS1 footprint). Our RRL candidates must first pass the first four initial rectangular color cuts :

$$0.75 < (u - g) < 1.45 \quad (5.1)$$

$$- 0.25 < (g - r) < 0.40 \quad (5.2)$$

$$- 0.20 < (r - i) < 0.20 \quad (5.3)$$

$$- 0.30 < (i - z) < 0.30 \quad (5.4)$$

These are single-epoch color ranges (Sesar et al., 2010) for RRab and RRc stars corrected for extinction using the Schlegel et al. (1998) dust map. The SDSS colors for RRL stars correspond to a random instant in their phase and depend on the time when the near-simultaneous SDSS photometry was obtained. It is thus safe to apply these color criteria to SDSS data but they are not suitable for PS1 data where the color range needs to be larger in order to account for the non-simultaneous observations in the PS1 filters. In order to avoid galaxies, these objects must be flagged as stars (`typeSDSS = 6`) in the SDSS. They should also be flagged as primary objects (`modeSDSS = 1`) with clean photometry in the SDSS DR7 database (`cleanSDSS = 1`).

Due to the noise and photometric errors resulting from the small number of PS1 epochs that we use in our method, some non-variable sources might appear as variables, especially faint sources with large photometric errors and bright sources that might saturate the CCD camera (see Section 5.3.3). To avoid this, we choose sources that are fainter than 14th and brighter than 20th magnitude in the PS1 g_{P1} filter (Equation (5.5)). Although PS1 will eventually observe each object around 12 times in each filter, the survey is not finished yet and the average number of detections per star is ~ 8 epochs in each of the PS1 filters. Some of these detections were not taken under good photometric conditions and therefore were flagged as bad sources by the PS1 pipeline. To ensure the reliability of our variability cuts, only clean PS1 detections that are not saturated or blended, and are not flagged as cosmic rays are used in our study (Morganson et al., 2012).

Thus, we only choose stars that have more than two clean detections in both the g_{P1} and r_{P1} filters (Equations (5.6)–(5.7)) in order to reliably distinguish variable from non-variable stars:

$$14.0 < g_{P1} < 20.0 \quad (5.5)$$

$$N_{g_{P1}} \geq 3 \quad (5.6)$$

$$N_{r_{P1}} \geq 3 \quad (5.7)$$

Variability cuts in the i_{P1} , z_{P1} , and y_{P1} filters are applied later.

In the studied area of Stripe 82, we have $\sim 74,000$ stars that passed the first four initial SDSS color cuts (Equations (5.1)–(5.4)), the PS1 magnitude cut (Equation (5.5)), and the PS1 threshold limit of the number of detections in both the g_{P1} and r_{P1} filters (Equations (5.6)–(5.7)).

Although there are 374 RRL stars in the same area, we missed 85 of them. Around 92% of these 85 stars did not have more than 2 clean g_{P1} or r_{P1} PS1 detections (Equations (5.6)–(5.7)) while the rest 8% of the missed RRL stars did not pass all of the four SDSS color cuts (Equations (5.1)–(5.4)). This leaves us with 289 true RRL stars that we recovered in Stripe 82 (among the $\sim 74,000$ stars that passed all the conditions in this step). The efficiency and completeness levels are then $\sim 0.39\%$ ($\frac{289}{74,000}$) and 77.3% ($\frac{289}{374}$), respectively.

- **Step (2):** In order to optimize our color selection of RRL candidates, we define color selection boundaries using the 636 RRL stars (see Section 5.2.2) in the SDSS ($u-g$) vs. ($g-r$) and ($g-r$) vs. ($r-i$) color-color diagrams with GMM (VanderPlas et al., 2012). GMM is a Bayesian generative classification method that fits different classes with simple non-correlated Gaussians. These Gaussians are then used to compute the likelihood of a point to belong to each class. The class with the highest likelihood is the predicted result. In our case, GMM uses the colors of the 636 pre-identified RRL stars and compares them to the colors of non-RRL stars to find the GMM color selection boundaries. We choose this method instead of adopting sharp rectangular cuts in order

to optimize our efficiency and completeness levels when light curve analyses are not possible due to the small number of PS1 observations.

In Figure 5.3 and Figure 5.4, the GMM color selection boundaries are applied and plotted in green in the $(u-g)$ vs. $(g-r)$ and $(g-r)$ vs. $(r-i)$ color-color diagrams, respectively, for a subsample of stars in Stripe 82. The colors of the 636 pre-identified RRL stars used to find the GMM color selection boundaries are shown with black open circles. Stars that fall inside our GMM selection boundaries are shown as blue dots while stars that fall outside are plotted as red dots. Only stars that fall inside the GMM color selection boundaries in both color-color diagrams ($(u-g)$ vs. $(g-r)$ and $(g-r)$ vs. $(r-i)$) are retained for further analysis.

This step significantly reduces the number of stars in our sample from $\sim 74,000$ to 1,820 stars, out of which 260 are true RRL stars.

Although the GMM color boundaries are computed using more than 600 well identified RRL stars distributed around the sky, 29 true RRL stars from Step (1) did not pass one or both of these GMM color boundary cuts. These stars either have relatively large SDSS magnitude uncertainties that are reflected in their colors or they fall close to, but outside of, our GMM color boundaries.

Because 1,820 stars passed all the cuts in this step (and the cuts in the previous step), and because we were able to recover 260 out of the 374 RRL stars found in Stripe 82, our efficiency level is $\sim 14.3\%$ ($\frac{260}{1,820}$) while the completeness level is 70% ($\frac{260}{374}$).

- **Step (3):** After defining and applying the GMM selection boundaries for the SDSS colors in the previous section, we use the g_{P1} , r_{P1} , i_{P1} , z_{P1} , and y_{P1} multi-epoch data from PS1 to distinguish a variable from a non-variable star.

Since we cannot rely on our small number of PS1 detections to phase the light curves and find their periods, we calculate low-order statistics (i.e., standard deviation) and use them to define a GMM selection boundary cut for the g_{P1} magnitudes as a function of the standard deviation in g_{P1} ($\sigma_{g_{P1}}$) plus the standard deviation in r_{P1} ($\sigma_{r_{P1}}$). In Figure 5.5, the GMM variability boundary plotted in green is computed by the GMM method (VanderPlas et al., 2012) which uses the $(\sigma_{g_{P1}} + \sigma_{r_{P1}})$ values of the 636 pre-identified RRL stars compared to the $(\sigma_{g_{P1}} + \sigma_{r_{P1}})$ values of non-variable stars to find the boundary of the variability cutoff. Although all of these 636 RRL stars are variable sources, only $\sim 90\%$ of them fall above our variability boundary, while $\sim 10\%$ show small or no variability due to the small number of epochs available from PS1. Only stars that fall above our GMM variability boundary are retained for further analysis. These stars have already passed the GMM selection boundaries for the SDSS colors discussed in the previous steps.

In order to be considered as RRL candidates, stars that have more than two clean detections in the i_{P1} , z_{P1} , and y_{P1} filters must pass the following additional variability criterion:

$$\sigma_{i_{P1}} + \sigma_{z_{P1}} + \sigma_{y_{P1}} \geq 0.1 \quad (5.8)$$

This threshold limit was adopted as more than 90% of the 636 pre-identified RRL stars (see Section 5.2.2) with more than 2 clean detections in the i_{P1} , z_{P1} , and y_{P1} filters have $\sigma_{i_{P1}} + \sigma_{z_{P1}} + \sigma_{y_{P1}} \geq 0.1$. This criterion is applied to stars with $N_{i_{P1}} \geq 3$, $N_{z_{P1}} \geq 3$, and $N_{y_{P1}} \geq 3$ that have already passed all of our GMM color and variability selection boundaries. Stars that passed our GMM color and variability selection boundaries and that do not have more than two good detections in the i_{P1} , z_{P1} , and y_{P1} filters are still considered RRL candidates. Applying the GMM variability selection cut (see Figure 5.5) for $(\sigma_{g_{P1}} + \sigma_{r_{P1}})$ and the variability cut in the i_{P1} , z_{P1} , and y_{P1} filters (see Equation (5.8)) to the 1,820 RRL candidates from Step (2) reduces the number of RRL candidates to 255 stars, out of which 195 are true RRL stars and 60 are contaminant stars. We discuss the nature of the 60 contaminant stars in Section 5.3.3.

At the same time, 65 RRL stars were lost when moving from Step (2) to Step (3). These stars did not show a significant amount of variability compared to other variable stars because their number of PS1 epochs is small (~ 3) and their magnitudes in different detections are not significantly different as they have likely been multiply observed at a relatively close phase.

In this final step, the efficiency significantly increases to $\sim 77\%$ ($\frac{195}{255}$) and the completeness drops to $\sim 52\%$ ($\frac{195}{374}$). This step greatly increases our efficiency level as it gets rid of a large fraction of non-variable stars with colors close to the colors of RRL stars (i.e., main-sequence stars with colors close to the colors of RRL stars).

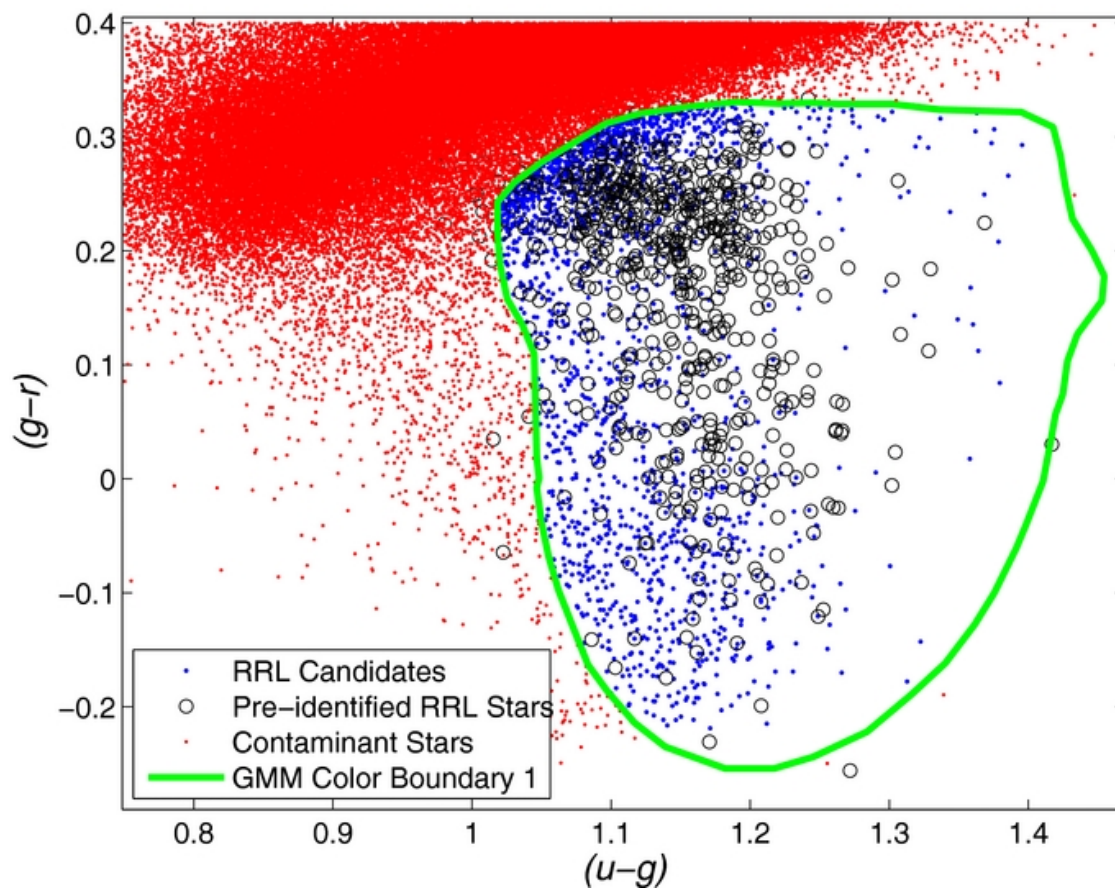


Figure 5.3: The $(u - g)$ vs. $(g - r)$ colors of the 636 pre-identified RRL stars used to find the GMM color selection boundary (plotted in green) are shown with black open circles. Stars that fall inside this boundary (blue dots) have RRL-like colors and are retained for further analysis. Stars falling outside the GMM boundary are plotted as red dots and are considered contaminant stars.

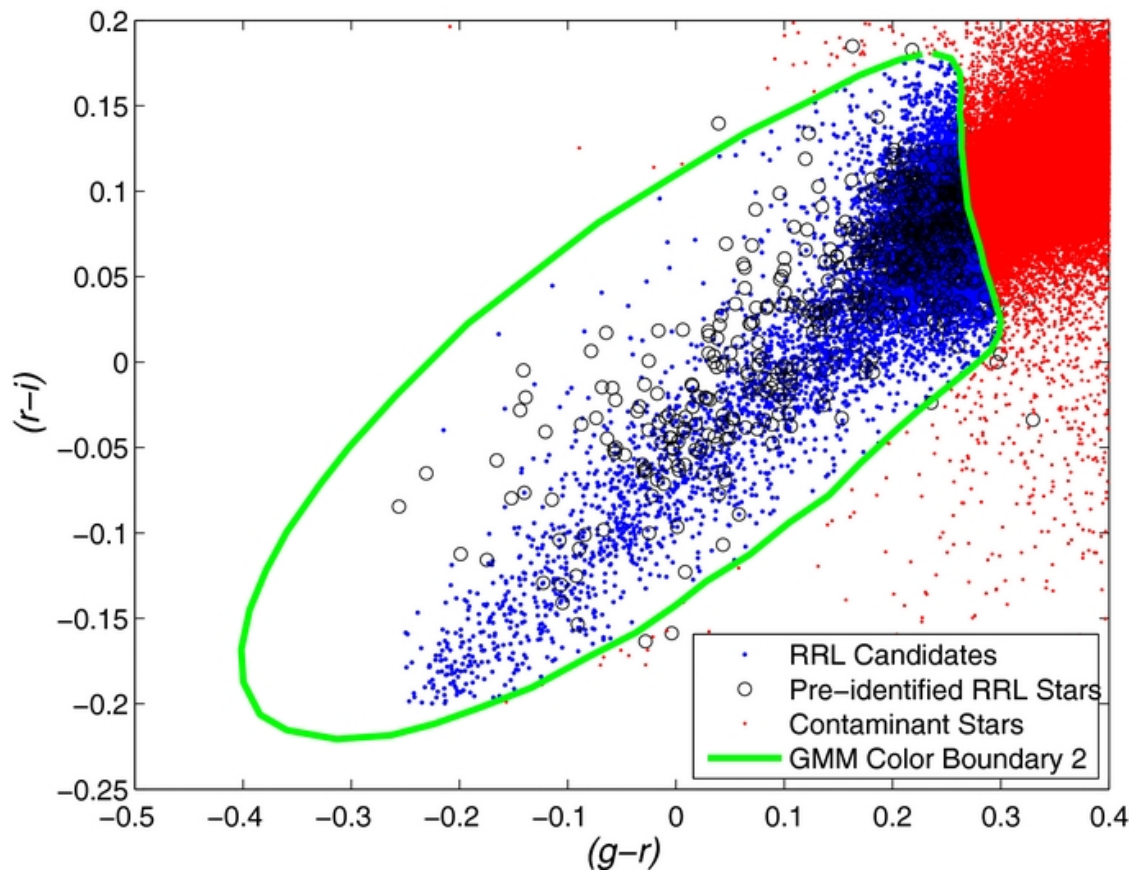


Figure 5.4: Same as Figure 5.3, but showing a $(g-r)$ vs. $(r-i)$ SDSS color-color diagram.

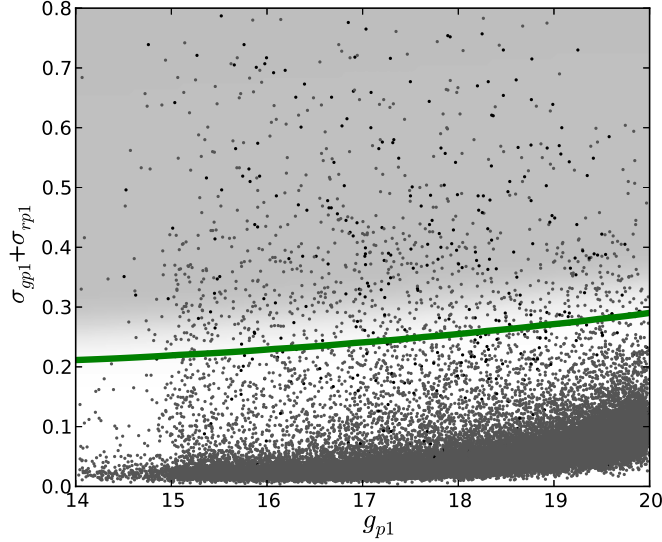


Figure 5.5: The g_{P1} vs. $(\sigma_{g_{P1}} + \sigma_{r_{P1}})$ distribution of a small sample of the stars that passed the SDSS GMM color selection cuts. The green line shows the variability boundary computed by GMM using the 636 pre-identified RRL stars. Stars falling above the variability boundary are retained for further analysis.

5.3.2 Applying Regular Rectangular Cuts

We apply the regularly used color and variability rectangular cuts (Sesar et al., 2010) to the stars in Stripe 82 and compare the results using this technique with the results we achieved using the GMM technique to test whether the latter technique improves the recovery of RRL stars.

The first step in this technique is similar to Step (1) from the previous section where the number of RRL candidates is $\sim 74,000$ stars of which 289 are known RRL stars. This step requires the SDSS rectangular color cuts, the magnitude cut, and the PS1 threshold limit of the number of detections in both, the g_{P1} and r_{P1} filters. The efficiency and completeness levels are then $\sim 0.39\%$ ($\frac{289}{74,000}$) and 77.3% ($\frac{289}{374}$), respectively.

Since we are not using the GMM technique in this section, we directly apply straight-line variability cuts in the PS1 filters. Stars with $(\sigma_{g_{P1}} + \sigma_{r_{P1}} \geq 0.22)$ that have passed the previous cuts in this section are retained for further analysis. The 636 pre-identified RRL stars were once again used to set the latter cut as more than 90% of these stars have $\sigma_{g_{P1}} + \sigma_{r_{P1}} \geq 0.22$. Just like in Step (3), an additional cut $(\sigma_{i_{P1}} + \sigma_{z_{P1}} + \sigma_{y_{P1}} \geq 0.1)$ is applied for the retained stars with $N_{i_{P1}} \geq 3$, $N_{z_{P1}} \geq 3$, and $N_{y_{P1}} \geq 3$. Retained stars that do not have more than two good detections in the i_{P1} , z_{P1} , and y_{P1} filters are still considered RRL candidates.

There are $\sim 1,600$ stars that passed all of our cuts in this section of which 205 are known RRL stars. This yields efficiency and completeness levels of $\sim 13\%$ ($\frac{205}{1,600}$) and $\sim 54\%$ ($\frac{205}{374}$), respectively.

The dependencies of the efficiency (dashed lines) and completeness (solid lines) levels in each step resulting from the GMM and rectangular cut techniques are plotted with red and blue lines in Figure 5.6, respectively. Although there was no significant change in the completeness level when using the rectangular cuts compared to the GMM technique, the efficiency level increased from $\sim 13\%$ ($\frac{205}{1,600}$, using rectangular cuts) to 77% ($\frac{195}{255}$, using the GMM technique). Hence, we favor using the GMM technique in future studies.

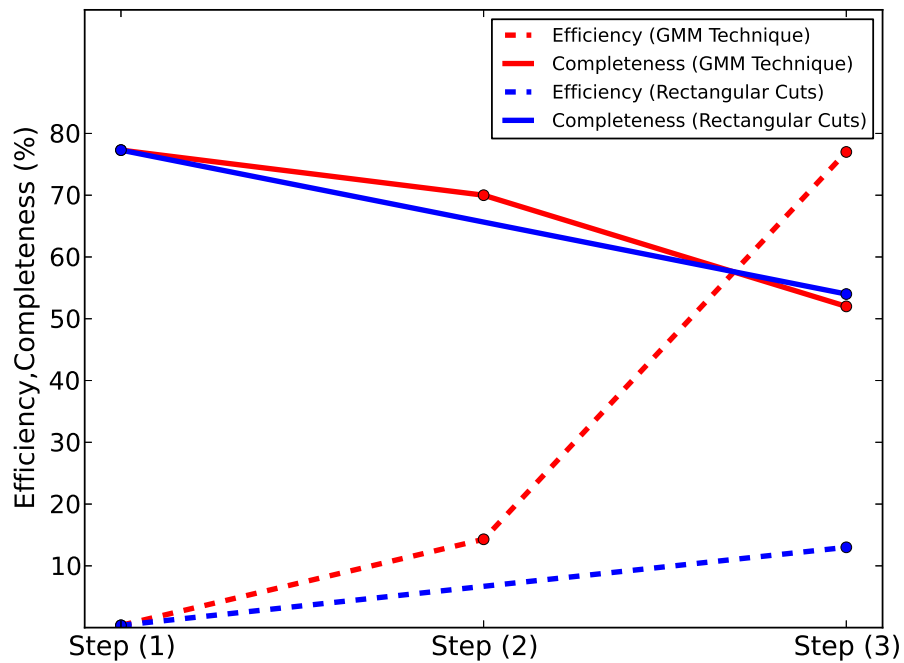


Figure 5.6: A comparison between the efficiency (dashed lines) and completeness (solid lines) levels on each step resulting from the GMM (in red) and rectangular (in blue) cuts techniques. The dependence of our GMM completeness and efficiency levels on Step (1): the magnitude, initial color, and number of detection cuts (Equations (5.1)–(5.7)), Step (2): the SDSS GMM color boundary cuts, and Step (3): the GMM variability boundary cut are also shown.

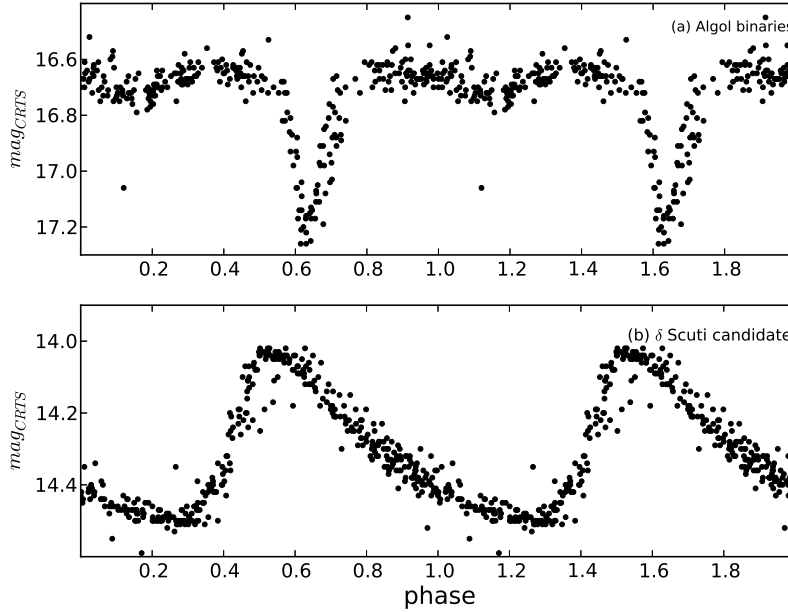


Figure 5.7: Phased light curves of (a): Stars in Algol binary systems ($ID_{CSS} = 18720940$), (b): δ Scuti candidate ($ID_{CSS} = 1109081021295$).

5.3.3 Contaminant Stars

To understand the nature of the contaminant stars, we look for multi-epoch data in the CSS database for the 60 contaminant stars we found in Stripe 82. 56 out of the 60 contaminant stars are found in the CSS database and have been observed between ~ 40 and 500 times.

Almost 40% of these stars showed no variability using the multi-epoch data from CSS, which makes them non-variable stars that have passed our variability cuts. These stars were observed only three to four times with PS1 and have magnitudes close to our bright ($g_{P1} \sim 14.0$ mag) and faint ($g_{P1} \sim 20.0$ mag) magnitude cuts. Hence, it is not surprising that some non-variable sources passed our variability cuts as their variability statistics are based on a small number of observations where a single noisy epoch can bias the statistics and make a non-variable source appear as a variable one, and vice versa.

The remaining 60% of the contaminant stars in Stripe 82 appeared as non-RRL variable stars using the CSS database. Their variability statistics reflected a change in their brightness over time but the shape of their light curve showed that most of them are W UMa, Algol binaries, δ Scuti, and SX Phe stars (Palaversa et al., 2013). Samples of the phased light curves for Algol binaries ($P = 0.6684$ days) and δ Scuti candidate ($P = 0.11367021$ days) stars that are contaminating our RRL stars are shown in panels (a) and (b) of Figure 5.7, respectively. We were able to recover the correct type and periods of these stars using the CSS multi-epoch data. Using the current PS1 data available, there is no way of getting rid of all the contaminants.

With the $\sim 77\%$ ($\frac{195}{255}$) efficiency level computed in the previous section, we know that $\sim 23\%$ of our RRL candidates are non-RRL stars (mainly non-variable stars and stars in eclipsing systems). However, we show in Section 5.5 that we are still able to detect halo substructures with such a contamination level. Additionally, the efficiency and completeness levels will be improved when more PS1 epochs are available in the near future. Our method can be useful in detecting RRL stars in surveys other than the PS1 where the number of detections per star is also small. Our efficiency

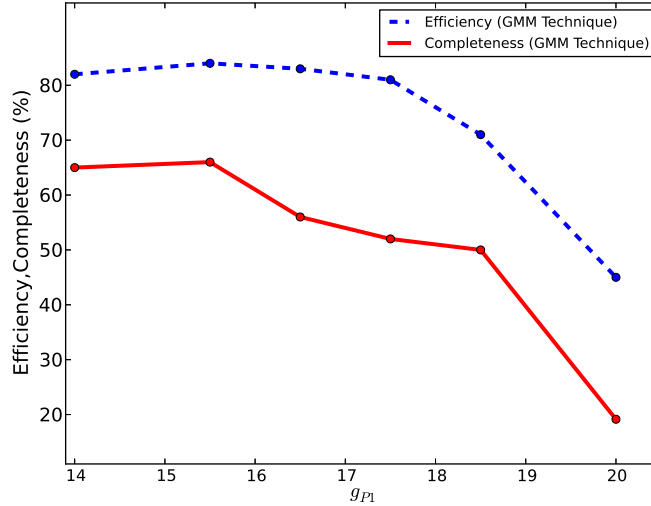


Figure 5.8: The decrease in the efficiency (blue dashed line) and completeness (red solid line) levels as a function of magnitude reflects the increase in contamination for fainter stars.

and completeness levels as a function of g_{P1} magnitudes are plotted in blue and red lines in Figure 5.8, respectively. The decrease in the efficiency and completeness levels as a function of magnitude reflects the increase in contamination for fainter stars.

5.4 RRL Candidates

Knowing that our efficiency and completeness levels are 77% ($\frac{195}{255}$) and $\sim 52\%$ ($\frac{195}{374}$), respectively, we apply our method to the whole SDSS \times PS1 overlapping footprint.

In the mentioned area, around 130,000 stars passed the first four initial SDSS color cuts (Equations (5.1)–(5.4)), the PS1 magnitude cut (Equation (5.5)), and the minimum number of PS1 epoch cuts (Equations (5.6)–(5.7)). These stars have also passed the two GMM selection boundaries in the SDSS colors defined and applied in Step (2) of Section 5.3.1.

Finally, we apply the GMM variability selection cut from Step (3) of Section 5.3.1 to these 130,000 stars. To illustrate this, we plot the g_{P1} vs $(\sigma_{g_{P1}} + \sigma_{r_{P1}})$ distribution for the sample of stars (spanning ~ 100 deg² of the sky) that passed our GMM color boundaries in the upper panel of Figure 5.9. Stars falling below our GMM variability boundary (green line) are plotted as blue dots and are considered non-variable stars. Stars passing the boundary are plotted as magenta dots and are considered RRL candidates. The lower panel of Figure 5.9 illustrates the distribution of the same stars, but showing a $\sigma_{g_{P1}}$ vs $\sigma_{r_{P1}}$ plot.

An additional variability cut was applied to all of our RRL candidates with $N_{i_{P1}} \geq 3$, $N_{z_{P1}} \geq 3$, and $N_{y_{P1}} \geq 3$. These stars must pass the i_{P1} , z_{P1} , and y_{P1} variability cut defined in Equation (5.8) ($\sigma_{i_{P1}} + \sigma_{z_{P1}} + \sigma_{y_{P1}} \geq 0.1$). Stars that passed all of our previous cuts and that do not have more than two good detections in the i_{P1} , z_{P1} , and y_{P1} filters are still considered RRL candidates.

Only 6% of the 130,000 stars passed these variability cuts which leaves us with 8,115 RRL candidates. Based on the analysis in Section 5.3.3, we believe that $\sim 23\%$ of these RRL candidates are non-RRL stars (mainly non-variable stars and stars in eclipsing systems).

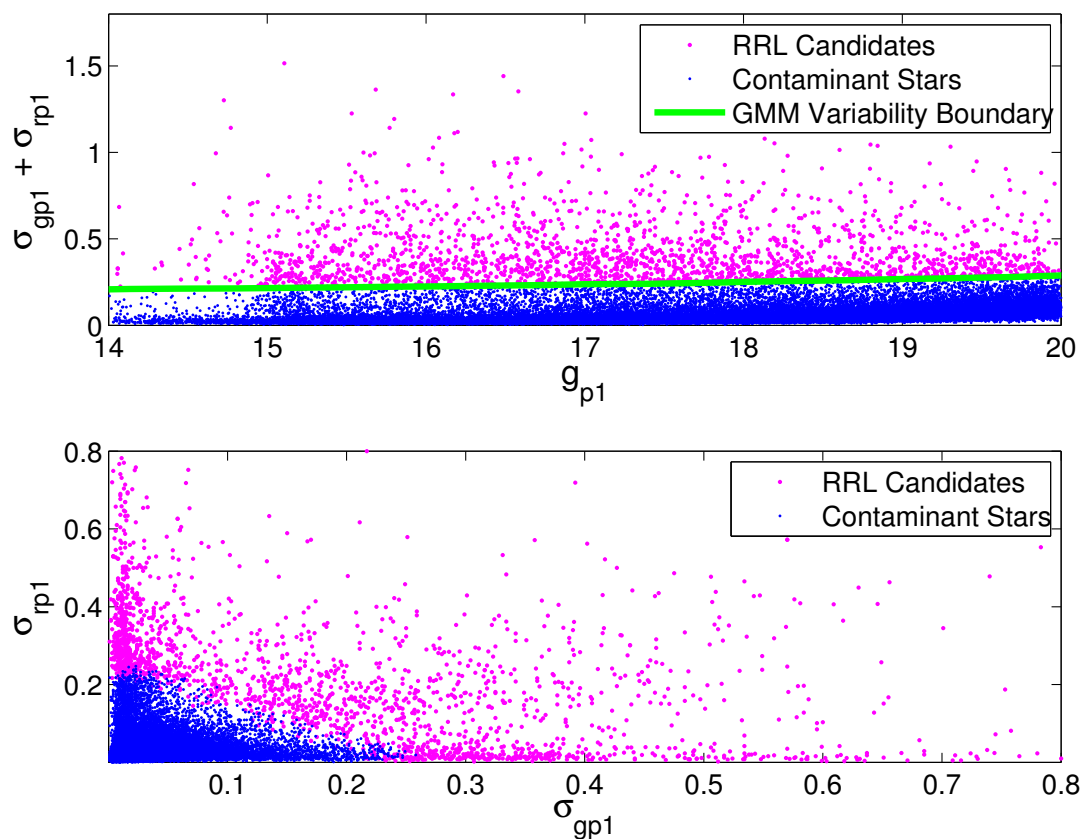


Figure 5.9: The upper panel illustrates how we apply our GMM variability selection boundary (green line) cut to distinguish variable (magenta dots) from non-variable (blue dots) stars in a g_{P1} vs $(\sigma_{g_{P1}} + \sigma_{r_{P1}})$ plot. Stars falling above our GMM variability boundary are considered to be RRL candidates. The lower panel shows the distribution of $\sigma_{g_{P1}}$ vs. $\sigma_{r_{P1}}$ of the same stars plotted in the upper panel.

5.5 Halo Substructure

One of the advantages of RRL stars is their well defined mean absolute $\langle V \rangle$ magnitude which makes it straightforward to find estimates for their distances. We determine the d_h of RRL stars using Equation 4.7 (See Section 4.8 for more details.). Our 8,115 RRL candidates have d_h in the ~ 3 –70 kpc distance range.

Using the 255 RRL candidates we detected in Stripe 82, we look for halo substructures in our covered distance range. We plot the number density distribution of these 255 RRL candidates in Figure 5.10. This plot includes our 60 contaminant stars in Stripe 82 (if we assume that Sesar et al.’s (2010) catalog of RRL stars is $\gtrsim 99\%$ complete).

The density of the points that is accentuated by the white contours is shown in scaled density levels. The smoothed surface regions with a high number of stars are indicated in red while regions with low number of stars are indicated in dark blue. We recover the HAC (Belokurov et al., 2007) at R.A.¹ $\sim -40^\circ$ and d_h between ~ 8 and ~ 24 kpc. The trailing arm of the Sgr dSph tidal stream (Majewski et al., 2003) is also recovered at R.A. $\sim 30^\circ$ and $d_h \sim 23$ kpc.

Both of our recovered substructures were seen using the $\sim 99\%$ complete and efficient catalog of RRL stars in Stripe 82 (Sesar et al., 2010). Although our method is not as efficient and complete as the mentioned catalog, Figure 5.10 proves that the efficiency and completeness levels we achieved are good enough to select RRL candidates to trace stellar streams and substructures in spite of the inclusion of contaminant stars. Stripe 82 was visited ~ 80 times by the SDSS, which made it relatively easy to find its RRL stars using light curve analysis (Sesar et al., 2010). In contrast, it was more difficult to find RRL stars in our study using only the SDSS colors and PS1 variability because of the small number of multi-epoch data available from PS1.

Nevertheless, we recovered $\sim 52\%$ of the RRL stars ($d_h < 70$ kpc) not only in the Stripe 82 region, but in the whole SDSS \times PS1 overlapping footprint.

Having additional PS1 epochs will improve the quality of our variability statistics which will improve the separation between variable and non-variable stars. Using the CSS data, we showed in Section 5.3.3 that 40% of our contaminant stars are non-variable sources and have small number of PS1 epochs. We expect to get rid of at least 60% of these non-variable contaminant stars when more PS1 epochs (~ 15 epochs in all filters) are available. However, it will not be possible to get rid of all of the contaminant stars as the number of PS1 epochs will not be sufficient to distinguish RRL from non-RRL variable stars using light curve and period analysis. Furthermore, having additional PS1 epochs will improve our completeness level as we missed many RRL stars due to the PS1 threshold limit of the number of detections in both the g_{P1} and r_{P1} filters (Equations (5.6)–(5.7)). We expect the efficiency and completeness level to increase to at least $\sim 83\%$ and $\sim 65\%$ when all of the PS1 epochs are available. Having additional epochs will also allow us to study stars in the halo that are further than 70 kpc (d_h).

5.6 Summary

In this study, we combine data from two different sky surveys (SDSS and PS1) to look for RRL candidates in the halo. We select the RRL candidates using SDSS color cuts and PS1 variability cuts. We show that using a GMM method to define GMM boundary cuts optimizes the efficiency and completeness levels to select RRL stars (or other type of variable stars) when light curve analyses are not available.

We start by adopting initial color cuts for RRL stars from Sesar et al. (2010). In order to optimize the selection of our RRL candidates, we use 636 pre-identified RRL stars from the CSS and LINEAR to define GMM color selection boundaries in the SDSS ($u - g$) vs. ($g - r$) and ($g - r$) vs. ($r - i$) color-color diagrams in addition to a GMM variability boundary cut for the (g_{P1} vs. $\sigma_{g_{P1}} + \sigma_{r_{P1}}$) diagram. We applied another variability cut in the i_{P1} , z_{P1} , and y_{P1} filters from PS1. A comparison between our efficiency and completeness levels using the GMM method to the efficiency and completeness levels using rectangular cuts that are commonly used yielded a significant increase in the efficiency level from $\sim 13\%$ ($\frac{205}{1,600}$) to $\sim 77\%$ ($\frac{195}{255}$) and an insignificant change in the completeness levels. Hence, we favor using the GMM technique in future studies.

We used the multi-epoch data from the CSS database to study the properties of our contaminant stars found in Stripe 82. Around 40% of the contaminant stars showed no sign of variability in the CSS data. Because these stars have

¹Add 360° to obtain the correct values of R.A. when R.A. $< 0^\circ$. Negative values of R.A. were used for better visualization only.

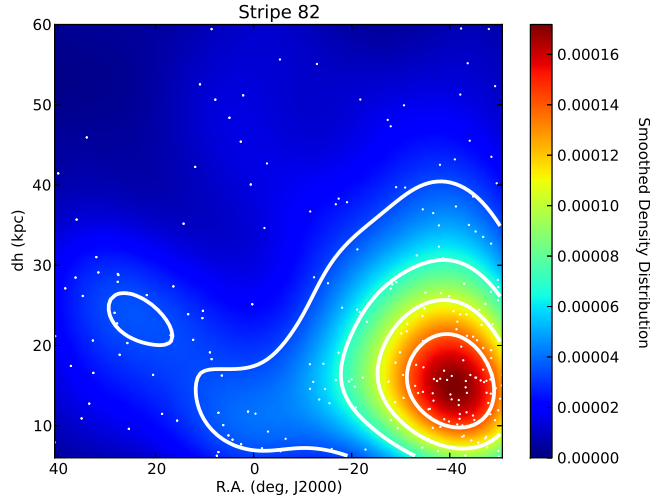


Figure 5.10: The number density distribution of the RRL stars in Stripe 82 is plotted with scaled density levels that are accentuated by the white contours. The HAC appears at R.A. $\sim -40^\circ$ and d_h between ~ 8 and ~ 24 kpc while the Sgr dSph tidal stream is detected at R.A. $\sim 30^\circ$ and $d_h \sim 23$ kpc. Negative values of R.A. were used for better visualization only (R.A. = R.A. + 360° when R.A. $< 0^\circ$)

between ~ 40 and 500 CSS epochs compared to ~ 8 epochs in g_{P1} and r_{P1} , we favor the CSS variability statistics and consider that these stars are contaminating our RRL candidates sample. Noisy detections, poor seeing, and non photometric conditions in the PS1 filters are the reasons for why these stars appeared to be variables in the latter photometric system. Although the remaining 60% of the contaminant stars in Stripe 82 showed variability using the CSS data, their variability properties indicate that most of them are W UMa, Algol binaries, δ Scuti, and SX Phe stars.

Having achieved our best efficiency (77%) and completeness (52%) levels, we apply our selection criteria and cuts to the whole SDSS \times PS1 overlapping footprint. Our technique yielded the detection of 8,115 RRL candidates. From the analysis in Section 5.3.3, we believe that $\sim 23\%$ of our RRL candidates are non-RRL stars (mainly non-variable stars and stars in eclipsing systems). Since light curve analysis is not possible in our study, we believe that achieving such a high efficiency and small contamination level reflects the success of our method. With the current PS1 data available, there is no way of getting rid of the contaminants. But it is plausible to assume that getting the remaining PS1 epochs yet to be observed (~ 3 epochs per filter) would eliminate more contaminant stars and recover more RRL stars. Our method can be applied to data from any multi-band survey where the number of multi-epoch data is small.

We obtain distance estimates for our RRL stars to test if we are still able to detect halo stellar streams and substructures with our efficiency and completeness levels. Although $\sim 23\%$ of the 255 RRL candidates in Stripe 82 are not true RRL stars and although we missed $\sim 50\%$ of the known RRL stars within the magnitude range considered here, we were still able to recover the HAC and the arm of the Sgr dSph tidal stream (see Figure 5.10). This proves that our method is good enough to detect some of the halo substructures and stellar streams in the halo.

The technique developed in this paper can be adopted to optimize the selection of a specific type of variable stars when light curve analyses are not possible while the technique developed in Chapter 4 (Abbas et al., 2014a) can be adopted when a large number of repeated observations are available.

The Oosterhoff Populations in the Milky Way's Halo

Women are like flowers. They should be treated gently, kindly, and with affection. Imam Ali

Abstract We use the largest currently existing catalog of RRab stars from the CSS (Drake et al., 2013a) to study the different Oosterhoff populations in the halo. The CSS RRab stars cover $\sim 20000 \text{ deg}^2$ of the sky to d_h up to ~ 60 kpc. Using the CSS RRab stars, we clearly detect two distinct Oosterhoff populations in the halo, the OoI and OoII populations. We use the [Fe/H] information obtained from the SDSS, to show that RRab_{OoI} stars are, on average, more metal-rich than RRab_{OoII} stars. Consistent with previous studies with smaller sky coverage, we show that $\sim 73\%$ of the halo RRab stars are of OoI type, and we present the mean periods and metallicities of the halo RRab_{OoI} and RRab_{OoII} stars. By examining the ratio of RRab_{OoI} and RRab_{OoII} stars with Galactocentric distances (R_{gc}), we detect two turning points at $R_{gc} \sim 25$ kpc and $R_{gc} \sim 45$ kpc. We believe that these turning points are associated with breaks in the power-laws of the halo and that they divide the stellar halo into three main components: the inner halo, the outer halo, and the “extreme outer halo” components. As parts of the trailing arm of the Sgr dSph galaxy, the Virgo substructure, and the HAC are located in the footprint of the CSS RRab stars, we also study their specific Oosterhoff populations. We conclude that these substructures are dominated by RRab_{OoI} stars ($\sim 80\%$) and that the mean periods of their RRab stars fall near the boundary of the Oosterhoff gap; results that suggest that they had dSph galaxy progenitors.

This chapter is based on: Abbas, M., Grebel, E., and Huxor, A. (in prep.)

6.1 Introduction

Understanding the Oosterhoff effect, which we discussed in Section 2.6, can help in understating the formation history of the Galaxy. In this Chapter, we will investigate the Oosterhoff effect in the Milky Way's halo using the combined catalogs of RRab stars from Drake et al. (2013a), Drake et al. (2013b), and Drake et al. (2014) (hereafter, the CSS catalog). Although the new catalog of RRab stars from Drake et al. (2014) is similar to the two previously published ones (Drake et al., 2013a,b), their new catalog did not include extinction and distance information. To be consistent with the two previous catalogs, we correct their V magnitudes for extinction using the Schlegel et al. (1998) dust maps, adopt average magnitude of $M_v = 0.61$ mag, and calculate distances for the additional ~ 2400 stars using Equation 4.7.

Although we already mentioned some of the previous studies that investigated the Oosterhoff effect in the halo in Section 3.7, it is important to study this effect using the new CSS catalog for several reasons.

The latter catalog covers a much larger area of the sky compared to the areas covered by the previous studies (i.e., 1430 deg^2 from Miceli et al. 2008, and 840 deg^2 in the LSQ Survey). Such a large coverage provides us with more accurate results for the halo as a whole and for substructures covered by the catalog. For instance, Zinn et al. (2014) did not find a variation in the fraction of the OoI stars with distance but they emphasized the importance of testing the latter variation with a larger sample of RRL stars. Table 3.3 shows a list of the different catalogs we mentioned, their depths, areas, and number of RRL stars. Although the LSQ catalog covers RRL stars that are more distant than those covered by the CSS combined catalog, the latter catalog is more complete and thus more RRab stars are included in our analyses in our covered distance range (see figure 10 from Zinn et al. (2014) for a comparison between the completeness of their catalog with the CSS catalog).

Last but not least, the catalog we are using in this study includes ~ 2400 additional CSS RRab stars (of which ~ 35 are in the direction of the HAC) than the one used by Simion et al. (2014). These are the stars from Drake et al. (2014) that have been published after Simion et al.'s (2014) study came out. Thus, we use this more complete catalog to study the different Oosterhoff groups in the halo as a whole and in three different halo substructures: part of the Sgr dSph (Ibata et al., 1995), the Virgo substructure (Jurić et al., 2008), and the HAC.

In Section 3.7 we described the properties of the CSS RRab stars as well as other surveys and catalogs used in this study. We study the different Oosterhoff groups in the halo in Section 6.2 and we present the mean periods and metallicities of the OoI and OoII RRab stars. In Section 6.2.1 we examine the change of the OoI and OoII RRab stars with distance and we compare these changes with previous studies. In Section 6.3, we compare the numbers of OoI and OoII RRab stars in the direction of the trailing arm of the Sgr dSph, the Virgo substructure, and the HAC. Section 6.4 provides a summary of the important points and results.

6.2 The Oosterhoff Groups in the Stellar Halo

To check whether the different Oosterhoff groups are present in the stellar halo, we compare the locations of our RRab stars with the mean loci for RRab OoI (RRab_{OoI}) and RRab OoII (RRab_{OoII}) stars from Zorotovic et al. (2010). The P–A density plot is shown in Figure 6.2 where the number of CSS RRab stars are color-coded according to the legend. The mean loci for RRab_{OoI} and RRab_{OoII} stars from Zorotovic et al. (2010) are plotted with the solid and dashed lines, respectively. We add 0.15 mag for the CSS amplitudes to correct for the underestimated CSS amplitudes (Drake et al., 2013a).

For each RRab star, we calculate the difference (ΔP) between its actual period from the CSS catalog (P_{ab}) and its predicted period from the OoI locus ($P_{OoI-locus}$, the solid line in Figure 6.2) using Equation (6.1). We plot the ΔP distribution for all the CSS stars in the upper panel of Figure 6.3 where we observe one primary peak at $\Delta P \sim 0\text{d}$ and another secondary peak at $\Delta P \sim 0.1\text{d}$. The primary peak at $\Delta P \sim 0\text{d}$ indicates that most of the CSS RRab periods agree well with the periods predicted from the OoI locus adopted from Zorotovic et al. (2010). The secondary peak at $\Delta P \sim 0.1\text{d}$ indicates the presence of a different group of RRab stars in the halo, the OoII population.

We adopt $\Delta P = 0.045\text{d}$ from Miceli et al. (2008) as a threshold cut to separate RRab_{OoI} ($\Delta P \leq 0.045\text{d}$) and RRab_{OoII} ($\Delta P > 0.045\text{d}$) stars.

$$\Delta P = P_{ab} - P_{OoI-locus} \begin{cases} RR_{OoI} & \text{if } \Delta P \leq 0.045\text{d} \\ RR_{OoII} & \text{if } \Delta P > 0.045\text{d} \end{cases} \quad (6.1)$$

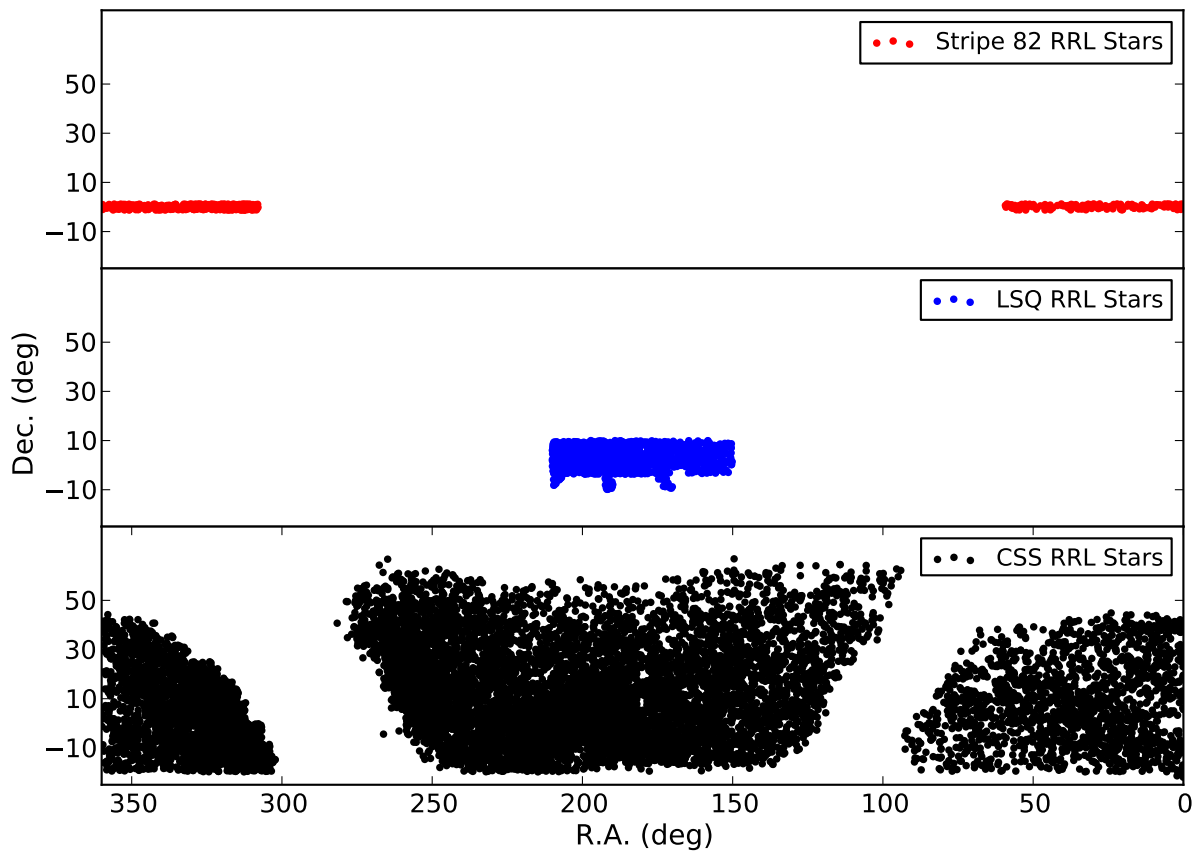


Figure 6.1: Lower to upper panels: spatial distribution of the CSS RRab stars, LSQ RRL stars, and the Stripe 82 RRL stars in equatorial coordinates.

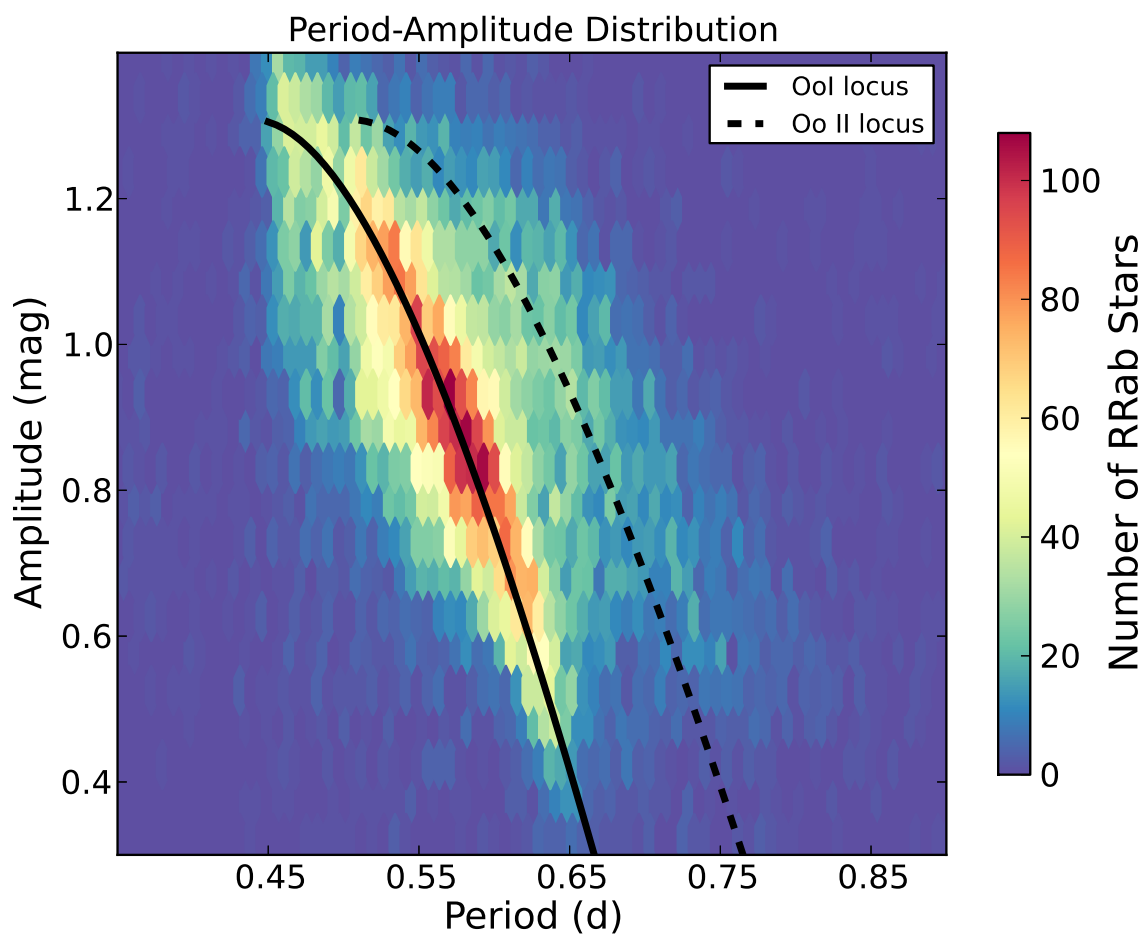


Figure 6.2: The P–A density plot of the CSS RRab stars. The numbers of RRab stars in each bin are color-coded according to the legend. Solid and dashed lines represent the RRab OoI and RRab OoII loci, respectively, and are adopted from Zorotovic et al. (2010).

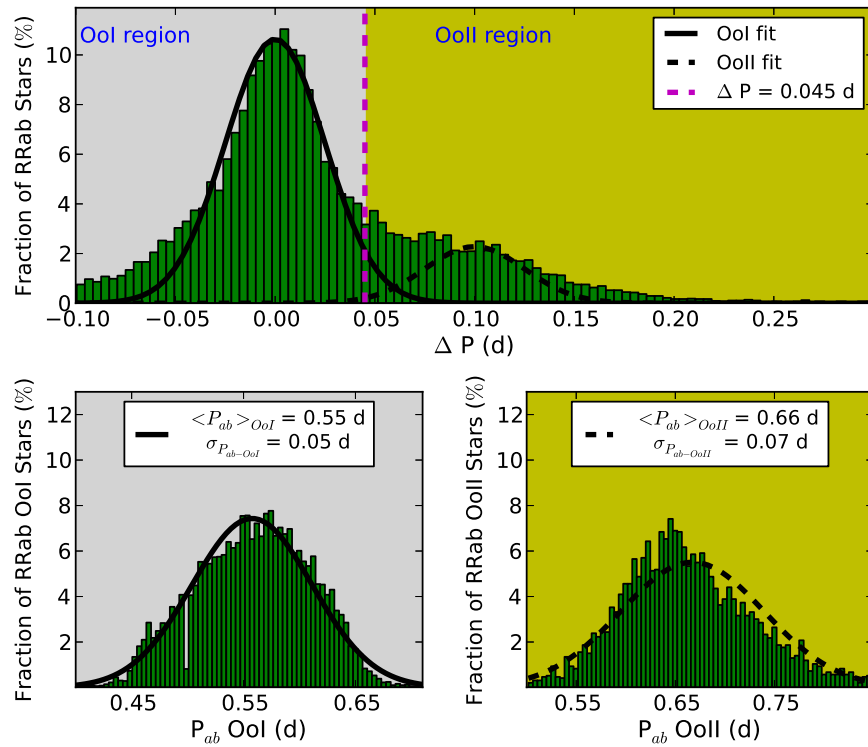


Figure 6.3: The ΔP distribution is shown in the upper panel where primary (at $\sim \Delta P = 0$ d) and secondary (at $\sim \Delta P = 0.1$ d) peaks are observed and fitted with two different Gaussian distributions. The magenta horizontal dashed line indicates the threshold limit between the OoI and OoII components ($\Delta P = 0.045$ d). The lower left and lower right panels show the period distributions of the RRab_{OoI} ($\Delta P \leq 0.045$ d) and RRab_{OoII} ($\Delta P > 0.045$ d) stars, respectively, and their Gaussian fits. Grey and yellow backgrounds indicate OoI and OoII regions, respectively.

The OoI and OoII regions are plotted with grey and yellow backgrounds in the different subplots in Figure 6.3. We present the mean periods of the OoI ($\langle P_{ab} \rangle_{OoI} = 0.55 \pm 0.05\text{d}$) and OoII RRab ($\langle P_{ab} \rangle_{OoII} = 0.66 \pm 0.07\text{d}$) stars in the halo using the Gaussian fits plotted in black in the lower panels of the same Figure. These values are very close to the mean periods of the OoI and OoII clusters found in previous studies (Clement et al., 2001; Catelan, 2009; Contreras Ramos et al., 2013). In agreement with other studies with smaller sky coverage (i.e., Miceli et al. 2008; Zinn et al. 2014), we find that $\sim 73\%$ of the CSS RRab stars are of OoI type.

We take advantage of the [Fe/H] information provided by Drake et al. (2013a) for ~ 1300 CSS RRab stars to examine the differences between the metallicities of OoI ($[\text{Fe}/\text{H}]_{OoI}$) and OoII ($[\text{Fe}/\text{H}]_{OoII}$) RRab stars. These spectroscopic metallicities were obtained from the 8th data release of the SDSS (SDSS DR8; Fukugita et al. 1996; Aihara et al. 2011).

In Figure 6.4a we plot the fraction of RRab_{OoI} (N_{RRab}^{OoI})¹ and RRab_{OoII} (N_{RRab}^{OoII}) stars with respect to [Fe/H] (using 0.2 dex binning) in blue and red lines, respectively. The error bars shown are computed assuming Poissonian noise on N_{Oo} . In Figure 6.4b we show the [Fe/H] vs. $(u - g)_0$ plot for the ~ 1300 CSS RRab stars with [Fe/H] information in the SDSS DR8 database. The latter plot shows that the number of RRab_{OoII} stars (red filled circles) decreases as the metallicity increases. In contrast, the number of RRab_{OoI} stars (blue crosses) increases as the metallicity increases. The RRab_{OoII} stars with ΔP near the threshold cut ($0.045 < \Delta P (d) < 0.065$) are shown with white filled circles.

Using the [Fe/H] distribution of RRab OoI and OoII stars plotted in the lower left and lower right panels of Figure 6.4, respectively, we find a mean [Fe/H] of RRab_{OoI} stars ($\langle [\text{Fe}/\text{H}] \rangle_{OoI} = -1.57$ dex, and RRab_{OoII} stars ($\langle [\text{Fe}/\text{H}] \rangle_{OoII} = -1.88$ dex. Thus, in agreement with previous studies (i.e., Dotter et al. 2010; Smith et al. 2011; Cusano et al. 2013; Kennedy et al. 2014), we confirm that the Oosterhoff groups in the halo are connected to the metallicity and that RRab_{OoI} stars are, on average, more metal-rich than RRab_{OoII} stars. These different groups represent different populations and formation histories.

6.2.1 Changes in the Oosterhoff Populations With Galactocentric Distance

It is interesting to examine changes in N_{RRab}^{OoI} as a function of R_{gc} . Detecting changes or turning points in N_{RRab}^{OoI} might help to trace the different components of the halo (such as an inner and outer halo). We start by calculating the R_{gc} of the CSS stars using Equation (6.2):

$$R_{gc} = (X^2 + Y^2 + \frac{Z^2}{q^2})^{1/2} \quad (6.2)$$

where q is the flattening parameter. (X, Y, Z) are Cartesian coordinates with an origin at the Galactic center. The Z -axis points towards the Galactic North Pole, the X -axis points in the direction of the Sun, the Y -axis points in the direction of the Galactic Rotation, and the Sun's location is at $(-8, 0, 0)$ kpc. When Simion et al. (2014) compared their RRL stars with different density models they concluded that the models that best reproduced the observations were from Deason et al. (2011) and Sesar et al. (2011b). Thus we adopt $q \sim 0.71$ (Sesar et al., 2011b) to find the distances in Equation (6.2). Before investigating changes in N_{RRab}^{OoI} with distance, and in order not to bias our results, we removed stars that lie in the direction of known halo substructure (Sgr dSph, VSS, etc.).

We show the R_{gc} distribution ($5 < R_{gc} < 55$ kpc) for the CSS RRab stars that are not located in the direction of any known halo substructure in the lower panel of Figure 6.5. Grey filled and red open histograms correspond to N_{OoI} and N_{OoII} , respectively. The change of N_{RRab}^{OoI} with distance is shown in the upper panel of the same figure and the errors are calculated assuming Poissonian noise on N_{OoI} . Two turning points at $R_{gc} \sim 25\text{--}30$ and $R_{gc} \sim 45\text{--}50$ kpc where the fraction of OoI stars reaches a local maximum are detected in the upper panel of Figure 6.5.

Different types of halo tracers like RRL, horizontal-branch, blue straggler, and main-sequence stars have been used to study the Galactic structure and the number density profile of the halo (e.g., Saha 1985; Bell et al. 2008; de Jong et al. 2010; Deason et al. 2011; Sesar et al. 2011b; Zinn et al. 2014; Simion et al. 2014) and comparable breaks have been detected at $R_{gc} \sim 25$ kpc (e.g., Beers et al. 2012; Sesar et al. 2011b; de Jong et al. 2010). The first turning point at $R_{gc} \sim 25\text{--}30$ kpc in the upper panel of Figure 6.5 is consistent with this break. Although Zinn et al. (2014) confirmed this break by studying the number density distribution of the LSQ catalog of RRL stars, they did not detect

¹ $N_{RRab}^{OoI} = \frac{N_{OoI}}{N_{OoI} + N_{OoII}}$ where N_{OoI} is the number of RRab OoI stars. Similarly for N_{RRab}^{OoII} .

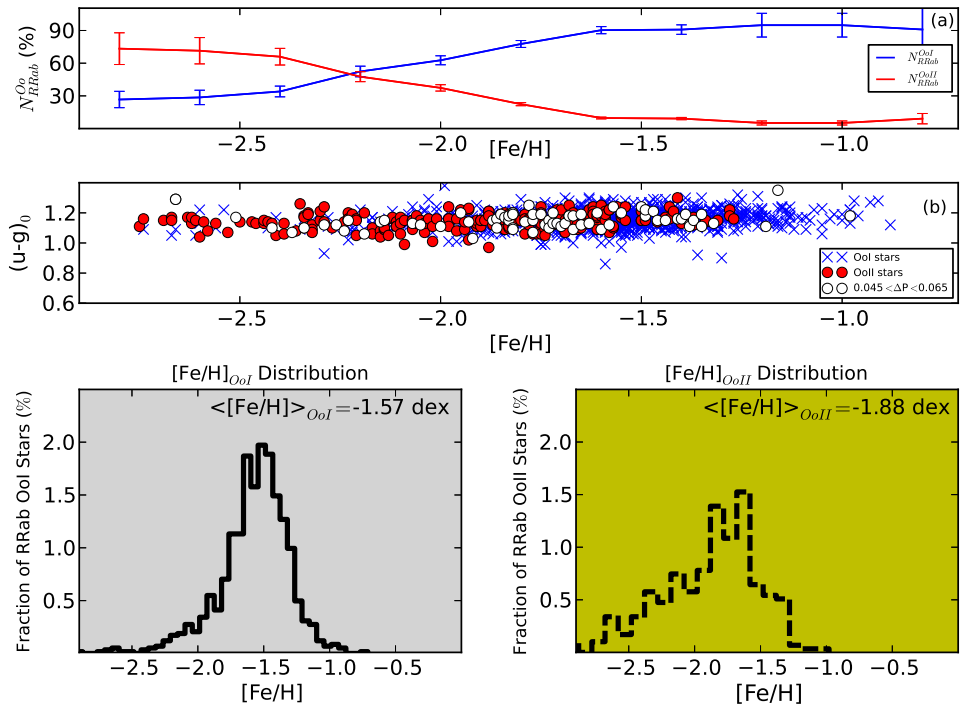


Figure 6.4: Panel (a): The distributions of N_{RRab}^{OoI} (blue line) and N_{RRab}^{OoII} (red line) with respect to $[Fe/H]^3$ are shown. Panel (b): $[Fe/H]$ vs. $(u - g)_0$ plot of $RRab_{OoI}$ (blue crosses) and $RRab_{OoII}$ (red filled circles) stars. $RRab_{OoII}$ stars with $0.045 < \Delta P < 0.065$ are shown with white filled circles. Lower panels: The $[Fe/H]$ distribution of $RRab_{OoI}$ ($[Fe/H]_{OoI}$) and $RRab_{OoII}$ ($[Fe/H]_{OoII}$) stars are plotted in the lower left and right panels, respectively.

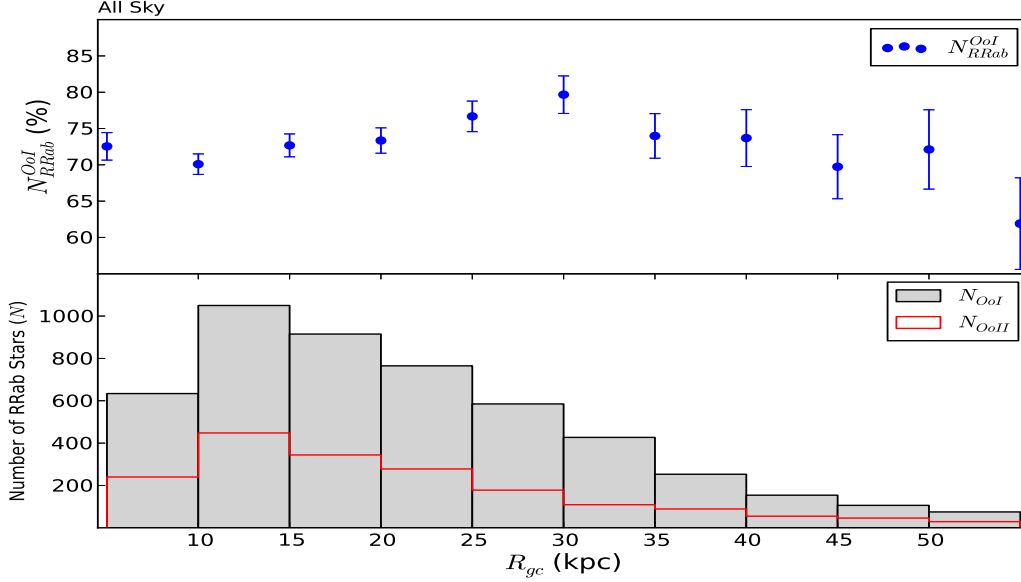


Figure 6.5: Upper panel: The N_{RRab}^{OoI} ratios in each Galactocentric distance bin are shown with their error bars. Lower panel: Histograms of the Galactocentric distance (R_{gc}) distribution for all CSS $RRab_{OoI}$ and $RRab_{OoII}$ stars not in the direction of any known halo substructure are shown in grey and red, respectively.

a change in N_{RRab}^{OoI} with distance. Since our catalog covers a much larger portion of the sky, we believe that the turning point detected at $R_{gc} \sim 25$ kpc is associated with the break in the halo and the different formation scenarios of the inner halo which is believed to be made largely by the accretion of a few massive systems in addition to in situ star formation processes, and the outer halo which mainly resulted from mergers and accretions of smaller systems (De Lucia & Helmi, 2008; Cooper et al., 2010). The second turning point at $R_{gc} \sim 45$ – 50 kpc might be associated with the break in the power-law detected by Keller et al. (2008) and Akhter et al. (2012) using RRL stars from the Southern Edgeworth-Kuiper Belt Object (SEKBO, Moody et al. 2003) survey. We believe that the latter turning point reflects an “extreme outer halo” component. Thus, the two turning points detected show three main components in the stellar halo: the inner halo, the outer halo, and the “extreme outer halo” components.

6.3 The Oosterhoff Groups in the substructures of the halo

In this section, we study the presence and properties of the different Oosterhoff populations in three main halo substructures that are detected by the CCS RRab stars.

6.3.1 Part of the Sagittarius Stream

After the discovery of the Sgr dSph (Ibata et al., 1995), tidal debris associated with it was detected and studied (i.e., Ivezić et al. 2000; Yanny et al. 2000; Vivas et al. 2001; Newberg et al. 2002, 2003; Law & Majewski 2010). For instance, Majewski et al. (2003) traced the Sgr dSph trailing tail and part of the leading arm using M giants.

We start by testing our RRab Oosterhoff classification technique by comparing our RRab OoI and OoII stars with those found in the catalog of RRL stars in Stripe 82 (Sesar et al., 2010) that overlap with the Sgr tidal stream.

Using the 38 RRL stars located in the Sgr tidal stream in Stripe 82, Sesar et al. (2010) found that $\sim 76\%$ of them belong to the OoI population and that the median period of its RRab stars is 0.6d. Likewise, we applied the method described in Section 6.2 to the 35 CSS RRab stars located in the same region. Our results were very similar to those found by Sesar et al. 2010 ($\sim 77\%$ are RRab_{OoI} stars and have a median period ~ 0.6 d).

However, because the CSS catalog of RRab stars covers a much larger portion of the sky (20000 deg²) and of the Sgr trailing arm in comparison to the area covered by Sesar et al. (2010) in Stripe 82 (270 deg²), we study the Oosterhoff groups in the Sgr tidal stream. In the upper panel of Figure 6.6, we plot the histogram of the ~ 440 CSS RRab stars ($d_h < 35$ kpc) that lie in the direction of the trailing tail of the Sgr dSph (Majewski et al., 2003) to study N_{RRab}^{OoI} and N_{RRab}^{OoII} at different distances. The completeness level of the CSS catalog reaches a maximum of $\sim 90\%$ at $d_h \sim 18$ kpc (Drake et al., 2014) and decreases at farther distances to $\sim 50\text{--}60\%$. Because the changes in the completeness levels with distance should affect both RRab^{OoI} and RRab^{OoII} stars at the same rate, and because our analyses are based on the ratio of N_{RRab}^{OoI} and N_{RRab}^{OoII} , we believe that these changes do not have a significant effect on our results.

We find that N_{RRab}^{OoI} in the Sgr tail studied here reaches its maximum ($\sim 80\text{--}85\%$) at d_h in the 15–30 kpc distance range compared to a $N_{RRab}^{OoI} \sim 71\%$ for $d_h < 15$ kpc. The RRab_{OoI} excess in the upper panel of Figure 6.6 for the intermediate (Sgr, $15 < d_h < 30$ kpc) RRab stars compared to the nearby ($d_h < 15$ kpc) RRab stars suggest that the intermediate and nearby RRab stars have different formation histories and metallicities. The P–A distribution for the intermediate RRab_{OoI} and RRab_{OoII} stars (d_h in the 15–30 kpc distance range) are plotted in the lower panel of Figure 6.6 with blue filled and red open circles, respectively. We find that the mean period of RRab stars belonging to the trailing tail of the Sgr dSph ($\langle P_{ab}^{SgrTail} \rangle = 0.58$ d) lies near the boundary of the Oosterhoff gap.

The RRab_{OoI} excess and the mean period of $\langle P_{ab}^{SgrTail} \rangle = 0.58$ d of the intermediate RRab stars located in the Sgr direction suggest a dSph progenitor nature of these stars. Although we already know from other studies that there is an overdensity in this area that is associated with the Sgr dSph, it is interesting to confirm this result using the Oosterhoff populations.

6.3.2 The Virgo Substructure

Although the Virgo substructure is one of the most dominant and studied substructures in the halo (Vivas & Zinn, 2006; Duffau et al., 2006; Jurić et al., 2008; Bonaca et al., 2012; Duffau et al., 2014), its origin and properties are not well understood. It extends between 1000 deg² (Martínez-Delgado et al., 2007; Jurić et al., 2008) and 3000 deg² (Bonaca et al., 2012) in the sky and is located in the 5–20 kpc distance range (Jurić et al., 2008). The two main parts in the Virgo substructure are the VSS (Duffau et al., 2006) and the Virgo Overdensity (VOD, Jurić et al. 2008). Whether the VSS and VOD have the same progenitor or not is still being debated (e.g., Vivas et al. 2008; Carlin et al. 2012). See Bonaca et al. (2012) and Duffau et al. (2014) for a detailed discussion of the Virgo substructure.

We compare the N_{RRab}^{OoI} for CSS RRab stars located in the Virgo substructure region ($260^\circ < l < 310^\circ$, $50^\circ < b < 80^\circ$, $d_h < 22$ kpc) with the N_{RRab}^{OoI} for CSS RRab located in a comparison field ($0^\circ < l < 80^\circ$, $45^\circ < b < 70^\circ$, $d_h < 22$ kpc)⁴ that is free of known substructures. If the halo is symmetric, the N_{RRab}^{OoI} distribution in different locations should be similar. However, we find that $N_{RRab}^{OoI} \sim 80\%$ and $\sim 69\%$ in the Virgo substructure and comparison field regions, respectively. The N_{RRab}^{OoI} excess in the Virgo substructure can be explained by a possible dSph progenitor. To further investigate this excess, we plot the histograms of RRab_{OoI} (in grey) and RRab_{OoII} (in red) stars located in the Virgo substructure and comparison field regions in the lower and upper panels of Figure 6.7, respectively, and we provide the N_{RRab}^{OoI} fractions in blue for each distance bin.

Although N_{RRab}^{OoI} does not exceed $\sim 74\%$ in most of the distance bins of the comparison field, in the Virgo substructure region it reaches values greater than 81% in the 4–6, 8–10, 14–18, and 20–22 kpc distance ranges and $\sim 78\%$ in the 18–20 kpc distance range. In agreement with other studies, these values reflect the spread of the Virgo substructure in the $\sim 5\text{--}21$ kpc distance range (Jurić et al., 2008). Similar to $\langle P_{ab}^{SgrTail} \rangle$, the mean period of RRab stars in the Virgo substructure ($\langle P_{ab}^{Virgo} \rangle$) lies near the boundary of the Oosterhoff gap, $\langle P_{ab}^{Virgo} \rangle = 0.58$ d, which again suggests a dSph progenitor origin.

⁴Adopted from Simion et al. (2014)

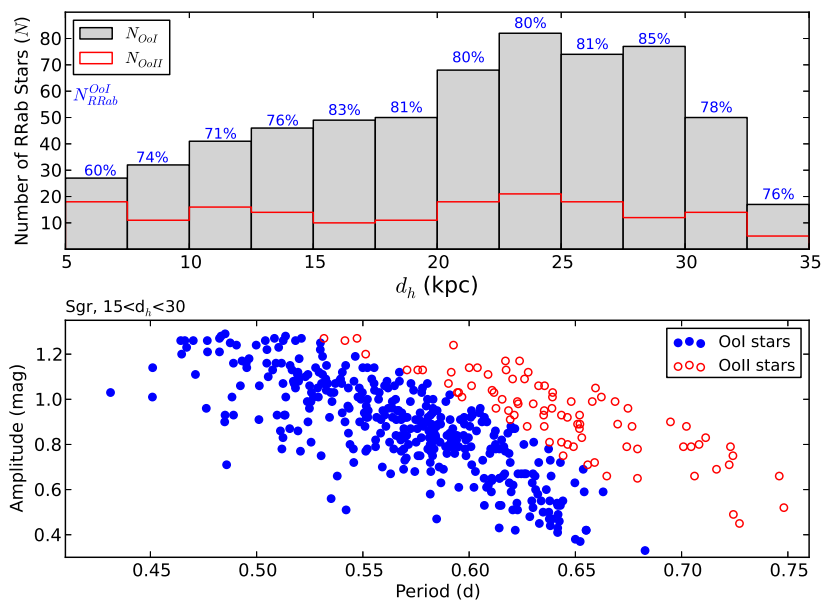


Figure 6.6: Upper panel: Histogram of the heliocentric distance (d_h) distribution of $RRab_{OoI}$ (in grey) and $RRab_{OoII}$ (in red) stars located in the direction of the trailing tail of the Sgr dSp. The percentages of $RRab_{OoI}$ stars (N_{RRab}^{OoI}) are shown in blue for each bin. Lower panel: The P–A distribution for the $RRab$ stars with $15 < d_h < 30$ kpc. The $RRab_{OoI}$ and the $RRab_{OoII}$ stars are shown in blue filled and red open circles, respectively.

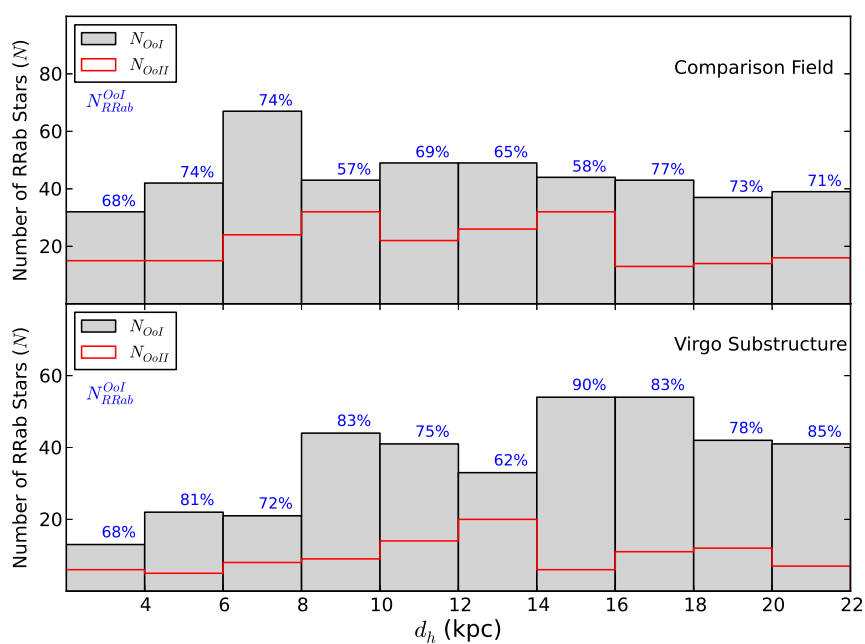


Figure 6.7: Upper panel: Histogram of the distance distribution of RRab_{OoI} (in grey) and RRab_{OoII} (in red) stars located in the comparison field region. The N_{RRab}^{OoI} fractions are shown in blue for each distance bin. Lower panel: Same as the upper panel, but for stars located in the Virgo substructure region.

6.3.3 The Hercules-Aquila Cloud (HAC)

The HAC (Belokurov et al., 2007) is another large halo substructure extending both above and below the disk and located in the 10–20 d_h range. Recently, Simion et al. (2014) detected a RRL star excess in the HAC using the CSS RRab stars and confirmed that the HAC is a distinct stellar halo substructure. Additionally, they found that the majority ($\sim 81\%$) of the HAC RRab stars are of OoI type. The catalog we are using in this study includes ~ 2400 additional CSS RRab stars from Drake et al. (2014), of which ~ 35 are in the direction of the HAC and with $d_h < 24$ kpc. In Figure 6.8, we perform the same analyses done in Sections 6.3.1 and 6.3.2 with the RRab stars located in the HAC region ($31^\circ < l < 55^\circ$, $-45^\circ < b < -25^\circ$, $d_h < 24$ kpc) and we confirm that the sample is dominated by RRab_{OoI} stars ($N_{RRab}^{OoI} \sim 80\%$).

Additionally, we plot the N_{RRab}^{OoI} fractions for each distance bin in the HAC region in the upper panel of Figure 6.8. It is clear that RRab_{OoI} stars dominate the sample ($N_{RRab}^{OoI} > 79\%$) in the 12–22 kpc d_h range where the HAC is located. Just like the Sgr and Virgo substructures, the mean period of RRab stars in the HAC, $\langle P_{ab}^{HAC} \rangle = 0.57$ d, lies near the Oosterhoff gap boundary. Thus, we favor a dSph progenitor nature of the HAC.

6.4 Summary

In this study, we use the largest catalog of RRab stars from the CSS (Drake et al., 2013a,b, 2014) to study the different Oosterhoff populations in the stellar halo, the trailing arm of the Sgr dSph, the Virgo substructure, and the HAC.

In order to distinguish the different populations, we adopt the loci for RRab_{OoI} and RRab_{OoII} stars from Zorotovic et al. (2010). For each star, we then calculate the difference (ΔP) between the CSS period and the predicted period from the RRab_{OoI} locus using Equation (6.1). Stars with $\Delta P \leq 0.045$ d and $\Delta P > 0.045$ d are classified as RRab_{OoI} and RRab_{OoII} stars, respectively. Our P–A density plot in Figure 6.2 and the ΔP distribution presented in Figure 6.3 show that the CSS RRab stars are divided into two distinct groups, the OoI and OoII populations.

We use the [Fe/H] values obtained from the SDSS DR8 and provided by Drake et al. (2013a) to show that the RRab_{OoI} stars are, on average, more metal-rich compared to RRab_{OoII} stars and we confirm the connection between the different Oosterhoff groups and the metallicities (see Figure 6.4). We show that $\sim 73\%$ of the halo RRab stars are of OoI type (Miceli et al., 2008; Zinn et al., 2014) and we present the mean periods and metallicities of the halo RRab_{OoI} and RRab_{OoII} stars. We also show that at larger distances the N_{RRab}^{OoI} decreases and thus the mean metallicities decreases with it. This is also connected with the two turning points we detected in N_{RRab}^{OoI} when we examined its change with R_{gc} . These turning points divide the stellar halo into three main components: the inner halo, the outer halo, and the “extreme outer halo”. The first turning point at $R_{gc} \sim 25$ kpc corresponds to the separation between the inner and outer halo. Another turning point at $R_{gc} \sim 45$ kpc corresponds to an “extreme outer halo” component. Thus, we see a three-fold subdivision of the stellar halo as traced by RRL stars. We believe that the turning points are associated with the break in the halo and the different formation scenarios of the inner and outer halo.

Additionally, we find that the majority ($\sim 80\%$) of the RRab stars in the direction of the Sgr dSph, the Virgo substructure, and the HAC are RRab_{OoI} stars and that the mean periods of these stars lie near the boundary of the Oosterhoff gap. Thus, we favor the dSph progenitor nature of these overdensities.

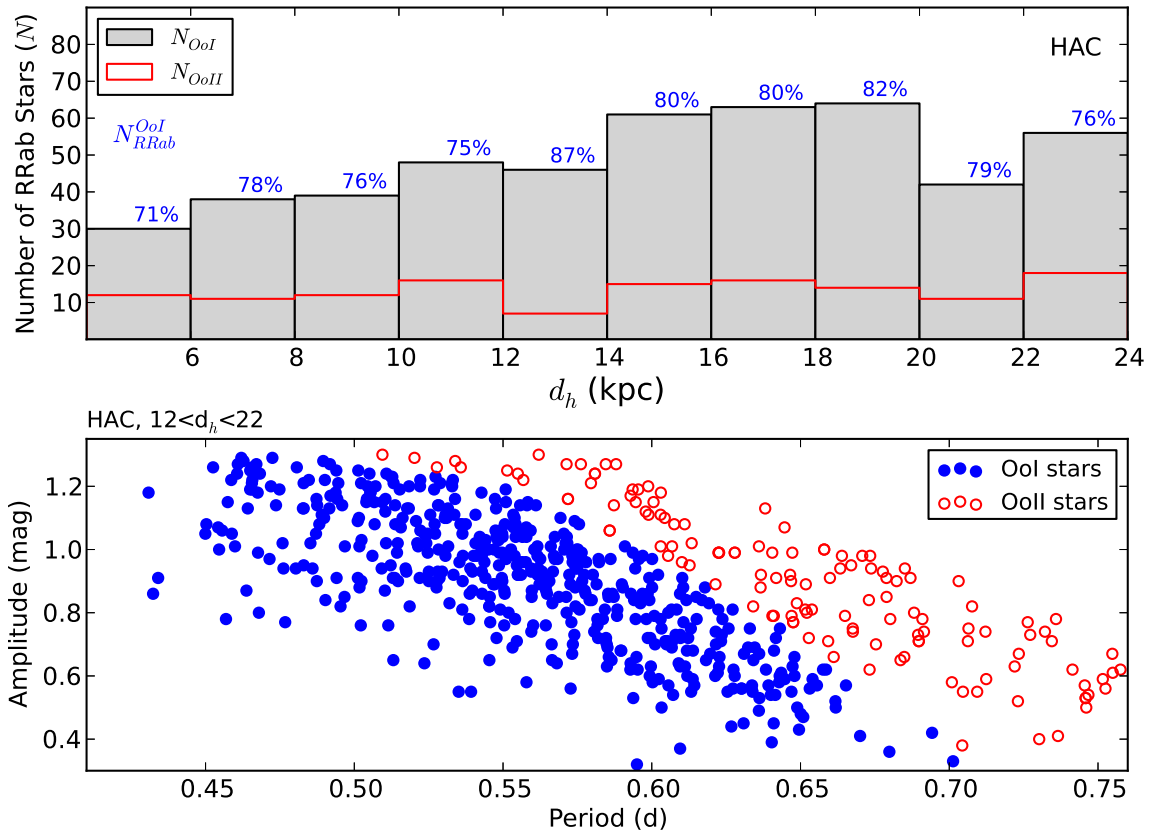


Figure 6.8: Upper panel: Histogram of the distance distribution of $RRab_{OoI}$ (in grey) and $RRab_{OoII}$ (in red) stars located in the HAC direction. The percentages of $RRab_{OoI}$ stars (N_{RRab}^{OoI}) are shown in blue for each bin. Lower panel: The P–A distribution for the $RRab_{OoI}$ (blue filled circles) and $RRab_{OoII}$ (red open circles) stars in the HAC.

Summary

What she really loved was to hang over the edge and watch the bow of the ship slice through the waves. She loved it especially when the waves were high and the ship rose and fell, or when it was snowing and the flakes stung her face.
Kristin Cashore

7.1 Summary

Different themes and topics have been covered in this doctoral dissertation. We started by finding 6371 field RRL stars (4800 RRab and 1571 RRc) in the Milky Way' halo. Of these, ~ 2021 (~ 572 RRab and 1449 RRc) stars are new discoveries. Our RRL stars cover $\sim 14000 \text{ deg}^2$ of the sky and have $d_h < 28 \text{ kpc}$. Our catalog, which is published in Abbas et al. (2014a) and made publicly available, provides the official SDSS designation name, the equatorial J2000.0 R.A. and Dec. in decimal degrees, the CSDR2 mean magnitude, the CSDR2 amplitude, the type, the period, the ephemeris, and the heliocentric distance of each RRL star.

In addition to improving our understanding of the color and variability properties of RRL stars, our method presented a systematic and efficient way to find RRL stars when a large number of repeated observations are available and when light curve analyses are possible. The catalog was also used to detect different halo substructures like the Virgo overdensity, the HAC, and the Sgr stream. Recently, Kinman & Brown (2014) used stellar variability in the ultraviolet bands from GALEX to search for RRL stars. They compared their results to ours (Abbas et al., 2014a) and found similar results (i.e., ~ 0.455 RRL star per square degree of the sky).

Our RRL stars were selected using the SDSS $(u - g)$, $(g - r)$, $(r - i)$, and $(i - z)$ color cuts and the PS1 σ_{gP_1} and σ_{rP_1} variability cuts. The SDSS color and PS1 variability cuts were necessary to select and distinguish RRL from contaminant stars as well as to reduce the number of light curves to be requested from the CSDR2 as the CSDR2 allows the retrieval of only 100 sky objects at a time. Although applying the latter cuts were used to cull our candidate list, contaminant stars like main-sequence stars with colors at the edge of the color range of the RRL stars, W UMa contact binary stars, Algol eclipsing binary stars, δ Scuti and SX Phe stars were still present in our sample. Thus, the CSDR2 variability and light curves for the stars that passed the SDSS color and the PS1 variability cuts were then analyzed and periods were determined using the AoV technique. More than 90% of these stars were observed more than 100 times. Unlike previous studies that looked for RRL stars using the CSDR data, we used the template fitting technique from

Table 7.1: Excess of RRab_{OoI} stars in the halo's substructures

Substructure	N_{RRab}^{OoI} (%)	$\langle P_{ab} \rangle^a$	d_h (kpc)
Sgr dSp	80	0.58	15–30
Virgo substructure	81	0.58	5–20
HAC	79	0.57	12–22

^aMean period in days

Layden (1998) to correctly classify different types of stars. Additionally, we visually inspected all of the RRL candidate light curves. This yielded to the discovery of ~ 2021 new RRL stars. The comparison of our RRL star discoveries with the SDSS-Stripe 82, the GCVS, and the LSQ catalogs of RRL stars confirmed the reliability of our method and showed that our completeness levels are $\sim 50\%$ for RRab and RRC stars and that our efficiency levels are $\sim 99\%$ and $\sim 87\%$ for RRab and RRC stars, respectively.

In addition to detecting halo substructures using the catalog from Abbas et al. (2014a), and to further investigate the formation history of the Milky Way's halo, we studied the different Oosterhoff populations (OoI and OoII) in Abbas et al. (2014d) (in prep.) using the largest catalog of RRab stars from the CSS (Drake et al., 2013a). Previous studies that investigated the Oosterhoff effect in the halo used relatively small catalogs and emphasized the importance of studying the latter effect using larger catalogs. We classified the different Oosterhoff groups by calculating the ΔP between the P_{ab} from the CSS catalog and its predicted $P_{OoI-locus}$ period from the OoI locus (Zorotovic et al., 2010). Stars with $\Delta P \leq 0.045$ d and $\Delta P > 0.045$ d are classified as RRab_{OoI} and RRab_{OoII} stars, respectively (See Equation 6.1). The ΔP histogram of the CSS stars yielded a primary peak at $\Delta P \sim 0$ d which is associated with the RRab_{OoI} stars and another secondary peak at $\Delta P \sim 0.1$ d which is associated with the RRab_{OoII} stars. In agreement with other studies with smaller sky coverage, we find that $\sim 73\%$ of the CSS RRab stars are of OoI type. Thus, we successfully detected and confirmed the existence of the different Oosterhoff groups in the field RRL stars.

We use the [Fe/H] values from the SDSS DR8 database to compare the metallicities of RRab_{OoI} and RRab_{OoII} stars. We find that RRab_{OoI} stars ($\langle [Fe/H] \rangle_{OoI} = -1.57$ dex) are, on average, more metal-rich than RRab_{OoII} stars ($\langle [Fe/H] \rangle_{OoII} = -1.88$ dex). Thus, we confirm that the Oosterhoff groups in the halo are connected to the metallicities. Another interesting result was the detection of two turning points at $R_{gc} \sim 25$ and at $R_{gc} \sim 45$ when we studied the changes of N_{RRab}^{OoI} as a function of R_{gc} . Previous studies that investigated the Galactic structure and the number density profile of the halo found breaks at comparable distances (i.e., Watkins et al. 2009; Sesar et al. 2010; de Jong et al. 2010; Akhter et al. 2012). We believe that these turning points divide the stellar halo into three main components: the inner halo, the outer halo, and the "extreme outer halo". The first turning point at $R_{gc} \sim 25$ kpc corresponds to the separation between the inner and outer halo while the turning point at $R_{gc} \sim 45$ kpc shows an "extreme outer halo" component.

Additionally, we detected excess of RRab_{OoI} stars in the direction and distance range of the Sgr dSph, the Virgo substructure region, and the HAC and we find that the $\langle P_{ab} \rangle$ of RRab stars associated with these overdensities lies near the boundary of the Oosterhoff gap. Specifically, in the direction of the :

- (1) Sgr dSph: $\langle P_{ab}^{SgrTail} \rangle = 0.58$ d and $N_{RRab}^{OoI} \sim 80\%$ for RRab stars with $15 < d_h < 30$ kpc.
- (2) Virgo substructure: $\langle P_{ab}^{Virgo} \rangle = 0.58$ d and $N_{RRab}^{OoI} \sim 81\%$ for RRab stars with $5 < d_h < 20$ kpc.
- (3) HAC: $\langle P_{ab}^{HAC} \rangle = 0.57$ d and $N_{RRab}^{OoI} \sim 79\%$ for RRab stars with $12 < d_h < 22$ kpc.

These values are presented in Table 7.1. The excess of RRab_{OoI} stars in the direction of these halo substructures and their mean periods that lie near the boundary of the Oosterhoff gap suggest their dSph progenitor nature. These systems prove the different formation scenarios of the halo (accretion of a few massive systems in addition to in situ star formation processes).

In this thesis, we also presented an optimized method to find RRL stars or other type of variable stars when large number of multi-epoch data and light curve analyses are not available. Our method was published in Abbas et al. (2014b). We compared our method (which is based on the GMM cuts) to the regularly used methods (that are based on rectangular cuts) and proved that our method yields a significant increase in the efficiency level and an insignificant

change in the completeness levels. Our method also shows how the synergy between data from different surveys and how exploiting the strong points of different surveys (i.e., SDSS colors) to mitigate other weak points of the same surveys (i.e., lack of SDSS multi-epoch data) results in an efficient method to find RRL stars or other type of stellar objects.

We used the color and variability properties of 636 pre-identified RRL from the CSS and LINEAR to define our GMM color and variability boundary cuts. We then applied GMM color cuts ($(u - g)$, $(g - r)$, $(r - i)$, and $(i - z)$) using all of the SDSS filters and GMM variability cuts using the PS1 filters (g_{P1} , r_{P1} , i_{P1} , z_{P1} , and y_{P1}) on stars in Stripe 82. At the same time, we applied the regularly used color and variability rectangular cuts on the same stars and we compared the results of the two methods with the Sesar et al.'s (2010) catalog of RRL stars that is $\gtrsim 99\%$ complete and efficient. Our method yielded an increase in the efficiency level from $\sim 13\%$ to $\sim 77\%$ and an insignificant change in the completeness level. In Stripe 82 area, our method selected 255 RRL candidate stars, out of which 195 are true RRL stars and 60 are contaminant stars. We used the CSS database to study the nature of the contaminant stars to find that 40% of these stars are non-variable stars that passed the PS1 variability cuts due to the small number of PS1 repeated observations (~ 4 epochs only). The remaining 60% of the contaminant stars in Stripe 82 appeared as non-RRL variable stars using the CSS database (i.e., W UMA, δ Scuti, Algol binaries, etc.). Using the small number of multi-epoch data from PS1, there was no way to get rid of all the contaminants.

Since our method yielded high efficiency and completeness levels, we applied our method to the whole SDSS \times PS1 overlapping footprint and we selected 8115 RRL candidates with $d_h < 70$ kpc. Thus, we recovered $\sim 52\%$ of the RRL stars not only in the Stripe 82 region, but in the whole SDSS \times PS1 overlapping footprint. These stars were used to detect halo substructures (i.e., HAC and the arm of the Sgr dSph tidal stream). Although we developed our method over the SDSS \times PS1 footprint, the technique presented in Abbas et al. (2014b) work well on any multi-band, multi-epoch survey for which the number of epochs is limited. Hence, we favor using the GMM technique in future studies.

List of Abbreviations

AoV: Analysis of Variance
CMD: Color-magnitude diagram
CoRoT: Convection Rotation and Planetary Transits satellite mission
Completeness: Fraction of selected RRL stars
Contaminant stars: non-RRL stars
CRTS: Catalina Real-Time Transient Survey
CSDR1: The first photometric catalog of the Catalina Survey
CSDR2: The second photometric catalog from the Catalina Survey
CSS: Catalina Sky Survey
d: day
 d_h : Heliocentric distance
dSph: Dwarf spheroidal
Efficiency: Fraction of true RRL stars in the candidate sample
 $[Fe/H]_{OoI}$: Metallicities of RRab_{OoI} stars
 $[Fe/H]_{OoII}$: Metallicities of RRab_{OoII} stars
GALEX: Galaxy Evolution Explorer
GCVS: General Catalog of Variable Stars
GMM: Gaussian Mixture Bayesian Generative Method
HAC: Hercules-Aquila Cloud
HCO: Harvard College Observatory
 h_z : Scale height
ID_{CSS}: CSS identification numbers
 I_{WS} : Welch-Stetson variability index
LINEAR: Lincoln Near Earth Asteroid Research survey
LONEOS-I: Lowell Observatory Near Earth Objects Survey Phase I
LSQ survey: La Silla QUEST survey
LS: Lomb-Scargle periodogram analysis
MJD: Modified Julian date
MLS: Mt. Lemmon Survey
 $\langle M_V \rangle$: Absolute magnitude
N: Number of observations
NEo: Near Earth object

N_{OoI} : Number of RRab_{OoI} stars
 N_{OoII} : Number of RRab_{OoII} stars
 N_{RRab}^{OoI} : Fraction of RRab_{OoI} stars: $(\frac{N_{OoI}}{N_{OoI}+N_{OoII}})$
OGLE: Optical Gravitational Lensing Experiment
OoI: Oosterhoff type I
OoII: Oosterhoff type II
 $\langle P \rangle$: Mean period
Pal 5: Palomar 5
Pan-STARRS1: Panoramic Survey Telescope and Rapid Response System 1
P–A: Period-amplitude distribution
Periodogram: period vs. power
PS1: Pan-STARRS1 3π Survey
PS1-MD: Pan-STARRS1 Medium Deep Field Survey
QES: Qatar Exoplanet Survey
QUEST: Quasar Equatorial Survey Team
RRab: RRL of ab type
RRab_{OoI}: Rab stars of OoI type
RRab_{OoII}: Rab stars of OoII type
RRc: RRL of c type
RRd: RRL of d type
RRL: RR Lyrae
 R_{gc} : Galactocentric distances
SDSS: Sloan Digital Sky Survey
SDSS DR7: SDSS 7th data release
SDSS DR8: SDSS 8th data release
SEKBO: Southern Edgeworth-Kuiper Belt Object
Sgr: Sagittarius
Sgr dSph galaxy: Sagittarius dwarf spheroidal galaxy
SSS: Siding Spring Survey
TFM: Template Fitting Method
 Var : Variance
VOD: Virgo Overdensity
VSS: Virgo Stellar Stream
W UMa: Ursae Majoris stars
 W_{σ} : Weighted standard deviation
2MASS: Two Micron All Sky Survey

Bibliography

- Abbas, M. A., Grebel, E. K., Martin, N. F., et al. 2014a, MNRAS, 441, 1230
- Abbas, M., Grebel, E. K., Martin, N. F., et al. 2014b, AJ, 148, 8
- Abbas, M., Layden, A., Guldenschuh, K., et al. 2014c, arXiv:1410.3305
- Abbas, M., Grebel, E. K., and Huxor, A., 2014d, in prep.
- Aihara, H., Allende Prieto, C., An, D., et al. 2011, ApJS, 193, 29
- Akhter, S., Da Costa, G. S., Keller, S. C., & Schmidt, B. P. 2012, ApJ, 756, 23
- Alcock, C., Allsman, R., Alves, D. R., et al. 2000, ApJ, 542, 257
- Alsbai, K. A., Parley, N. R., Bramich, D. M., et al. 2013, Acta Astron, 63, 465
- Bailey, S. I. 1902, Annals of Harvard College Observatory, 38, 1
- Beers, T. C., Carollo, D., Ivezić, Ž., et al. 2012, ApJ, 746, 34
- Bell, E. F., Zucker, D. B., Belokurov, V., et al. 2008, ApJ, 680, 295
- Belokurov, V., Evans, N. W., Bell, E. F., et al. 2007, ApJ Lett., 657, L89
- Bernard, E. J., Ferguson, A. M. N., Schlafly, E. F., Abbas, M. et al. 2014 MNRAS, 443, L84
- Baker, J. M., Layden, A. C., Welch, D. L., & Webb, T. M. A. 2007, AJ, 133, 139
- Blažko, S. 1907, Astronomische Nachrichten, 175, 325
- Bonaca, A., Jurić, M., Ivezić, Ž., et al. 2012, AJ, 143, 105
- Bowell, E., Koehn, B. W., Howell, S. B., Hoffman, M., & Muinonen, K. 1995, Bulletin of the American Astronomical Society, 27,1057
- Buchler, J. R., & Kolláth, Z. 2011, ApJ, 731, 24

- Bullock, J. S., Kravtsov, A. V., & Weinberg, D. H. 2001, *ApJ*, 548, 33
- Bullock, J. S., & Johnston, K. V. 2005, *ApJ*, 635, 931
- Bramich, D. M., Alsubai, K. A., Arellano Ferro, A., et al. 2014, *Information Bulletin on Variable Stars*, 6106, 1
- Cacciari, C., & Clementini, G. 2003, *Stellar Candles for the Extragalactic Distance Scale (Lecture Notes in Physics)*, Vol. 635, ed. D. Alloin & W. Gieren (Berlin: Springer), 105
- Carlin, J. L., Yam, W., Casetti-Dinescu, D. I., et al. 2012, *ApJ*, 753, 145
- Carollo, D., Beers, T. C., Lee, Y. S., et al. 2007, *Nature*, 450, 1020
- Carollo, D., Beers, T. C., Chiba, M., et al. 2010, *ApJ*, 712, 692
- Catelan, M. 2006, *Revista Mexicana de Astronomia y Astrofisica Conference Series*, 26, 93
- Catelan, M. 2009, *Ap&SS*, 320, 261
- Chadid, M., Benkő, J. M., Szabó, R., et al. 2010, *A&A.*, 510, A39
- Chadid, M., Perini, C., Bono, G., et al. 2011, *A&A.*, 527, A146
- Clement, C. M., Muzzin, A., Dufton, Q., et al. 2001, *AJ*, 122, 2587
- Contreras Ramos, R., Clementini, G., Federici, L., et al. 2013, *ApJ*, 765, 71
- Cooper, A. P., Cole, S., Frenk, C. S., et al. 2010, *MNRAS*, 406, 744
- Cox, J. P., & Whitney, C. 1958, *ApJ*, 127, 561
- Cusano, F., Clementini, G., Garofalo, A., et al. 2013, *ApJ*, 779, 7
- Deason, A. J., Belokurov, V., & Evans, N. W. 2011, *MNRAS*, 416, 2903
- Dehnen, W., Odenkirchen, M., Grebel, E. K., & Rix, H.-W. 2004, *AJ*, 127, 2753
- de Jong, J. T. A., Yanny, B., Rix, H.-W., et al. 2010, *ApJ*, 714, 663
- De Lee, N. 2008, Ph.D. Thesis, Michigan State Univ.
- De Lucia, G., & Helmi, A. 2008, *MNRAS*, 391, 14
- Dotter, A., Sarajedini, A., Anderson, J., et al. 2010, *ApJ*, 708, 698
- Duffau, S., Zinn, R., Vivas, A. K., et al. 2006, *ApJ Lett.*, 636, L97
- Duffau, S., Vivas, A. K., Zinn, R., Méndez, R. A., & Ruiz, M. T. 2014, *A&A.*, 566, A118
- Drake, A. J., Djorgovski, S. G., Mahabal, A., et al. 2009, *ApJ*, 696, 870
- Drake, A. J., Catelan, M., Djorgovski, S. G., et al. 2013a, *ApJ*, 763, 32
- Drake, A. J., Catelan, M., Djorgovski, S. G., et al. 2013b, *ApJ*, 765, 154
- Drake, A. J., Graham, M. J., Djorgovski, S. G., et al. 2014, *ApJS*, 213, 9

- Dwek, E., Arendt, R. G., Hauser, M. G., et al. 1995, *ApJ*, 445, 716
- Eddington, A. S. 1926, *The Internal Constitution of the Stars*, Cambridge: Cambridge University Press, 1926. ISBN 9780521337083
- Eggen, O. J., Lynden-Bell, D., & Sandage, A. R. 1962, *ApJ*, 136, 748
- Font, A. S., McCarthy, I. G., Crain, R. A., et al. 2011, *MNRAS*, 416, 2802
- Fukugita, M., Ichikawa, T., Gunn, J. E., et al. 1996, *AJ*, 111, 1748
- Freeman, K., & Bland-Hawthorn, J. 2002, *Ann. Rev. Astron. Astrophys.*, 40, 487
- Garofalo, A., Cusano, F., Clementini, G., et al. 2013, *ApJ*, 767, 62
- Greco, C., Clementini, G., Held, E. V., et al. 2010, *IAU Symposium*, 266, 411
- Grillmair, C. J., & Dionatos, O. 2006, *ApJ Lett.*, 641, L37
- Hadjijska, E., Rabinowitz, D., & Baltay, C. et al. 2012, *IAU Symp. 285, New Horizons in Time-domain Astronomy*, ed. E. Griffin, R. Hanison, & R. Seaman (Cambridge: Cambridge Univ. Press), 324
- Haschke, R., Grebel, E. K., Frebel, A., et al. 2012, *AJ*, 144, 88
- Helmi, A., Cooper, A. P., White, S. D. M., et al. 2011, *ApJ Lett.*, 733, L7
- Ibata, R. A., Gilmore, G., & Irwin, M. J. 1995, *MNRAS*, 277, 781
- Ivezić, Ž., Goldston, J., Finlator, K., et al. 2000, *AJ*, 120, 963
- Ivezić, Ž., Vivas, A. K., Lupton, R. H., & Zinn, R. 2005, *AJ*, 129, 1096
- Ivezić, Ž., Sesar, B., Jurić, M., et al. 2008, *ApJ*, 684, 287
- Ivezić, Ž., Beers, T. C., & Jurić, M. 2012, *Ann. Rev. Astron. Astrophys.*, 50, 251
- Johnston, K. V., Bullock, J. S., Sharma, S., et al. 2008, *ApJ*, 689, 936
- Jurcsik, J., Sódor, Á., Szeidl, B., et al. 2009, *MNRAS*, 400, 1006
- Jurić, M., Ivezić, Ž., Brooks, A., et al. 2008, *ApJ*, 673, 864
- Kaiser, N., Aussel, H., Burke, B. E., et al. 2002, *Proc. SPIE*, 4836, 154
- Keller, S. C., Murphy, S., Prior, S., Da Costa, G., & Schmidt, B. 2008, *ApJ*, 678, 851
- Kennedy, C. R., Stancliffe, R. J., Kuehn, C., et al. 2014, *ApJ*, 787, 6
- Kholopov, P. N., Samus, N. N., Frolov, M. S., et al. 1998, *Combined General Catalogue of Variable Stars*, 4.1 Ed (II/214A). (1998)
- Kinemuchi, K., Smith, H. A., Woźniak, P. R., McKay, T. A., & ROTSE Collaboration 2006, *AJ*, 132, 1202
- Kinman, T. D., Cacciari, C., Bragaglia, A., Buzzoni, A., & Spagna, A. 2007, *MNRAS*, 375, 1381
- Kinman, T. D., Cacciari, C., Bragaglia, A., Smart, R., & Spagna, A. 2012, *MNRAS*, 422, 211

- Kinman, T. D., & Brown, W. R. 2014, arXiv:1408.0808
- Kolenberg, K., Szabó, R., Kurtz, D. W., et al. 2010, *ApJ Lett.*, 713, L198
- Kunder, A., Stetson, P. B., Catelan, M., Walker, A. R., & Amigo, P. 2013, *AJ*, 145, 33
- Law, D. R., Majewski, S. R., & Johnston, K. V. 2009, *ApJ Lett.*, 703, L67
- Law, D. R., & Majewski, S. R. 2010, *ApJ*, 718, 1128
- Layden, A. C., Hanson, R. B., Hawley, S. L., Klemola, A. R., & Hanley, C. J. 1996, *AJ*, 112, 2110
- Layden, A. C. 1998, *AJ*, 115, 193
- Layden, A. C., Ritter, L. A., Welch, D. L., & Webb, T. M. A. 1999, *AJ*, 117, 1313
- Layden, A. C., Bowes, B. T., Welch, D. L., & Webb, T. M. A. 2003, *AJ*, 126, 255
- Lomb, N. R. 1976, *Ap&SS*, 39, 447
- Magnier, E. A., Schlafly, E., Finkbeiner, D., et al. 2013, *ApJS*, 205, 20
- Majewski, S. R., Skrutskie, M. F., Weinberg, M. D., & Ostheimer, J. C. 2003, *ApJ*, 599, 1082
- Marconi, M. 2009, *American Institute of Physics Conference Series*, 1170, 223
- Martin, D. C., Fanson, J., Schiminovich, D., et al. 2005, *ApJ Lett.*, 619, L1
- Martínez-Delgado, D., Peñarrubia, J., Jurić, M., Alfaro, E. J., & Ivezić, Z. 2007, *ApJ*, 660, 1264
- Miceli, A., Rest, A., Stubbs, C. W., et al. 2008, *ApJ*, 678, 865
- Minniti, D., & Zoccali, M. 2008, *IAU Symposium*, 245, 323
- Moody, R., Schmidt, B., Alcock, C., et al. 2003, *Earth Moon and Planets*, 92, 125
- Morganson, E., De Rosa, G., Decarli, R., et al. 2012, *AJ*, 143, 142
- Newberg, H. J., Yanny, B., Rockosi, C., et al. 2002, *ApJ*, 569, 245
- Newberg, H. J., Yanny, B., Grebel, E. K., et al. 2003, *ApJ Lett.*, 596, L191
- Odenkirchen, M., Grebel, E. K., Rockosi, C. M., et al. 2001, *ApJ Lett.*, 548, L165
- Odenkirchen, M., Grebel, E. K., Dehnen, W., et al. 2003, *AJ*, 126, 2385
- Oosterhoff, P. T. 1939, *The Observatory*, 62, 104
- Palaversa, L., Ivezić, Ž., Eyer, L., et al. 2013, *AJ*, 146, 101
- Pickering, E. C., Colson, H. R., Fleming, W. P., & Wells, L. D. 1901, *ApJ*, 13, 226
- Reimann, J. D. 1994, Ph.D. Thesis
- Saha, A. 1985, *ApJ*, 289, 310
- Samus, N. N., Durlevich, O. V., & et al. 2009, *VizieR Online Data Catalog*, 1, 2025

- Schlafly, E. F., & Finkbeiner, D. P. 2011, *ApJ*, 737, 103
- Schlaufman, K. C., Rockosi, C. M., Allende Prieto, C., et al. 2009, *ApJ*, 703, 2177
- Schlaufman, K. C., Rockosi, C. M., Lee, Y. S., et al. 2012, *ApJ*, 749, 77
- Schlegel, D. J., Finkbeiner, D. P., & Davis, M. 1998, *ApJ*, 500, 525
- Schwarzenberg-Czerny, A. 1989, *MNRAS*, 241, 153
- Schwarzschild, M. 1940, *Harvard College Observatory Circular*, 437, 1
- Searle, L., & Zinn, R. 1978, *ApJ*, 225, 357
- Sesar, B., Ivezić, Ž., Grammer, S. H., et al. 2010, *ApJ*, 708, 717
- Sesar, B., Stuart, J. S., Ivezić, Ž., et al. 2011a, *AJ*, 142, 190
- Sesar, B., Jurić, M., & Ivezić, Ž. 2011b, *ApJ*, 731, 4
- Sesar, B., Ivezić, Ž., Stuart, J. S., et al. 2013, *AJ*, 146, 21
- Shapley, H. 1914, *ApJ*, 40, 448
- Simion, I. T., Belokurov, V., Irwin, M., & Koposov, S. E. 2014, *MNRAS*, 440, 161
- Skrutskie, M. F., Cutri, R. M., Stiening, R., et al. 2006, *AJ*, 131, 1163
- Smith, H. A. 1995, *RR Lyrae Stars*. Cambridge Univ. Press, Cambridge
- Smith, H. A., Catelan, M., & Kuehn, C. 2011, *Carnegie Observatories Series, Vol. 5, RR Lyrae Stars, Metal-Poor Stars, and the Galaxy*, ed. A. McWilliam (Pasadena, CA: The Observatories of the Carnegie Institution of Washington), 17
- Soszyński, I., Udalski, A., Szymański, M. K., et al. 2009, *AcA*, 59, 1
- Sparke, L. S., & Gallagher, J. S., III 2007, *Galaxies in the Universe: An Introduction*. Second Edition. By Linda S. Sparke and John S. Gallagher, III. ISBN-13 978-0-521-85593-8 (HB); ISBN-13 978-0-521-67186-6 (PB). Published by Cambridge University Press, Cambridge, UK, 2007
- Tonry, J. L., Stubbs, C. W., Lykke, K. R., et al. 2012, *ApJ*, 750, 99
- VanderPlas, J., Connolly, A. J., Ivezić, Z., & Gray, A. 2012, *Statistics, Data Mining and Machine Learning in Astronomy*. Princeton Univ. Press, Princeton, NJ
- Vivas, A. K., Zinn, R., Andrews, P., et al. 2001, *ApJ Lett.*, 554, L33
- Vivas, A. K., Zinn, R., Abad, C., et al. 2004, *AJ*, 127, 1158
- Vivas, A. K., & Zinn, R. 2006, *AJ*, 132, 714
- Vivas, A. K., Jaffé, Y. L., Zinn, R., et al. 2008, *AJ*, 136, 1645
- Watkins, L. L., Evans, N. W., Belokurov, V., et al. 2009, *MNRAS*, 398, 1757
- Welch, D. L., & Stetson, P. B. 1993, *AJ*, 105, 1813
- Werner, M. W., Roellig, T. L., Low, F. J., et al. 2004, *ApJS*, 154, 1

- Yanny, B., Newberg, H. J., Kent, S., et al. 2000, *ApJ*, 540, 825
- Yanny, B., Newberg, H. J., Grebel, E. K., et al. 2003, *ApJ*, 588, 824
- York, D. G., Adelman, J., Anderson, J. E., Jr., et al. 2000, *AJ*, 120, 1579
- Zhevakin, S. A. 1959, *AZh*, 36, 269
- Zinn, R., Horowitz, B., Vivas, A. K., et al. 2014, *ApJ*, 781, 22
- Zolotov, A., Willman, B., Brooks, A. M., et al. 2010, *ApJ*, 721, 738
- Zorotovic, M., Catelan, M., Smith, H. A., et al. 2010, *AJ*, 139, 357

Acknowledgments

Gratitude for the abundance you have received is the best insurance that the abundance will continue. Prophet Muhammad

This work would not have been possible without the enormous help and support I received from people around me throughout the years. Thank you is the least I can say to you to show my appreciation.

I thank my PhD advisor and mentor Prof. Dr. Eva K. Grebel who has supported me in the past three and half years. She provided me with constant support, knowledge, and guidance. I thank her for always listening to my research ideas, even when they made no sense! The friendly and intellectual environment she created enhanced my confidence and knowledge. I am extremely grateful for all the countless time she spent teaching me about astronomy, correcting my paper drafts, writing letters of recommendations, and for the freedom she gave me to explore different scientific topics and to attend different meetings and conferences. This thesis dissertation would not have existed without your help, thank you.

I would like to thank Prof. Dr. Andrew Layden who was the first to show me how to “research”. Throughout the years, Dr. Layden has inspired me with his knowledge, patience, and support. He spent countless hours explaining and teaching me about astronomy, telescopes, dark frames, flat frames, writing recommendation letters, and the list goes on... In addition to being my masters thesis advisor, Dr. Layden was a friend who provided me with personal support and advices. He was there for me when I was going through my worst times. Thank you Dr. Layden for all you have done for me.

I would also like to acknowledge my committee members: Prof. Dr. Joachim Wambsganss, Dr. Andreas Wolf, and Dr. Andreas Koch, who graciously agreed to serve on my committee, when they probably have lots of other duties and work to do. Without them, I would not have been able to deliver my thesis on time. At the same time, I thank Dr. Sonia Duffau who guided me during my first year during my PhD. She generously shared her knowledge, codes, ideas, and data with me. I thank her for putting me on the right track and for her constant support.

Special thanks go to Dr. Nicolas F. Martin, Dr. Avon Huxor, and Dr. Edouard Bernard who regularly reviewed my work and who provided me with suggestions, ideas, and comments that helped me improve the quality of my work. I also thank Dr. Martin for spending time writing recommendation letters on my behalf.

I also need to thank Dr. Dale Smith, Dr. Johannes Ludwig, Dr. Raoul Haschke, Dr. Oleksiy Golubov, Dr. Stefan Schmeja, Dr. Veronica Lora, Dr. Xiaoying Pang, Dr. Corrado Boeche, Dr. Sara Najem, and Dr. Matthias Frank who supported me throughout the years.

Special thanks go to Jan Rybizki, John Vickers, Mirko Simunovic, Gustavo Morales, Ghina Halabi, Peter Zeidler, Fabrizio Arrigoni Battaia, Eduardo Banados Torres, Anahi Caldu Primo, Salvatore Cielo, Nikolay Kacharov, Maria Elena Manjavacas, Michael Maseda, Svea Proft, Frederik Schoenebeck, Deniss Stepanovs, Akin Yildirim, and Gustavo A Cardona. They were not only good “party” partners, but also talented researches who provided me with great advices and comments that helped me in finishing my PhD thesis.

Another thank you goes to the coordinating scientist of the IMPRS, Dr. Christian Fendt. Dr. Fendt provided me and other IMPRS students with a lot of support and advices during the last years.

To my family, thank you for always encouraging me to follow my dreams. Thank you for your constant emotional and financial support and for always believing in me. Thank you for teaching me about life in the good and bad times. Thank you Ali, Hannan, Tania, Lara, Katia, Hussein, and Aya. Thank you Hussein Awada, Ghassan Beydoun, Natasha M. Saad, Shatha, Yasmina, Celine, Hadi, Rena, Shatha, and Aseel. I love you all. Special thanks go to Raheel Hammoud, Lina, Abbas, Sara, Ruba, and Assad Mousawi and to Najah, Maya, Nisreen and Hassan Sharara.

To my friends, thank you for listening, offering me advice, and supporting me throughout the years. Special thanks go to my Heidelberg friends: Areej Albariri, Hannan Slimani, Walid Inani, Anna, Firas Odeh, Paulina Fischer, Richard Fritsch, Paul Joriz, Cris Masia, Martin, Lisa Johansen, Franziska Kroker, Katie Cbrook, and Stefania Mamberti.

I can't but thank some of my friends from Lebanon: Jaafar Darwish, Rami Shouker, Jad Kishle, Mirna Salloum, Omar Aridi, Bashir Handous, Mohamad Mackook, Bob Mantoufe, Samer Al Jammal, Mohamad Olaymi, and Mohamad Joud as well as my good old friends from Bowling Green: Ashley Merriweather, Hannah Simon, Giselle Veller, David Michael Smith, Hosam Mesmar, Matt Richardson, and Maagan Reedy.

Special thanks go to one of my best friends Emily Volland who has always inspired me with her thoughts and ideas and who offered me unconditional support. I will never forget the fun times we spent together in Bowling Green. I would like to thank more of my best friends, Johnny Mayer and Lucas Haigermoser. Johnny and Luu have always been the best party partners whom I share great and countless memories with, and yet more to come. Thank you my best “egypcion” friend Marwa ElRefaey for always being there for me and for all the good times we had. You have the kindest and sweetest heart. Thanks to my special childhood friend Jaafar Darwish who supported and helped me throughout the years. Thank you for your loyalty my friend. Special thanks go to Sara Osman who never failed to put a smile on my face. Thank you for bearing with me during the bad times and for taking care of me during the good times. Thank you for always listening to my ideas and for always pushing me to do what I want, even though you are not interested in Astronomy. Thank you for the mugs you brought me from different cities and thank you for the Mjadara and Fasoolya. Thank you for letting me see the world differently. I am not sure if I can thank you enough. We have acquired great memories in a very short time. I am grateful to have met you.

I acknowledge support by the Collaborative Research Center “The Milky Way System” (SFB 881, subproject A3) of the German Research Foundation (DFG). The Pan-STARRS1 Surveys (PS1) have been made possible through contributions of the Institute for Astronomy, the University of Hawaii, the Pan-STARRS Project Office, the Max-Planck Society and its participating institutes, the Max Planck Institute for Astronomy, Heidelberg and the Max Planck Institute for Extraterrestrial Physics, Garching, The Johns Hopkins University, Durham University, the University of Edinburgh, Queen's University Belfast, the Harvard-Smithsonian Center for Astrophysics, the Las Cumbres Observatory Global Telescope Network Incorporated, the National Central University of Taiwan, the Space Telescope Science Institute, the National Aeronautics and Space Administration under Grant No. NNX08AR22G issued through the Planetary Science Division of the NASA Science Mission Directorate, the National Science Foundation under Grant No. AST-1238877, the University of Maryland, and Eotvos Lorand University (ELTE). Funding for SDSS-III has been provided by the Alfred P. Sloan Foundation, the Participating Institutions, the National Science Foundation, and the U.S. Department of Energy Office of Science. The SDSS-III web site is <http://www.sdss3.org/>. SDSS-III is managed by the Astrophysical Research Consortium for the Participating Institutions of the SDSS-III Collaboration including the University of

Arizona, the Brazilian Participation Group, Brookhaven National Laboratory, Carnegie Mellon University, University of Florida, the French Participation Group, the German Participation Group, Harvard University, the Instituto de Astrofísica de Canarias, the Michigan State/Notre Dame/JINA Participation Group, Johns Hopkins University, Lawrence Berkeley National Laboratory, Max Planck Institute for Astrophysics, Max Planck Institute for Extraterrestrial Physics, New Mexico State University, New York University, Ohio State University, Pennsylvania State University, University of Portsmouth, Princeton University, the Spanish Participation Group, University of Tokyo, University of Utah, Vanderbilt University, University of Virginia, University of Washington, and Yale University. The CRTS is supported by the U.S. National Science Foundation under grants AST-0909182 and CNS-0540369. The work at Caltech was supported in part by the NASA Fermi grant 08-FERMI08-0025 and by the Ajax Foundation. The CSS survey is funded by the National Aeronautics and Space Administration under grant No. NNG05GF22G issued through the Science Mission Directorate Near-Earth Objects Observations Program.

Mohamad Abbas

Phone +4917664886483
Fax +496221541888
E-mail mabbas@ari.uni-heidelberg.de
Address Heidelberg, Germany

PERSONAL DATA

Gender: Male
Nationality: Lebanese

Date of Birth: February 1st, 1987
Place of Birth: Kuwait, Kuwait
Marital Status: Single

EDUCATION

University of Heidelberg

Astronomisches Rechen-Institut, Heidelberg, Germany

PhD – Astronomy

(2011 – expected: Dec 2014)

- International Max Planck Research School for Astronomy and Cosmic Physics (IMPRS)
- Advisor: Prof. Dr. Eva Grebel
- Thesis Topic: RR Lyrae stars, substructures, and the Oosterhoff dichotomy in the Halo of the Milky Way

Bowling Green State University (BGSU)

Ohio, USA

Master of Science (M.Sc.) – Physics, (4.0 GPA)

2009 – 2011

- Honor list: all semesters
- Advisor: Dr. Prof. Andrew Layden
- Thesis Topic: Variable Stars in Globular Clusters

American University of Beirut (AUB)

Beirut, Lebanon

Bachelor of Science (B.Sc.) – Physics, (3.37 GPA)

2006 – 2009

- Honor list: 2007-2008

RESEARCH EXPERIENCE

- Oosterhoff analysis of the halo RRL stars 2014 – ongoing
- Searching for blue straggler stars in globular clusters 2014 – ongoing
- Studying and finding new RRL stars to map the substructure of the Galaxy's halo using different surveys 2011 – ongoing
- Studying and developing Light Curve Analysis methods to statistically classify the star's variability type 2011 – ongoing
- Identifying color cuts and properties of RRL stars using different surveys (*Pan-STARRS*, *SDSS*, *2M...*) 2011 - ongoing
- Studying Long Period Variable Stars in Globular Clusters 2009 - ongoing
- Studying interstellar dust and star evolution (BGSU) 2009 - 2011
- Testing the visibility in different locations in Lebanon using appropriate software and telescopes 2008 - 2009
- Oil spill impact on the Lebanese coast. The study sheds light on the effects of oil spill on fish (AUB) 2007 - 2009
- Research Assistant in the Animal Pathology lab at AUB, both literature and lab work Summer of 2007

SKILLS, TECHNICAL EXPERIENCE, AND LANGUAGES

Data Analysis and Programming:

- Handling and performing statistical analysis on massive amount of data from very large surveys (*i.e.*, *Pan-STARRS*, *SDSS*, *CATALINA...*)
- Image stacking and photometric techniques: *IRAF*, *DAOPHOT*, *ISIS*, and others
- Programming: *Python*, *Matlab*, and others

Observing Experience:

- Operating the BGSU observatory (0.5m telescope) to observe different globular clusters, CCD Imaging 2009 - 2011
- Observing remotely using Robotic Telescopes (PROMPT) 2009 - ongoing
- Operating Lx-200 Meade Telescopes and other solar telescopes

Languages:

- Fluent in Arabic and English. Basic in German.

TEACHING EXPERIENCE

- *Galactic & Extragalactic Astronomy* (solving sessions). Spring 2013 and 2014, Heidelberg. Undergraduate and graduate course
- *Phy201*: General Physics I (lecture summary and lab), Fall, Spring, and Summer of 2009-2011, BGSU. Undergraduate course
- *Phy202*: General Physics II (lecture summary and lab), Fall, Spring, and Summer 2009-2011, BGSU. Undergraduate course
- *Classical Physics Lab* (assistant for the lab instructor). Summer 2008, AUB
- *Tutoring: Teaching physics and mathematics courses for high school and college students since 2005*

HONORS AND AWARDS

- Win Stone Award for graduating with a cumulative total GPA of 4.0, BGSU 2011
- Arthur Award for research and academic excellence, BGSU 2011
- Arthur Award for research and academic excellence, BGSU 2010
- Dean's Honor List of the American University of Beirut 2007 - 2008
- Electricity production award - Beirut Baptist School 2005

PROFESSIONAL MEMBERSHIP

- Member of the International Planetarium Society (IPS) 2013 - ongoing
- Junior member of the American Astronomical Society (AAS) 2011 - ongoing
- Student Representative of the IMPRS students at Heidelberg 2011 - 2012
- Graduate Representative of the World Student Association at BGSU 2010 - 2011
- Founder and president of the Astronomy Club at AUB 2009
- President of the Physics Society at AUB 2008 - 2009
- Member of the Lebanese Astronomy Group (LAG)
- Member of the "Toufoula" organization which helps children suffering from cancer in Lebanon

OTHER ACTIVITIES

- Playing the "oud" and guitar
- Drawing, acting in theatre, film production, reading, and writing

SELECTED CONFERENCES, POSTERS, AND TALKS

- International astronomical union - regional meeting, *Beirut, Lebanon* *September 2014*
- The Multi-wavelength, multi-epoch heritage of Stripe 82, *Princeton University, NJ, USA* *March 2014*
- Pan-STARRS Science Consortium Meeting (PS1SC), *National Central University, Taiwan* *November 2013*
- GREAT Astro-Statistics School, *Alicante, Spain* *June 2013*
- Variable Stars talk, *Bowling Green State University, Ohio, USA* *January 2013*
- Ecology of Blue Straggler Stars, *European Southern Observatory, Santiago, Chile* *November 2012*
- The art of observational techniques, *La Laguna University, Canary Islands, Spain* *September 2012*
- GREAT School on the Science and Techniques of Gaia, *Leiden, the Netherlands* *February 2012*
- American Astronomical Society, *Austin, Texas, USA* *January 2012*
- Annual meeting of the Astronomische Gesellschaft, *Heidelberg, Germany* *September 2011*
- Variable Stars Meeting, *Michigan State University, MI, USA* *March 2010*

PUBLICATION LIST

- The Oosterhoff Populations in the Milky Way's Halo.
Abbas, M., Grebel, E., and Huxor, A. (**In Prep.**)
- Variable Stars in the Metal-Rich Globular Cluster NGC 6496.
Abbas, M., Layden, A., Guldenschuh, K., Reichart, D., Ivarsen, K., Haislip, J., Nysewander, M., LaCluyze, A., and Welch, D.
The Astronomical Journal (**Accepted 2014 September 27**). (<http://adsabs.harvard.edu/abs/2014arXiv1410.3305A>).
- An Optimized Method to Identify RR Lyrae Stars in the SDSS×Pan-STARRS1 Overlapping Area Using a Bayesian Generative Technique.
Abbas, M., Grebel, E., Martin, N., Kaiser, N., Burgett, W., Hubers, M., and Waters, C.
The Astronomical Journal (**Accepted 2014 April 23**). (<http://adsabs.harvard.edu/abs/2014AJ....148....8A>).
- Newly Discovered RR Lyrae Stars in the SDSSXPan-STARRS1XCatalina Footprint.
Abbas, M., Grebel, E., Martin, N., Burgett, W., Flewelling, H., and Wainscoat, R.
Monthly Notices of the Royal Astronomical Society (**Accepted 2014 March 30**). (<http://adsabs.harvard.edu/abs/2014MNRAS.441.1230A>).
- Serendipitous Discovery of a Thin Stellar Stream near the Galactic Bulge in the Pan-STARRS1 3Pi Survey.
Edouard, B., Annette, F., Schlafly, E., **Abbas, M.,** Bell, E., Martin, N., Hand-Walter, R., Sesar, B., et al.
Monthly Notices of the Royal Astronomical Society (**Accepted 2014 June 06**). (<http://adsabs.harvard.edu/abs/2014MNRAS.443L..84B>).

REFERENCES

(1) Prof. Dr. Eva K. Grebel

Director of the Astronomisches Rechen-Institut
Mönchhofstraße 12-14
D-69120 Heidelberg, Germany
Phone: +49 (0)622154 1810
grebel@ari.uni-heidelberg.de

(2) Prof. Dr. Andrew Layden

Department of Physics & Astronomy
Bowling Green State University
Bowling Green, OH 43403, USA
Phone: +1 4193728653
laydena@bgsu.edu

(3) Prof. Dr. Nicolas F. Martin

Strasbourg Observatory, France &
Max Planck Institute for Astronomy
Königstuhl 17
D-69117 Heidelberg, Germany
Phone: +49 (0)6221528453
martin@mpia-hd.mpg.de

(4) Dr. Christian Fendt

Max Planck Institute for Astronomy
Königstuhl 17
D-69117 Heidelberg, Germany
Phone: +49 (0)6221528387
fendt@mpia.de

(5) Prof. Dr. Dale Smith

Prof. and Planetarium Director
Department of Physics & Astronomy
Bowling Green State University
Bowling Green, OH 43403, USA
Phone: +1 4193728666
dsmith@newton.bgsu.edu

(6) Prof. Dr. Mounib El-Eid

American University of Beirut
P.O.Box 11-0236 / Physics Department
Beirut 1107 2020, Lebanon
Phone: +961 1340460
meid@aub.edu.lb

FULL ADDRESS

M. Abbas
Astronomisches Rechen-Institut
Mönchhofstr. 12-14
69120 Heidelberg, Germany
Alternate email: astromabbas@gmail.com